To the Graduate Council:

I am submitting herewith a dissertation written by Jose L. Rivera-Rojas entitled "Molecular modeling at interfaces: Phase equilibria of complex fluids, and mechanical properties of nanostructures." I have examined the final electronic copy of this dissertation for form and content and recommend that it be accepted in partial fulfillment of the requirements for the degree of Doctor of Philosophy, with a major in Chemical Engineering.

Peter T. Cummings
Major Professor

We have read this dissertation
and recommend its acceptance:

Brian Edwards

David Keffer

Roberto Benson

Accepted for the Council:

Anne Mayhew
Vice Provost and
Dean of Graduate Studies

(Original signatures are on file with official student records.)

# MOLECULAR MODELING AT INTERFACES: PHASE EQUILIBRIA OF COMPLEX FLUIDS, AND MECHANICAL PROPERTIES OF NANOSTRUCTURES

A Dissertation
Presented for the
Doctor of Philosophy
Degree
The University of Tennessee, Knoxville

Jose´Luis Rivera-Rojas
May 2003

# Acknowledgements

I would like to thank to my advisors Peter Cummings and Clare McCabe for their support, faith, patience, but mainly to the open and nice environment of work that they have around their research groups. I also like to thank Drs. Jose Alejandre, Marco Mora, Robin Sagar, and Enrique Diaz from the Chemistry and Physics departments at Universidad Autonoma Metropolitana – Iztapala, for their encouragement to realize these doctoral studies. To my mother Conchita, my brother Mauricio and sister Jessica for their support and love. Finally to my friends Enrique Lima, Vicky de la Garza, and Hung-Chih Li for their support and help.

These studies were supported in part by Consejo Nacional de Ciencia y Tecnología (CONACyT) de México under grant number 118657 and the Division of Chemical Sciences, Geosciences, and Biosciences, Office of Basic Energy Sciences, US Department of Energy.

# Abstract

Molecular simulation is a very powerful technique that allows us to predict thermodynamic and transport properties of bulk and confined phases, as well as phase equilibria and interfacial properties. These properties are often crucial to the design of chemical and related industrial processes. Molecular simulation can predict these properties over a wide range of conditions, in contrast with experiments, which at extreme conditions (e.g., high temperature and/or high pressure) are often very difficult and in some cases dangerous. Furthermore, semi-empirical and empirical engineering models can frequently only be used for the specific systems to which they are fitted – that is, they are interpolative rather than predictive. Therefore molecular modeling methods, including simulation, can play a very useful role in the design of new processes, as well as the prediction of new phenomena.

In this thesis, we applied molecular simulation methods to four separate problems: vapor-liquid equilibrium for a polarizable model of water, liquid-liquid interfacial properties, phase equilibrium in confined systems, and mechanical properties of nano scale systems.

The first three problems imply the study of phases in equilibrium under different conditions. The most simple is the vapor-liquid equilibrium of a single component.

Thermophysical properties such as coexistence densities, vapor pressure, surface tension, and interfacial thickness were obtained for a polarizable model of water and compared with other simpler potential models and experimental results. Using the same methodology, the interfacial properties of binary and ternary mixtures with polar and non-polar fluids exhibiting liquid-liquid equilibrium were studied. The dependence of the interfacial properties with increasing molecular size of one compound was studied. For ternary mixtures, the presence of a surfactant molecule was studied at different concentrations of the surfactant. Phase equilibria inside single carbon nanotubes were studied for single and binary aqueous systems, the coexistence liquid densities were calculated and compared with results of water in hydrophobic nanopores, and in the bulk. The phase equilibria behavior was studied indirectly in terms of the pressure inside the nanotube.

Molecular simulation is a very suitable tool to study mechanical properties of systems at the nanoscale. The interlayer friction forces in double-wall carbon nanotubes were studied for systems with axial length up to 100 nm. The oscillatory behavior resulting when the inner tube is pulled out and released was studied as a function of nanotube length, temperature, and internal conformation. The latter enabled the study of systems with different degree of commensurability.

# Contents

# List of Tables

# List of Figures

# Part 1. Vapor-liquid equilibrium simulations of the SCPDP model of water

# Summary

Molecular simulations were carried out using the self-consistent point dipole polarizability model (SCPDP) of water in the region of vapor-liquid equilibrium. The methods of isothermal-isochoric molecular dynamics (NVT-MD) and Gibbs ensemble Monte Carlo (GEMC) were employed to calculate orthobaric densities and vapor pressures; NVT-MD also yields surface tensions and interface thickness. Agreement was found between the two methods, particularly at lower temperatures, but compared with experimental results, this model over-predicts vapor pressures and densities, and under-predicts the liquid density, surface tension, and interface thickness. The interface thickness predicted by the SCPDP model showed better agreement with experimental results than a simpler extended point charge model (SPC/E). ). The results of this work were published as J.L. Rivera, M. Predota, A.A. Chialvo, and P.T. Cummings, “Vapor–liquid equilibrium simulations of the SCPDP model of water,” *Chemical Physics Letters*, **357**, 189 (2002).

# 1.1 Introduction

Simple point charge models (Chialvo and Cummings, 1998; Chialvo and Cummings, 1999) are used widely to study condensed phases and phase equilibrium of water. Their major shortcoming is that the effects of polarization,

which play an important role in physico-chemical processes in water, are not explicitly included. Polarizable models incorporate the effect of polarizability by having polarizable sites (Chialvo and Cummings, 1996); depending on the model, point dipoles or point charges are induced at these sites in response to electrostatic fields due the surrounding molecules. Among polarizable models, the SCPDP model accurately describes the pressure and configurational energy at ambient temperature, while retaining the experimental value for the permanent isolated dipole moment. The structure predicted by this model at ambient conditions agrees well with neutron scattering experiments (Chialvo and Cummings, 1996). Although this model is more detailed than simple point charge models, a significant improvement in the description of phase equilibrium at higher temperatures has not been observed (Kiyohara K. *et al.*, 1998).

There are several studies in the literature using polarizable models in inhomogeneous environments using molecular dynamics methods. The effect of polarizability has been included by Wallqvist (1990) to study the behavior of water close to hydrophobic molecules. Chang and Dang (1996) applied the NVT-MD method to study the liquid-liquid mass transfer coefficients for the system tethrachloromethane - water, using polarizable models for both components. Motakabbir and Berkowitz (1991) studied the orientation of molecules of a polarizable model of water at the vapor-liquid interface. There are also in the literature results of simulations using the GEMC method in the vapor- liquid

region for several polarizable models of water, including the SCPDP model (Kiyohara *et al.*, 1998; Predota *et al.*, 2001), and the polarizable version of the SPC model by Chen *et al.* (2000). These simulations showed that most of these models under-, and over-predict the liquid and vapor orthobaric densities, respectively. Although the SPC/E and the polarizable version of SPC produced better coexisting densities compared to other complex polarizable models, they fail to predict other properties in the vapor phase (SPC/E) and the structure of the liquid phase (SPC polarizable).

The NVT-MD method is a useful and practical tool to study properties in the bulk and at the interface formed between the vapor and liquid phases. It has been applied to study polar (Alejandre *et al.*, 2000) and non-polar (Alejandre *et al.*, 1995) molecules, and its mixtures (Rivera *et al.*, 2000). Compared with the GEMC method, NVT-MD requires more computing time because it simulates a thin liquid film between two vapor phases. This approximation to a bulk vapor-liquid system requires larger systems than the GEMC method, which simulates two systems in the corresponding bulk phases in thermodynamic equilibrium. The advantage of NVT-MD over GEMC is that NVT-MD includes an interface allowing it to be used to study interfacial properties.

# 1.2 Potential model and methodology

The SCPDP water model developed by Chialvo and Cummings (1996) consists of four sites, two of them (H) located at the hydrogen atoms are positively charged, one Lennard-Jones site at the oxygen atom (O), and one site negatively charged (M) along the H-O-H bisector, 0.1 Å away from the oxygen atom. The model has a planar configuration with an H-O-H angle of 109.5°, and an O-H bond length of 1.0 Å. The magnitude and location of the charges correspond to a permanent dipole moment of 1.855 D (Eisenberg and Kauzman, 1969), which agrees with the dipole momentum of an isolated molecule of water. The interactions of this model consist of Lennard – Jones interactions between O-O pairs ($\sigma$ = 3.221 Å, $\varepsilon/k$ = 92.56 K, $k$ = Boltzmann constant), and M-M, M-H, and H-H electrostatic pair interactions. An isotropic point-dipole polarizability is included at the center of mass to account for the many-body polarizable effects.

The induced dipole moment $\mathbf{p}_i$ at the center of mass of molecule $i$ is given by:

$$\mathbf{p}_i = \alpha \mathbf{E}_i = \alpha\left(\mathbf{E}_i^{\mathrm{q}} + \mathbf{E}_i^{\mathrm{p}}\right) \tag{1.1}$$

where $\alpha$ = 1.444 Å$^3$ (Eisenber and Kauzman, 1969) is the scalar molecular polarizability, $\mathbf{E}_i$ is the total electric field at the center of mass of molecule $i$, and

$\mathbf{E}_i^q$, $\mathbf{E}_i^p$ are the contributions from the permanent charges and induced dipoles respectively.

NVT-MD simulations of the vapor-liquid interface were carried out using a Gear's fourth-order predictor corrector algorithm (Gear, 1966) with a Nose´ thermostat (1984) in the NVT ensemble. Systems simulated employed 1000 molecules of water. The simulation cell was a rectangular parallelepiped of dimensions 25.77 Å x 25.77 Å x 128.85 Å. The initial configuration consists of a cubic cell in an FCC arrangement. The range of temperatures studied was 300 to 520 K, and the cutoff radius was 12.88 Å. Periodic boundary conditions were used along with the minimum image criterion. Statistical averages of the properties were made using 400,000 configurations, with previous 200,000 configurations for equilibration.

The molecular reaction field (Chialvo and Cummings, 1996; Hertzner et al., 1991; Garzon et al., 1994) with a dielectric constant of 78 (Steinhauser, 1982) was used to correct long ranged electrostatic interactions. Corrections to the Lennard-Jones forces due to the inhomogenity of the system in the *z*-direction were applied using the expression developed by Mecke *et al*. (1997), i. e.,

$$\Delta F_{i,z}/8\pi = -\int_{-\infty}^{-r_c} dz_{ij}\rho(z_j)\left(z_{ij}^{-11} - z_{ij}^{-5}\right) - \int_{r_c}^{\infty} dz_{ij}\rho(z_j)\left(z_{ij}^{-11} - z_{ij}^{-5}\right) \tag{1.2}$$

where $\Delta F_{i,z}$ is the additional force acting on particle $i$ in the $z$-direction, $z_{ij}$ is the component of the distance between oxygen atoms in the $z$-direction, and $\rho(z_j)$ is the local density, which can be obtained from the density profile. The system is homogeneous in the $x$-, and $y$-directions.

Vapor and liquid densities were obtained by fitting the density profile $\rho(z)$ to a hyperbolic tangent function (Chapela et al., 1977) of the form

$$\rho(z) = 0.5(\rho_L + \rho_V) - 0.5(\rho_L - \rho_V)\tanh\left[\frac{z - z_0}{d}\right] \tag{1.3}$$

where $\rho_L$, $\rho_V$ are the liquid and vapor densities, $z_0$ is the position of the Gibbs' dividing surface, and $d$ is a parameter related to the thickness of the interface.

The element $P_{\alpha\beta}$ of the molecular pressure tensor (Harris, 1992) is given by:

$$VP_{\alpha\beta} = \sum_{i=1}^{N} m_i (\mathbf{v}_i)_\alpha (\mathbf{v}_i)_\beta + \sum_{i=1}^{N}\sum_{j>i}^{N}\sum_{a=1}^{4}\sum_{b=1}^{4} (\mathbf{r}_{iajb})_\alpha (\mathbf{f}_{iajb})_\beta \tag{1.4}$$

where $V$ is the volume of the system, $m_i$ and $\mathbf{v}_i$ are the mass and velocity of molecule $i$. $\mathbf{r}_{iajb}$ and $\mathbf{f}_{iajb}$ are the separation and force between site $a$ in molecule

$i$ and site $b$ in molecule $j$ respectively. The vapor pressure was calculated using the component $P_{ZZ}$, which represents the normal pressure of the system. Surface tension values were obtained by

$$\gamma = \frac{1}{2A}\left[P_{ZZ} - 0.5\left(P_{XX} + P_{YY}\right)\right] \tag{1.5}$$

where $A$ is the surface area of the interface.

For comparison purposes, the coexisting densities and vapor pressure were also calculated using the GEMC method. Details concerning these calculations and the method used can be found in the paper of Predota *et al.* (2001).

# 1.3 Results

Results for the simulations using the NVT-MD method for thermophysical and interfacial properties are listed in Table 1.1 for temperatures in the range of 300 to 500 K. The corresponding thermophysical properties using the GEMC method are listed in Table 1.2 for temperatures in the range of 350 to 520 K. The interface formed by the NVT-MD method was unstable with respect to thermal fluctuations for temperatures above 500 K.

Table 1.1: Average liquid density $\rho_L$, vapor density $\rho_V$, vapor pressure $P_V$, surface tension $\gamma$, and interface thickness $t$, from NVT-MD method.

| $T$ (K) | $\rho_L$ (g/cm$^3$) | $\rho_V$ (g/cm$^3$) | $P_V$ (bar) | $\gamma$ (mN/m) | $t$ (A$^\circ$) |
|---|---|---|---|---|---|
| 300 | 0.984 | 0.001 | 0.15 | 51.5 | 3.16 |
| 350 | 0.937 | 0.002 | 3.30 | 39.2 | 4.42 |
| 400 | 0.868 | 0.010 | 9.97 | 25.0 | 6.14 |
| 450 | 0.779 | 0.022 | 37.16 | 17.2 | 8.14 |
| 480 | 0.699 | 0.040 | 67.02 | 12.4 | 10.34 |
| 500 | 0.621 | 0.067 | 95.73 | 8.1 | 11.66 |

Table 1.2: Average liquid density $\rho_L$, vapor density $\rho_V$, and vapor pressure $P_V$ from GEMC method.

| $T$ (K) | $\rho_L$ (g/cm$^3$) | $\rho_V$ (g/cm$^3$) | $P_V$ (bar) |
|---|---|---|---|
| 350 | 0.927 | 0.001 | 1.16 |
| 400 | 0.874 | 0.004 | 7.60 |
| 450 | 0.797 | 0.019 | 32.42 |
| 480 | 0.719 | 0.031 | 53.93 |
| 500 | 0.653 | 0.061 | 98.05 |
| 510 | 0.577 | 0.077 | 116.21 |

The resulting temperature-density phase envelope using GEMC and NVT-MD methods is shown in Figure 1.1 for the SCPDP model of water, in comparison with experimental data (Haar *et al.*, 1984), published results using the GEMC method (Kiyohara *et al.*, 1998), and published results using the NVT-MD method for the SPC/E model of water (Alejandre *et al.*, 1995). Results from this work using GEMC and NVT-MD methods agree for vapor densities, and for liquid densities agree from 300 to 450 K; beyond this temperature the liquid densities exhibit small differences. Published results using the GEMC method from Kiyohara *et al.* (1998) agree with our results using the same method for vapor densities, and there are small deviations for liquid densities. Compared with experimental results, the SCPDP model of water under- and over-predicts liquid and vapor densities respectively. At 300 K the absolute error in vapor and liquid densities are 0.024 and 0.0125 g/cm$^3$, at 500 K the errors are 0.054 and 0.211 g/cm$^3$ respectively. The SPC/E model predicts coexisting densities in better agreement with experimental results (Alejandre *et al.*, 1995) than the SCPDP model. The critical temperature and density of the SCPDP model of water are 538 K and 0.32 g/cm$^3$ (Kiyohara *et al.*, 1998). The phase envelopes using reduced temperatures ($T/T_C$) are shown in Figure 1.2. The temperatures of each phase envelope were reduced using its own critical temperature. In reduced units, the phase envelope produced by the SCPDP model is in better agreement with the experimental data than the phase envelope produced by the SPC/E model.

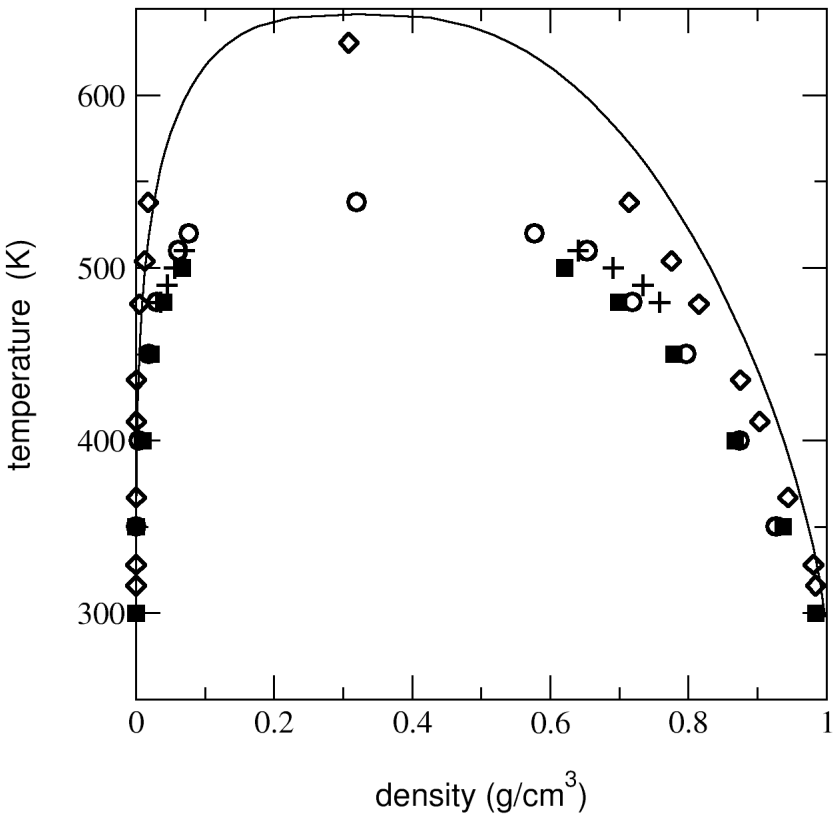


Figure 1.1: Liquid-vapor coexistence curve of water. The solid line represents the experimental data (Haar *et al.*, 1984). Squares and circles represent results from this work using NVT-MD, and GEMC methods, respectively. Crosses represent results for the GEMC method from Kiyohara *et al.* (1998). Diamonds represent results for the SPC/E model from Alejandre *et al.* (1995).

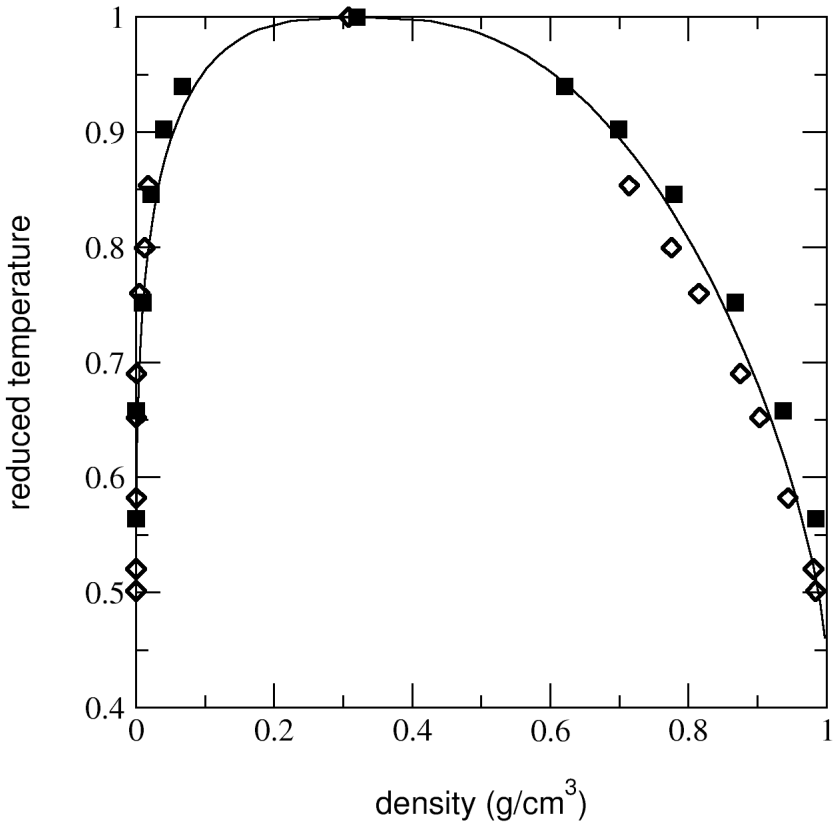


Figure 1.2: Liquid-vapor coexistence curve of water (reduced temperature). Symbols as in Figure 1.1.

Results for vapor pressures using GEMC and NVT-MD methods are shown in Figure 1.3, with published results using GEMC method (Kiyohara *et al.*, 1998), and experimental data (Haar *et al.*, 1984). Results from this work using GEMC and NVT-MD methods agree for temperatures up to 400 K; beyond this temperature the vapor pressures calculated using NVT-MD are higher than those obtained by the GEMC method. Published results from Kiyohara *et al*. (1998) using the GEMC method in the range of temperatures between 480 and 510 K agree with our calculations using the same method. Compared with experimental results, all simulations over-predict the experimental vapor pressures in the range of temperature studied. Using reduced temperatures (Figure 1.4), the corresponding vapor pressures under-predict the experimental data; these results are consistent with their corresponding phase envelope (Figure 1.2), where the vapor densities under-predict the experimental data.

The results for surface tension of the SCPDP model are shown in Figure 1.3, in comparison with experimental data (Vargaftik *et al.*, 1983), and published results for the SPC/E model (Alejandre *et al.*, 1995). Our results for the SCPDP model are well below the experimental results; the absolute error is almost the same for the whole range of temperatures studied, and this is around 22 mN/m. Published results using the SPC/E model from Alejandre *et al*. (1995) agree with experimental results. A simple linear regression was performed on our results, which is shown as a dashed line in Figure 1.3; an extrapolation of this curve to a

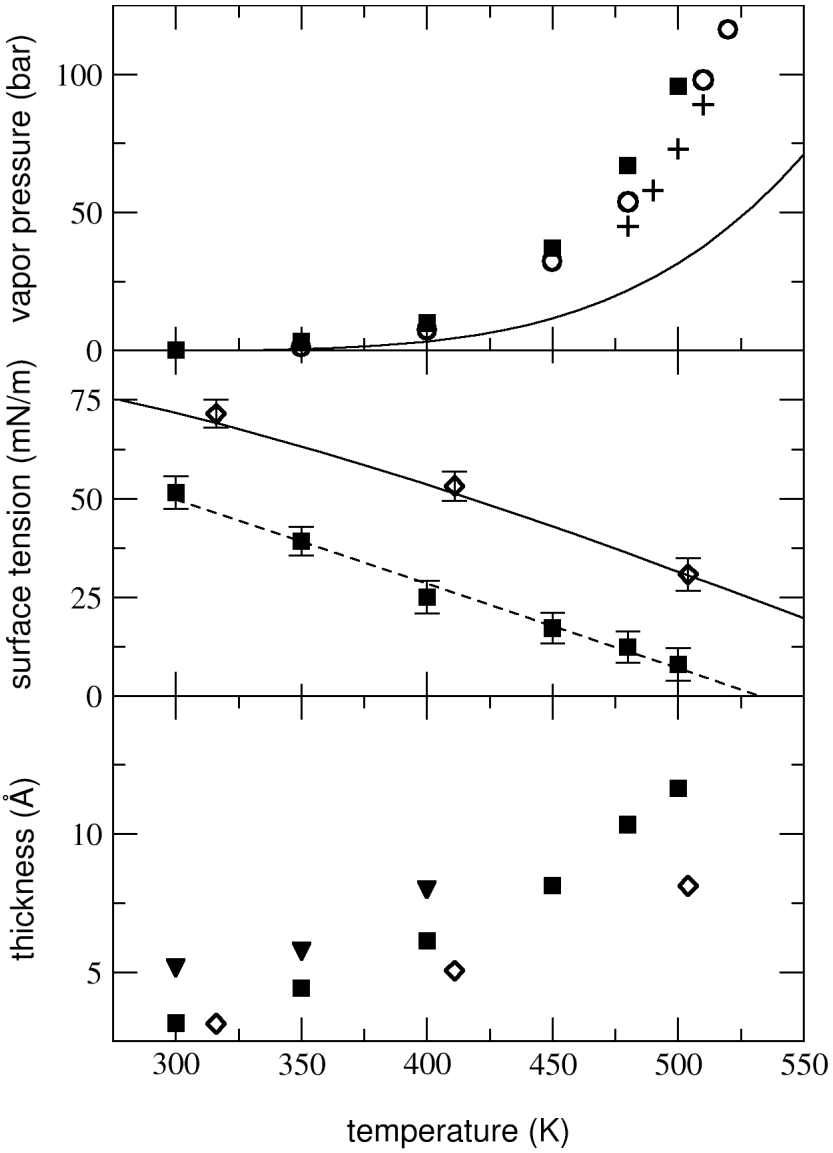


Figure 1.3: Vapor pressure, surface tension and interfacial thickness of water. The solid lines represent experimental data (Haar *et al.*, 1984; Vargaftik *et al.*, 1983) for vapor pressure and surface tension. Triangles represent experimental data (Matsumoto and Kataoka, 1988) for interfacial thickness. The remaining symbols as in Figure 1.1.

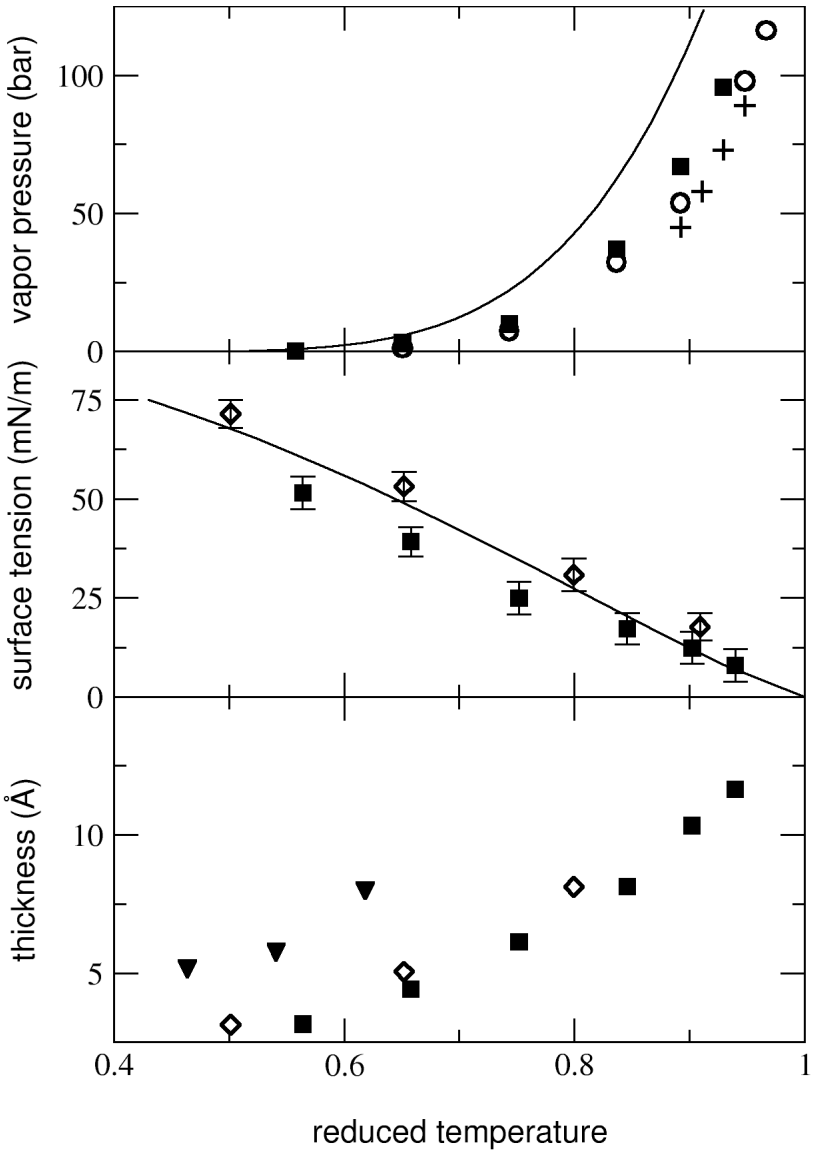


Figure 1.4: Vapor pressure, surface tension and interfacial thickness of water (reduced temperature). Symbols as in Figures 1.1 and 1.3.

value of 0 mN/m of surface tension produced a value of 532.54 K for the critical temperature, which differs by 1 % from the value reported by Kiyohara *et al.* (1998). In terms of reduced temperatures (Figure 1.4), our results are in better agreement with experimental results, particularly at higher temperatures.

The thickness of the interface was calculated using the data obtained from the fitting of the density profiles to Equation (1.2). The thickness *t*, is related to the parameter $d$ in Equation (1.2) by $t = 2.1972d$ (Chapela *et al.*, 1977). Results of these calculations are shown in Figure 1.3 with published results for the SPC/E model (Alejandre *et al.*, 1995) for comparison. The thickness of the interface can be obtained indirectly from ellipsometric and x-ray reflective experiments; results of these experimental studies reported by Matsumoto and Kataoka (1988) are also shown in Figure 1.3, and compared with our results; the absolute error is around 2.2 Å and is effectively constant for temperatures between 300 and 400 K. Compared with results for the SPC/E model, the SCPDP results are closer to the experimental values. Using reduced temperatures (Figure 1.4), results of both models agree with each other, but they do not agree with the experimental data.

# Conclusions

We have presented new calculations for the SCPDP model of water in the region of vapor – liquid coexistence using NVT-MD and GEMC methods. Results from both methods agree at lower and medium temperatures. At higher temperatures, where we expect system size problems with NVT-MD, the methods disagree. As expected based on previous phase equilibria studies compared with simpler models like SPC/E, the SCPDP model of water produces inferior results for phase equilibria, particularly at elevated temperatures, for almost all thermodynamic and interfacial properties studied. The only property that seems to be improved is the interfacial thickness. In terms of reduced temperatures, using the critical temperature of each model to reduce, this model produces better results, which are in concordance with results of the SPC/E model. These results show that the major problem of the SCPDP model is that it produces a very low critical temperature, making the predictions for other properties be in disagreement with experimental data.

Although the SCPDP model has the ability to reproduce properties at ambient conditions, it appears to have limited success in predicting vapor-liquid coexistence. The specific shortcomings of the SCPDP potential are difficult to pinpoint. Generally, polarizable models of water under-predict the phase envelope while simultaneously improving the prediction of other properties. We

are exploring alternative parameterizations of the SCPDP model to attempt to obtain globally better predictions for the model.

# Bibliography


Alejandre J., Tildesley D. J., and Chapela G. A., Molecular-dynamics simulation of the orthobaric densities and surface-tension of water, *J. Chem. Phys.*, 102, 4574 (1995).

Alejandre J., Tildesley D. J., and Chapela G. A., Fluid-phase equilibria using molecular-dynamics – The surface-tension of chlorine and hexane, *Mol. Phys.*, **85**, 651 (1995).

Alejandre J., Rivera J. L., Mora M. A., and de la Garza V., Force field of monoethanolamine, *J. Phys. Chem. B*, **104**, 1332 (2000).

Chang T., and Dang L. X., Transfer of $CH_4$ across the $H_2O$-$CCl_4$ liquid-liquid interface with polarizable potential models, *Chem. Phys. Lett.*, **263**, 39 (1996).

Chapela G. A., Saville G., Thompson S. M., and Rowlinson J. S., Computer-simulation of gas-liquid surface, *J. Chem. Soc. Faraday Trans. II*, **8**, 133 (1977).

Chen B., Xing J., and Siepmann J. I., Development of polarizable water force fields for phase equilibrium calculations, *J. Phys. Chem. B*, **104**, 2391 (2000).

Chialvo A. A., and Cummings P. T., Engineering a simple polarizable model for the molecular simulation of water applicable over wide ranges of state conditions, *J. Chem. Phys.*, **105**, 8274 (1996).

Chialvo A. A., and Cummings P. T., in *Encyclopedia of Computational Chemistry*, Wiley, New York, **4**, 2839 (1998).

Chialvo A. A., and Cummings P. T., Molecular-based modeling of water and aqueous solutions at supercritical conditions, *Adv. Chem. Phys.*, **109**, 115 (1999).

Eisenberg D., and Kauzman W., *The structure and properties of water*, Oxford, New York, 1969.

Garzon B., Lago S., and Vega C., Reaction field simulations of the vapor-liquid equilibria of dipolar fluids – does the reaction field dielectric constants affect the coexistence properties, *Chem. Phys. Lett.*, **231**, 366 (1994).

Gear W. C., The numerical integration of ordinary differential equations of various orders, Argonne National Laboratory, Report ANL-7126, 1966.

Haar L., Gallagher J. S., and Kell G. S., *NBS/NRC Steam Tables*, Hemisphere, Washington D. C., 1984.

Harris J. G., Liquid vapor interfaces of alkane oligomers – structure and thermodynamics from molecular-dynamics simulations of chemically realistic models, *J. Phys. Chem.*, **96**, 5077 (1992).

Hertzner A. W., Schoen M., and Morgner H., The influence of long-range electrostatic forces on static properties of a quasi-stockmayer fluid, *Mol. Phys.*, **73**, 1011 (1991).

Kiyohara K., Gubbins K. E., and Panagiotopoulos A. Z., Phase coexistence properties of polarizable water models, *Mol. Phys.*, **94**, 803 (1998).

Matsumoto M., and Kataoka Y., Study on liquid vapor interface of water. 1. Simulation results of thermodynamic properties and orientational structure, *J. Chem. Phys.* **88**, 3233 (1988).

Mecke M., Winkelmann J., and Fischer J., Molecular dynamics simulation of the liquid-vapor interface: The Lennard-Jones fluid, *J. Chem. Phys.*, **107**, 9264 (1997).

Motakabbir K. A, and Berkowitz M. L., Liquid-vapor interface of TIP4P water – comparison between a polarizable and a nonpolarizable model, *Chem. Phys. Lett.*, **176**, 61 (1991).

Nose S., A unified formulation of the constant temperature molecular dynamics methods, *J. Chem. Phys.*, **81**, 511 (1984).

Predota M., Cummings P. T., and Chialvo A. A., On the determination of vapor-liquid envelope for polarizable models by Monte Carlo simulations, *Fluid Phase Equil.*, **183**, 295 (2001).

Rivera J. L., Alejandre J., Nath S., and de Pablo J. J., Thermodynamic and transport properties of nitrogen and butane mixtures, *Mol. Phys.*, **98**, 43 (2000).

Steinhauser O., Reaction field simulation of water, *Mol. Phys.*, **45**, 335 (1982).

Vargaftik N. B., Volkov N. B., and Voljak L. D., International tables of the surface-tension of water, *J. Phys. Chem. Ref. Data*, **12**, 817 (1983).

Wallqvist A., Polarizable water at hydrophobic wall, *Chem. Phys. Lett.*, **165**, 437 (1990).

# Part 2. Liquid-Liquid interfacial properties: Water / *n*-alkane and water + methanol / *n*-alkane systems

# Summary

Direct molecular dynamics simulations of the liquid-liquid interface of water–*n*-alkane and water–methanol–*n*-alkane systems have been performed in order to study the interfacial properties of these systems. The simulations were carried out using the NERD revised force field of Nath *et al.* for the *n*-alkanes, the simple point charge extended (SPC/E) model for water, and the optimized potential for liquid simulations (OPLS) model for methanol. In order to validate the model employed in this work for the *n*-alkanes we calculated the coexisting densities, surface tension, and thickness of the interface for pure *n*-pentane. For all the systems studied the interfacial tension and thickness were calculated at 298.15 K. Our results show that, by adjusting the number of molecules to reproduce the liquid densities in the direct simulation method of the liquid-liquid interface in multicomponent systems, we are able to reproduce available experimental data for interfacial tension. The interfacial thickness is underpredicted and a constant negative deviation of ~ 2.5 Å from the experimental data is usually observed. We find that methanol acts like surfactant when it is added to the water–*n*-alkane mixtures, reducing the interfacial tension of the liquid-liquid ternary system. The interfacial tension results agree quantitatively well for the range of concentrations of methanol studied. The results of this work were written up as J. L. Rivera, C. McCabe, and P. T. Cummings, “Molecular simulations of liquid-liquid interfacial

properties: Water/n-alkane and water + methanol/n-alkane systems," which has been accepted for publication in *Physical Review E*.

## 2.1. Introduction

Oil-water and oil-water-surfactant systems are very important in many scientific and technological aspects. Practical applications in biological systems (Stryer, 1995), drug delivery (Arai *et al*., 1996), food processing (Dickinson *et al*., 1990), and detergents (Morrow, 1991), have been the subject of extensive experimental studies in recent years. Of particular relevance is the use of water flooding in enhanced crude oil recovery (Morrow, 1991), a procedure that is designed to maintain the reservoir pressure while oil is extracted through the oil well. During water flooding, capillary action causes significant retention of oil behind the flood front. This trapped oil can be recovered using surfactants, which reduce the oil-water interfacial tension by several orders of magnitude, making it feasible to mobilize and recover the oil (Morrow, 1991).

Among the properties that can be studied at the interface, two characterize liquid-liquid and vapor-liquid interfaces: interfacial tension (or surface tension for pure component systems), and density profiles (which also describe the interfacial

thickness). Several experimental studies at 298.15 K and 1 atm report liquid-liquid interfacial tension for water–*n*-alkane systems (Sachs and Meyn, 1995; Goebel and Lunkenheimer, 1997; Matsubara et al., 1988), the vapor-liquid interfacial thickness of pure water [8], long *n*-alkanes ($C_{20}$ and $C_{36}$) (Ocko et al., 1994), and liquid-liquid interfacial thickness of water–*n*-alkane systems (Mitrinovic *et al.*, 1999; Mitrinovic *et al.*, 2000). However measurements at conditions similar to those in an oil reservoir are scarce (Jennings and Newman, 1971) because of the difficulties performing experiments under such conditions (Sachs and Meyn, 1995). While predictions of the interfacial tension using equations of state have been reported, the lack of equations of state which adequately describe phase equilibria of water–*n*-alkane systems is an impediment to producing accurate results for interfacial properties at the specified conditions (Zuo and Stenby, 1998). For some water–*n*-alkane systems with less than 12 carbons in the *n*-alkane chain, theoretical predictions of the interfacial thickness using capillary-wave theory (Buff *et al.*, 1965; Sferraza *et al.*, 1997) have produced excellent results. In capillary-wave theory, besides the contribution from the interfacial thickness that corresponds to the intrinsic structure of the interface, there is a second contribution due to the roughness of the interface propagated by thermally excited capillary waves. The contribution due to the intrinsic structure of the interface for water–*n*-alkane systems can be estimated as the radius of gyration of the larger compound of the system (Mitrinovic *et al.*, 2000).

Molecular simulations have been reported in the literature which investigate the influence of surfactant concentration on the interfacial tension of model Lennard-Jones ternary systems (Smit, 1988; Diaz-Herrera, 1999). Smit (1988) showed that in the model system the interfacial tension decreases almost linearly with the concentration of surfactant at the interface. However, the results in this study were influenced by the size of the system due to the small number of molecules employed. Diaz-Herrera *et al.* (1999) studied larger system sizes and concluded that the dependence is not linear. To our knowledge there are only five simulations reported in the literature using realistic potentials for water–*n*-alkane and water–surfactant–*n*-alkane systems. Water–*n*-hexane was studied by Carpenter and Hehre (1990), water–*n*-octane by Zhang *et al.* (1995), water–*n*-nonane by Michael and Benjamin (1995), water–*n*-decane by van Buuren *et al.* (1993), and water–monododecyl pentaethylene glycol–*n*-octane by Kuhn and Rehage (2000). Hence it has been shown that using direct molecular dynamics simulations we are able to characterize the interface of a system, though the accuracy of the results will naturally depend upon the accuracy of the potential model employed for each compound and to some extent on the combining rules used to determine the unlike interactions between the molecules in the system. Furthermore, when dealing with polar molecules, consideration needs to be given to the way long-range electrostatic interactions are computed, since they can represent up to 25% of the total value of the interfacial properties (Alejandre *et al.*, 1995; Rivera *et al.*, 2002). However, of the previous simulation studies using

realistic potentials, one of them does not specify the method employed to calculate long-range electrostatic interactions (van Buuren *et al.*, 1993) and the remainder simply do not account for these interactions (Carpenter and Hehre, 1990; Zhang *et al.*, 1995; Michael and Benjamin, 1995; Kuhn and Rehage, 2000). All prior simulation studies obtained results for the interfacial thickness that disagree with the available experimental data (Mitrinovic *et al.*, 2000) with relative errors as large as 40 % for the simulation with *n*-hexane. Only Zhang *et al.* (1995) and van Buuren *et al.* (1993) actually calculated interfacial tensions; they obtained poor results with an all atom model of *n*-alkanes (Zhang *et al.*, 1995) and the Ryckaert-Bellemans model (Ryckaert and Bellemans, 1978).

In this work, we performed new realistic simulations of the water–*n*-alkane and water–methanol–*n*-alkane interface using the Ewald summation technique, which accurately describes the long-rang electrostatic interactions. We initially performed simulations to obtain a system at the correct density and compositions in the bulk phases compared to experimental data. The interfacial properties (density profiles, interfacial thickness and tension) were then calculated from the resulting configurations.

## 2.2. Methodology

We have performed direct molecular dynamics simulations (NVT-MD) of the vapor-liquid and liquid-liquid interfaces to obtain the coexisting densities and interfacial properties (interfacial thickness and surface and interfacial tensions) for pure *n*-pentane, the interfacial properties of binary mixtures of water–*n*-alkane, and the ternary mixture of water–methanol–*n*-pentane. All the simulations were carried out using the Verlet algorithm at constant temperature; the time step used was 1 fs. Depending on the *n*-alkane chain length the simulation cell contained between 150 and 350 *n*-alkane molecules, 100 to 540 water molecules, and 50 to 220 methanol molecules. The simulations were performed at ambient temperature for the liquid-liquid simulations and from 150 to 336 K for the vapor-liquid simulations of pure *n*-pentane.

The potential model parameters used to describe the water, methanol, and *n*-alkane molecules were taken from references (Berendsen *et al.*, 1987), (Jorgensen, 1981), and (Nath *et al.*, 1998) respectively. The reader is directed to the original references for details of each potential model. The intermolecular forces due to Lennard-Jones interactions were computed using an spherically truncated potential (Trokhymchuck and Alejandre, 1999). The interaction is given by

$$F_{LJ}\left(r_{iajb}\right)=\begin{cases}\dfrac{24\varepsilon}{r_{iajb}}\left[2\left(\dfrac{\sigma}{r_{iajb}}\right)^{12}-\left(\dfrac{\sigma}{r_{iajb}}\right)^{6}\right]-U_{LJ}\left(r_c\right)\delta\left(r_{iajb}-r_C\right), & r_{iajb}\le r_C \\ 0, & r_{iajb}>r_C\end{cases} \tag{2.1}$$

where $\sigma$ and $\varepsilon$ are the Lennard-Jones parameters, $r_C$ is the cut-off radius and $r_{iajb}$ is the distance between site $a$ in molecule $i$ and site $b$ in molecule $j$. $U_{LJ}$ is the simple Lennard-Jones potential and $\delta$ is a delta function, which is approximated by:

$$\delta\left(r_{iajb}-r_C\right)=\frac{\theta\left(r_{iajb}-r_C\right)-\theta\left(r_{iajb}-r_C-\Delta r\right)}{\Delta r} \tag{2.2}$$

where $\theta$ is the unit step function and $\Delta r$ a fixed parameter. Using Equation (2.1) to compute the interaction forces with a cutoff ratio greater than $4\sigma_{MAX}$ ($\sigma_{MAX}$ is the largest Lennard-Jones sigma parameter among the values used for the species studied), we can obtain more precise values for the interfacial properties compared to results using spherically truncated and shifted potentials. Sites in the same molecule separated by three of more bonds interact through the potential given in Equation (2.1). The Lorentz-Berthelot mixing rules were used for the cross interaction between unlike sites.

The procedure used in this work to simulate liquid-liquid equilibria is the same as that employed to simulate the liquid-vapor interface of one component or multicomponent systems (Alejandre *et al.*, 2000; Rivera and Alejandre, 2002). At the beginning of the simulation, molecules are allocated in the center of a parallelepiped cell surrounded by vacuum in the *z*-direction. The dimensions of the simulation cell vary depending upon the particular system being studied. A typical size of $L_X = L_Y = 31.44$ Å, and $L_Z = 125.76$ Å for liquid-vapor equilibria, and $L_X = L_Y = 31.44$, and $L_Z = 66.81$ Å for liquid-liquid equilibrium was used. The cut-off radius for Lennard-Jones interactions was 15.72 Å. Electrostatic interactions were handled by the Ewald summation technique with a convergence parameter $\kappa$ of $5.6/L_Z$ and a maximum value for the reciprocal lattice vector $h_{MAX}$ of 10. After an equilibration period of 150 ps the average properties were then obtained from an additional simulation run of 600 ps.

The coexistence densities and compositions were obtained following the same procedure described in reference (Rivera and Alejandre, 2002). During the vapor-liquid simulations, a molecular density profile was obtained and fitted to a hyperbolic tangent function (Alejandre *et al.*, 1995) in order to obtain the coexistence densities, viz.:

$$\rho(z) = 0.5(\rho_L + \rho_V) - 0.5(\rho_L - \rho_V)\tanh\left[\frac{z - z_0}{d}\right] \qquad (2.3)$$

where $\rho_L$, $\rho_V$ are the liquid and vapor densities, $z_0$ is the position of the Gibbs dividing surface, and $d$ is a parameter related to the thickness of the interface. The thickness of the interface is calculated as the distance along the interface over which the density changes from a value of 10% to 90% of the total density change between the bulk phases, which corresponds to 2.1972 times the value of parameter $d$ (Alejandre *et al.*, 1995). As a result, this thickness is known as the "10-90" interfacial thickness; a frequently used alternative thickness is the "10-50" interfacial thickness which is defined analogously.

For systems exhibiting liquid-liquid equilibrium, the thickness of the liquid-liquid interface was calculated using the criteria proposed by Senapti and Berkowitz (2001), which results in a prediction for the "10-50" interfacial thickness. The density profile of each component is fitted to an expression similar to the one used to fit the experimental data in liquid-liquid water-*n*-alkane systems (Mitrinovic *et al.*, 2000).

$$\rho_W(z) = 0.5\rho_{WB} + 0.5\rho_{WB}\mathrm{erf}\left[\frac{z - \langle z_W \rangle}{\sqrt{2}t_C}\right] \tag{2.4}$$

$$\rho_A(z) = 0.5\rho_{AB} + 0.5\rho_{AB}\mathrm{erf}\left[\frac{z - \langle z_A \rangle}{\sqrt{2}t_C}\right] \tag{2.5}$$

where $\rho_W(z)$, and $\rho_A(z)$ are the density profiles of water and *n*-alkane respectively. $\rho_{WB}$, and $\rho_{AB}$ are the water and *n*-alkane bulk densities respectively. $\langle z_W \rangle$ and $\langle z_A \rangle$ are the average positions of each interface, $t_C$ is the contribution to the "10-50" interface thickness due to thermal fluctuations, and $\mathrm{erf}$ is the error function. The intrinsic interfacial thickness $t_0$ is obtained as $|\langle z_A \rangle - \langle z_W \rangle|$, the difference between the positions of the fitted interfaces.

The surface and interfacial tensions were calculated using the molecular definition of the pressure tensor. The molecular surface tension is defined in terms of the pressure tensor components as (Alejandre *et al.*, 2000):

$$\gamma = \frac{L_Z}{2}\left[\langle P_{ZZ} \rangle - 0.5\left(\langle P_{XX} \rangle + \langle P_{YY} \rangle\right)\right] \tag{2.6}$$

where $P_{\alpha\alpha}$ is the $\alpha\alpha$ element of the pressure tensor. The factor (1/2) outside the bracket takes into account the fact that there are two interfaces in the system. Brackets for each $P_{\alpha\alpha}$ indicate temporal averages. The element $P_{\alpha\beta}$ of the molecular pressure tensor for additive pair potentials, as is the case of Lennard Jones is given by

$$VP_{\alpha\alpha} = \sum_i^N m_i(\mathbf{v}_i)_\alpha(\mathbf{v}_i)_\alpha + \sum_i \sum_{j>i} \sum_a \sum_b (\mathbf{r}_{iajb})_\alpha (\mathbf{f}_{iajb})_\alpha \tag{2.7}$$

where $N$ is the number of molecules, $V$ is the volume of the system, $m_i$ is the molecular mass, $(\mathbf{v}_i)_\alpha$ is the velocity of the center of mass in the $\alpha$-direction, $(\mathbf{r}_{iajb})_\alpha$ and $(\mathbf{f}_{iajb})_\alpha$ are the distance and interaction force between site $a$ in molecule $i$ and site $b$ in molecule $j$ in the $\alpha$-direction. For pure component simulations we can compute long-range corrections to the surface tension due to Lennard-Jones interactions beyond the cutoff ratio (Alejandre *et al.*, 1995). For *n*-pentane the expression is given by

$$\gamma_{LRC} = 12\pi(\rho_L - \rho_V)^2 \sum_{a=1}^{5}\sum_{b=1}^{5} \varepsilon_{ab}\sigma_{ab}^6 \int_0^1 ds \int_{r_C+\Delta r}^{\infty} dr \coth\left(\frac{rs}{d}\right)\frac{(3s^3 - s)}{r^3} \tag{2.8}$$

where $\rho_L$ and $\rho_V$ are the liquid and vapor coexisting densities. $\varepsilon_{ab}$ and $\sigma_{ab}$ are the cross Lennard-Jones parameters.

Using the Ewald summation technique, the reciprocal space contribution is not pair wise additive and Equation (2.7) cannot be used. The components for the pressure tensor or electrostatic interactions have already been obtained by Alejandre *et al.* (1995, 2000). For completeness we give only the basic equations here:

$$VP_{\alpha\alpha} = \sum_i \sum_a q_{ia} \sum_{j>i} \sum_b q_{jb} \left[ \frac{2}{\sqrt{\pi}} \kappa r_{iajb} \exp\left(-\kappa^2 r_{iajb}^2\right) + \operatorname{erfc}\left(\kappa r_{iajb}\right) \right] \frac{\left(\mathbf{r}_{ij}\right)_\alpha \left(\mathbf{r}_{iajb}\right)_\beta}{r_{iajb}^3}$$
$$+ \frac{2\pi}{V} \sum_{\mathbf{h}\neq\mathbf{0}} Q(h) S(\mathbf{h}) S(-\mathbf{h}) \left( \delta_{\alpha\beta} - \frac{2\mathbf{h}_\alpha \mathbf{h}_\beta}{h^2} - \frac{\mathbf{h}_\alpha \mathbf{h}_\beta}{2\kappa^2} \right) - \sum_i \sum_a \left(\mathbf{r}_{ia} - \mathbf{r}_i\right)_\beta \left(\mathbf{f}_{ia}^\kappa\right)_\alpha \tag{2.9}$$

$$S(\mathbf{h}) = \sum_i \sum_a q_{ia} \exp\left(i\mathbf{h} \cdot \mathbf{r}_{ia}\right) \tag{2.10}$$

$$Q(h) = \exp\left(-h^2 / 4\kappa^2\right) / h^2 \tag{2.11}$$

$$\mathbf{f}_{ia}^\kappa = -\frac{4\pi q_{ia}}{V} \sum_{\mathbf{h}\neq\mathbf{0}} Q(h) \mathbf{h} \operatorname{Im} ag\left[\exp\left(-i\mathbf{h} \cdot \mathbf{r}_{ia}\right) S(\mathbf{h})\right] \tag{2.12}$$

where $\mathbf{h}$ is the reciprocal lattice vector, $\delta$ is the Kronecker delta, erfc is the complementary error function, and Imag denotes the imaginary part of the complex variable.

# 2.3 Results

## 2.3.1. Vapor-liquid equilibrium results for *n*-pentane

The potential chosen to model the *n*-alkanes was validated for interfacial properties through NVT-MD simulations and the results are presented in this

section. For the pure *n*-pentane system the results of the simulations of the coexisting densities, "10-90" interfacial thickness and surface tension as a function of temperature are given in Table 2.1. Densities and interfacial thickness were obtained from density profiles fitted to Equation (2.3). Bulk phases extended for more than 50 Å with stable interfaces during the simulations. Our calculated densities agree well with experimental data (Smith and Srivarasta, 1986) having maximum absolute errors of 0.035 g/cm$^3$, which are similar to the errors obtained by Nath *et al.* (Nath *et al.*, 1998) using the Gibbs ensemble Monte Carlo method. Figure 2.1 illustrates these comparisons.

The results of calculations to determine the "10-90" interfacial thickness as a function of the temperature are shown in Figure 2.2a, where it can be seen that the thickness of the interface grows monotonically with the temperature. The results of this work for *n*-pentane are similar to previously reported results for simulations of *n*-hexane using the OPLS potential (Alejandre *et al.*, 1995), however there is no experimental data or theoretical predictions to which we can compare our results. Calculations of the surface tension are shown as a function of the temperature in Figure 2.2b. The agreement with experimental data (Grygoriev *et al.*, 1992) is excellent in the range of temperatures studied. Long-range corrections represent around 20 % of the total value. Therefore given these results we feel confident in the use of the NERD potential to study interfacial properties of multicomponent systems with water and surfactants.

Table 2.1: Simulation results for *n*-pentane. Average liquid density $\rho_L$, vapor density $\rho_V$, "10-90" interface thickness $t$, surface tension obtained during simulation $\gamma_{SIM}$, its long-range correction $\gamma_{LRC}$, and the total value $\gamma$ as function of temperature. Numbers between parentheses indicate the precision of the total values.

| $T$ (K) | $\rho_L$ (g/cm$^3$) | $\rho_V$ (g/cm$^3$) | $t$ (A°) | $\gamma_{SIM}$ (mN/m) | $\gamma_{LRC}$ (mN/m) | $\gamma$ (mN/m) |
|---|---|---|---|---|---|---|
| 150 | 0.7225 | 0.0001 | 2.62(0.39) | 26.70 | 6.39 | 33.09 (1.60) |
| 200 | 0.6807 | 0.0003 | 3.59 (0.39) | 20.17 | 5.42 | 25.59 (1.33) |
| 270 | 0.6187 | 0.0152 | 6.20 (0.39) | 15.34 | 3.85 | 19.19 (1.15) |
| 336 | 0.5552 | 0.0819 | 9.48 (0.39) | 9.93 | 2.44 | 12.37 (1.38) |

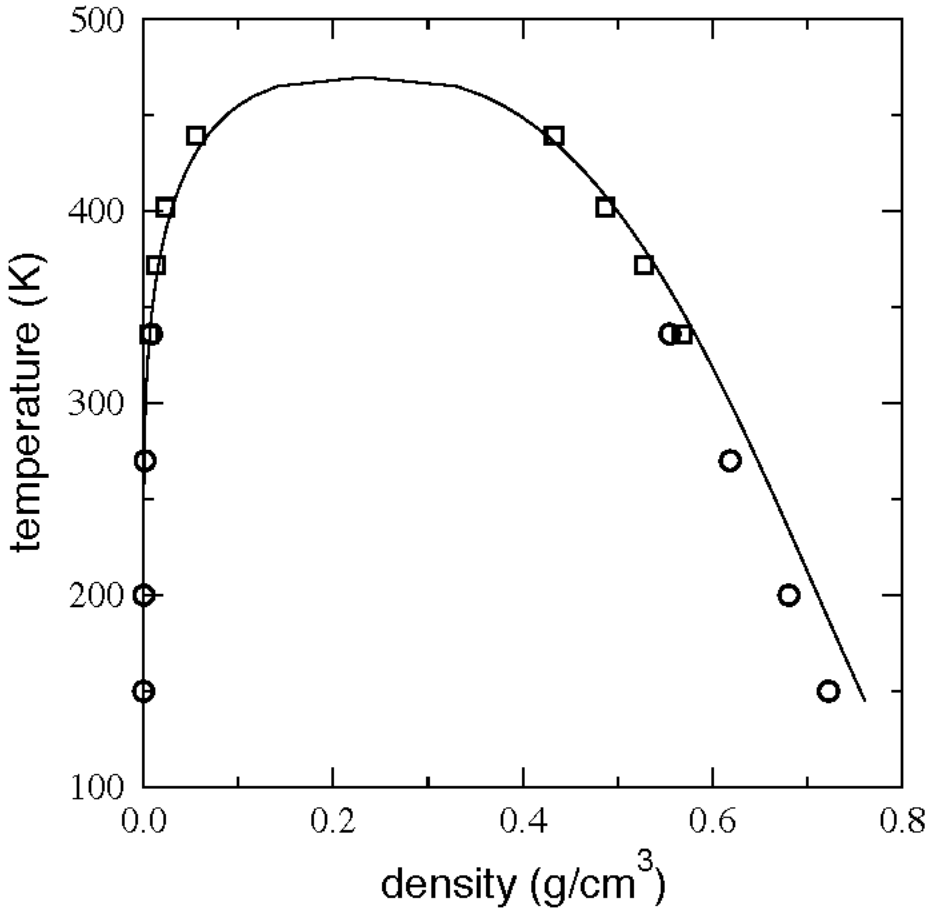


Figure 2.1: Liquid-vapor coexistence curve of *n*-pentane. The solid line represents experimental data (Smith and Srivastava, 1986). Squares and circles represent results from Nath *et al.* (1998) and results from this work respectively.

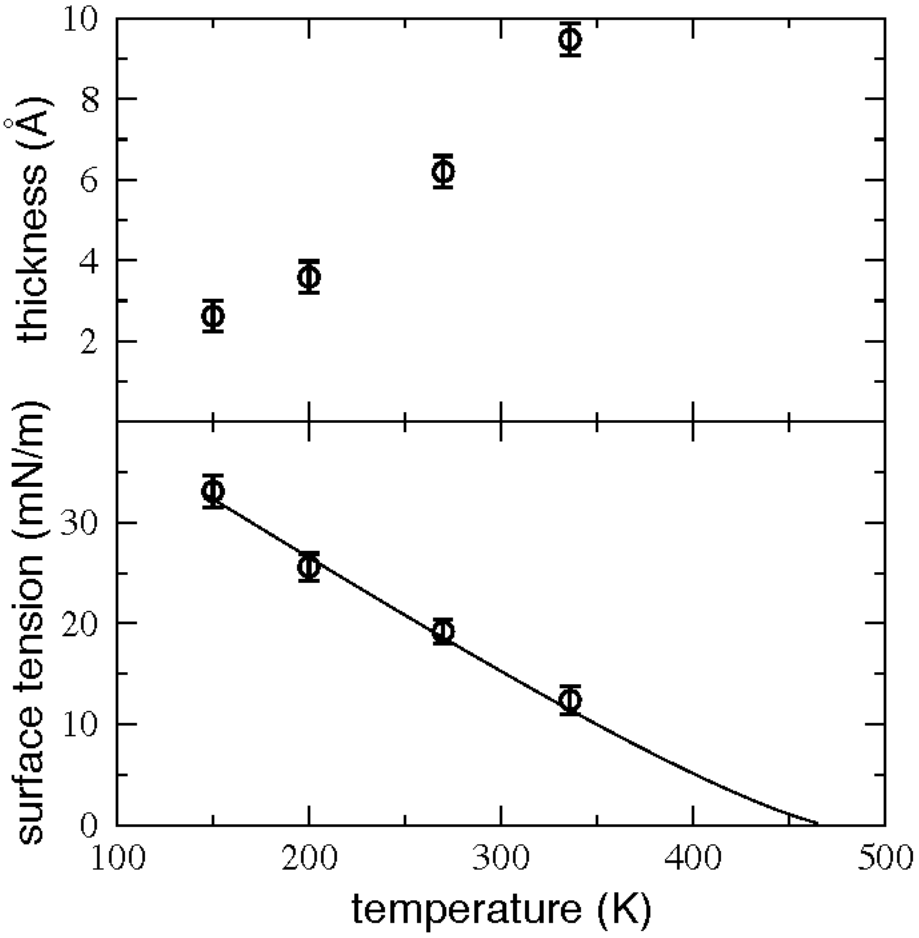


Figure 2.2: The interfacial thickness and surface tension of *n*-pentane as a function of the temperature. a) “10-90” interfacial thickness, and b) surface tension as function of temperature for *n*-pentane. Solid line represents experimental data from Grygoriev *et al.* (1992). Circles represent results from this work.

We did not perform similar validation studies for the water molecules as previous simulations results (Alejandre *et al.*, 1995, Taylor *et al.*, 1996) for the SPC/E model of water show that this model is also suitable for the study of interfacial properties. In particular, Alejandre *et al.* (1995) produced predictions using this model that agree quantitatively well with experimental data for the surface tension and the "10-90" interfacial thickness had an absolute error of ~1.1 Å (~ 33 %) at 298.15 K if the extrapolated simulation result is compared to a measurement of Matsumoto and Kataoka (1988).

## 2.3.2. Liquid-liquid equilibrium for water–*n*-alkane systems

The NVT-MD simulations of the liquid-liquid interface of water–*n*-alkane binary mixtures were carried out at 298.15 K, without considering the formation of a vapor phase. From previous simulations at this temperature, the amount of vapor in water and *n*-nonane binary mixtures is negligible (Michael and Benjamin, 1995), this being increasingly true for higher molecular weight *n*-alkanes; extrapolations to this temperature of the predicted vapor phase densities in vapor - liquid equilibria for the models employed are around 0.0001, 0.0040, and 0.0025 g/cm$^3$ for water (Alejandre *et al.*, 1995), *n*-pentane, and *n*-decane (Nath *et al.*, 1998) respectively. Therefore the formation of stable liquid-liquid-vapor interfaces is not expected.

Liquid-liquid equilibrium simulations were carried out using the same methodology as vapor-liquid simulations, the only difference being that the volume of the simulation cell should have the correct size needed to produce coexisting bulk phases with densities similar to the available experimental data. In this work our goal is not to predict the coexisting bulk densities, but to simulate a system contained in a certain cell volume, which will produce bulk phases with densities corresponding to the experimental values. We expect such systems to have a more realistic density profile at the interface and so should produce values of the interfacial properties closer to the experimental data. A simulation cell smaller than the correct cell will produce higher densities or maybe the system will mix with the formation of vapor-liquid equilibrium due to the higher pressure, while a simulation cell with greater than the correct cell will provoke a continuous formation and destruction of the interfaces due to the highly repulsive nature of the system components. We can perform such simulations in two ways, either by varying the dimension of one side of the simulation cell or by varying the number of molecules in the system. We choose the second route, where an initial system is equilibrated and the densities in the bulk phases are calculated; molecules are then added or eliminated from the initial system, thus increasing or reducing the bulk densities to values corresponding to experimental data. We note that of the molecules added or removed some of them will go to the interfaces, but most of them will go to the bulk phases. The dimensions of the

initial system should consider that we need a simulation cell length bigger than the cutoff ratio in two sides ($L_X$, $L_Y$) and the third side should contain at least twice $L_X$ or $L_Y$ (two phases) plus the thickness of the interface, which for example can be as big as 3.3 Å for water at 298.15 K (Ocko *et al.*, 1994). The equilibrated initial density profiles for water–*n*-pentane at 298.15 K are shown in Figure 2.3. For this system the bulk phases extended to ~28 Å and the total interfacial thickness is ~ 5 Å. The density profile for water is well defined at the interface, in other words we can see clearly where it starts to change in the aqueous phase (water rich) and where it finishes in the organic phase (*n*-alkane rich). For *n*-pentane we can see where the interface finishes in the aqueous phase, but the beginning is not clear because there are molecules of *n*-alkane adsorbed at the interface, hence the density profile for *n*-pentane cannot be fitted by Equation (2.3). The profiles fitted by Equations (2.4) and (2.5) are shown in Figure 2.3, and they reproduce the interfacial region well. The "10–50" interface thickness was computed using the fitted values of Equations (2.4) and (2.5).

The system water–*n*-pentane was simulated using a different number of *n*-pentane molecules to see the dependence of the bulk densities on the number of molecules present in the organic phase. In Figure 2.4 we can see how the bulk and interfacial densities change when we increase the number of *n*-pentane molecules by 20. As expected most of the molecules go to the bulk phase, but a fraction of them go to the interface, making it thicker and the peaks representing

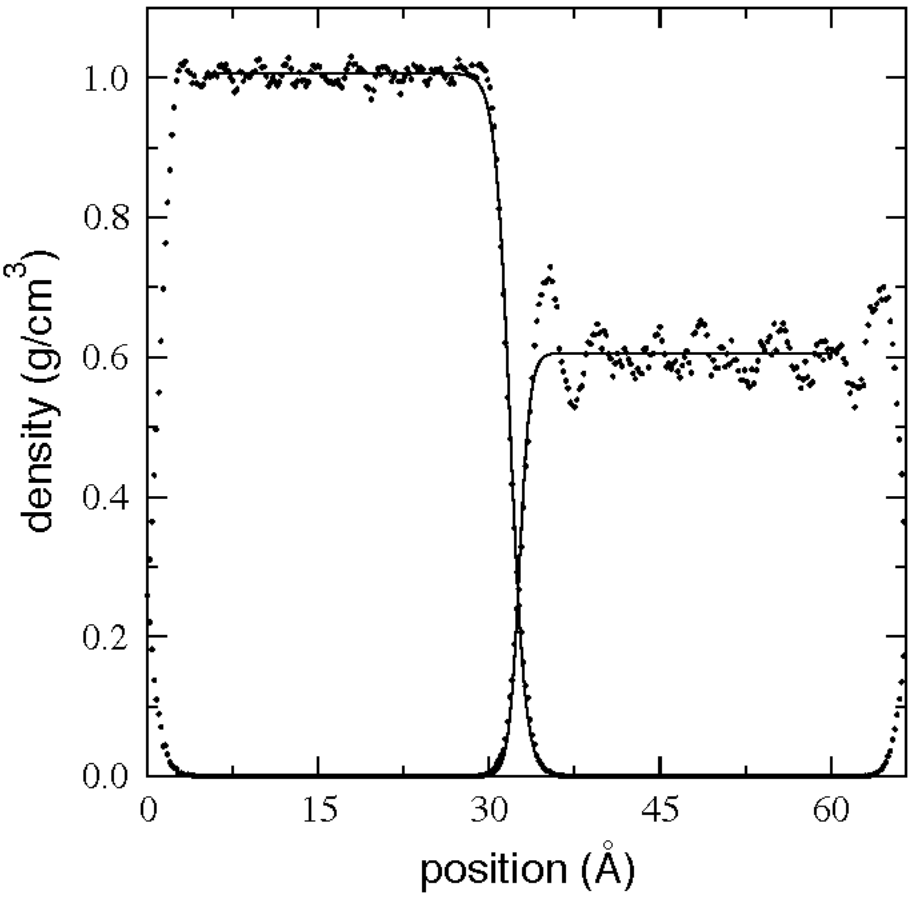


Figure 2.3: Density profiles of the liquid-liquid coexistence system water–*n*-pentane at 298.15 K. Left and right dotted lines are for the simulation results of water and *n*-pentane respectively. Continuous lines represent the fitted profiles to Equations (2.4) and (2.5).

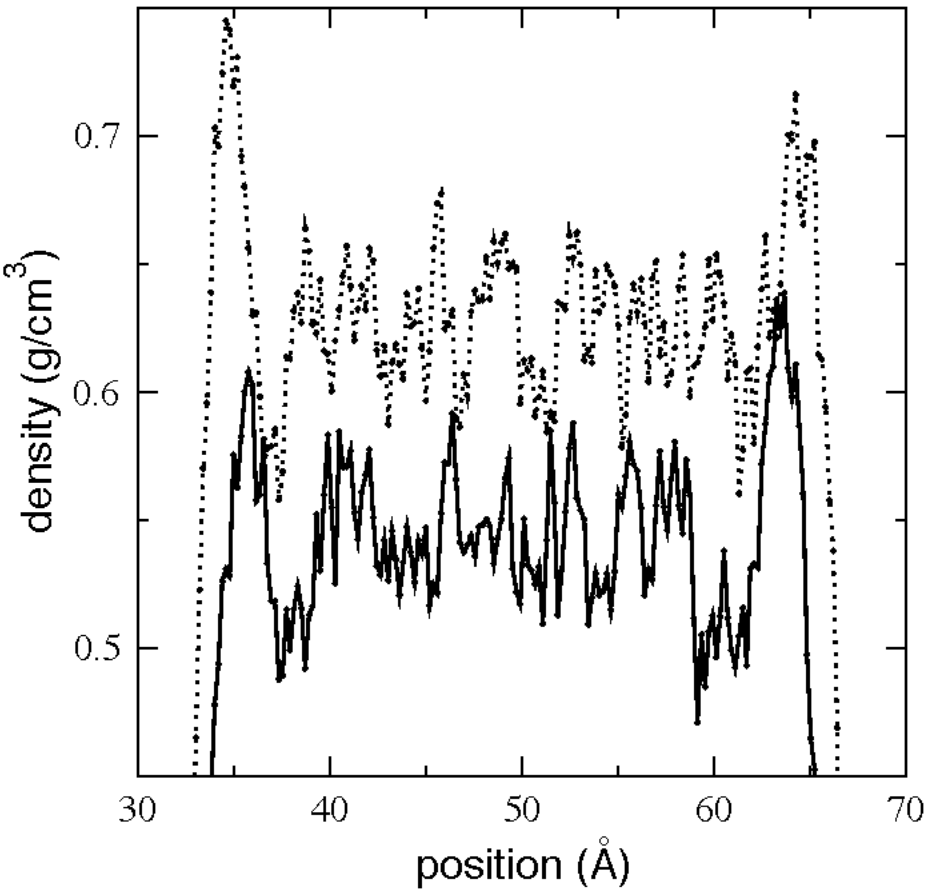


Figure 2.4: Density profiles of *n*-pentane in the system water–*n*-pentane at 298.15 K. Continuous and dotted lines are profiles with 152 and 172 molecules of *n*-pentane respectively.

the molecules adsorbed at the interface higher. The dependence of the bulk densities as a function of the number of *n*-pentanes in the system are shown in Figure 2.5, with horizontal lines representing the experimental density of the pure components. The bulk density of water remains almost constant and for *n*-pentane it increases almost linearly with the number of *n*-pentane molecules. Using around 175 molecules of *n*-pentane we obtained a value for the density in the organic phase, which agrees with the experimental data. The net effect of this process of preparing the systems is that at a specified temperature and density of the bulk *n*-alkane rich phase, we obtain the corresponding density of the bulk water phase and interfacial region.

Following the method described above, we simulated systems from water–*n*-pentane through water–*n*-decane. The results of these simulations for interfacial tension and thicknesses are reported in Table 2.2. The results of this work for the calculation of interfacial tensions as a function of the number of carbons in the *n*-alkane chain studied are shown in Figure 2.6. Experimental data for water–*n*-pentane from Matsubara *et al.* (1988), and for the remaining systems from Mitrinovic *et al.* (2000) are also shown. The simulation data follows the same general trend as the experimental data; the interfacial tension increases slightly with increasing the chain length in the *n*-alkane.

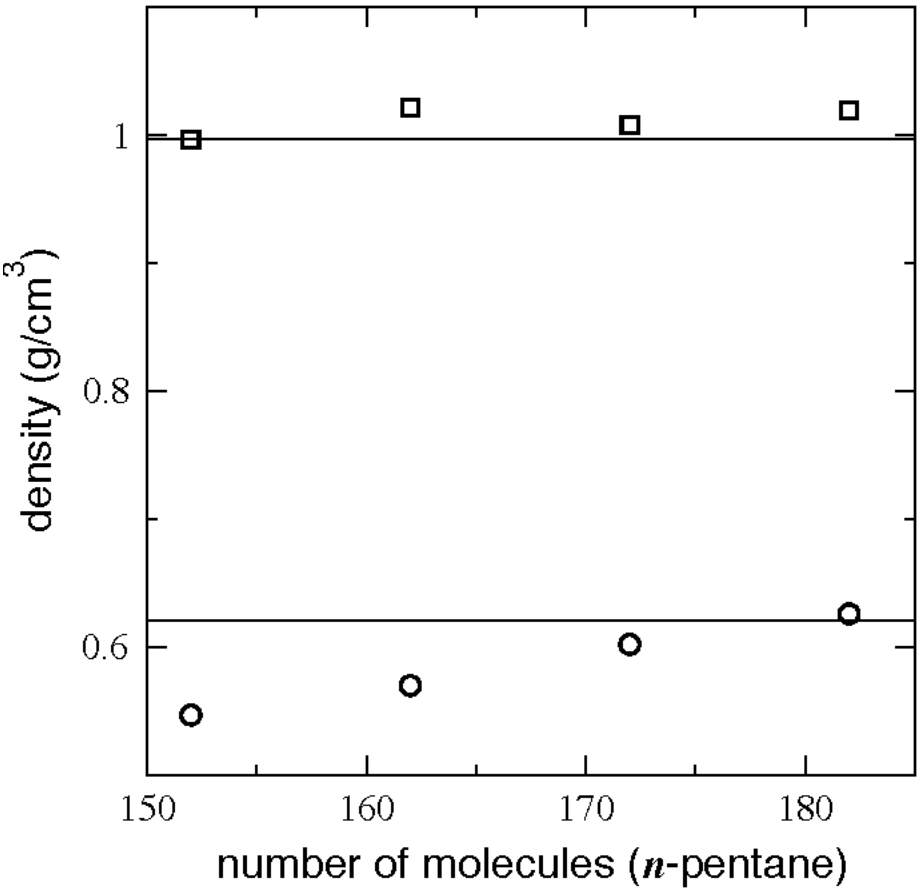


Figure 2.5: Density of each liquid phase in the system water–*n*-pentane at 298.15 K as function of the number of *n*-pentane molecules. Circles and squares represent results from this work for the density of *n*-pentane and water rich phases respectively. Horizontal lines represent experimental data of pure components (Smith and Srivastava, 1986).

Table 2.2: Simulation results for water–*n*-alkane. “10-50” intrinsic interface thickness $t_0$. Interface thickness due to thermal fluctuations $t_C$. Interfacial tension obtained during simulation $\gamma$. Numbers between parentheses indicate the precision of the total values.

| System | $t_0$ (Å) | $t_C$ (Å) | $\gamma$ (mN/m) |
|---|---|---|---|
| Water–*n*-pentane | 0.82 | 1.06 | 50.84 (3.16) |
| water–*n*-hexane | 0.87 | 1.28 | 50.91 (2.52) |
| water–*n*-heptane | 0.91 | 1.44 | 51.02 (2.71) |
| water–*n*-octane | 0.95 | 1.47 | 52.10 (2.30) |
| water–*n*-nonane | 1.16 | 1.48 | 53.22 (2.39) |
| water–*n*-decane | 1.32 | 1.49 | 54.04 (2.42) |

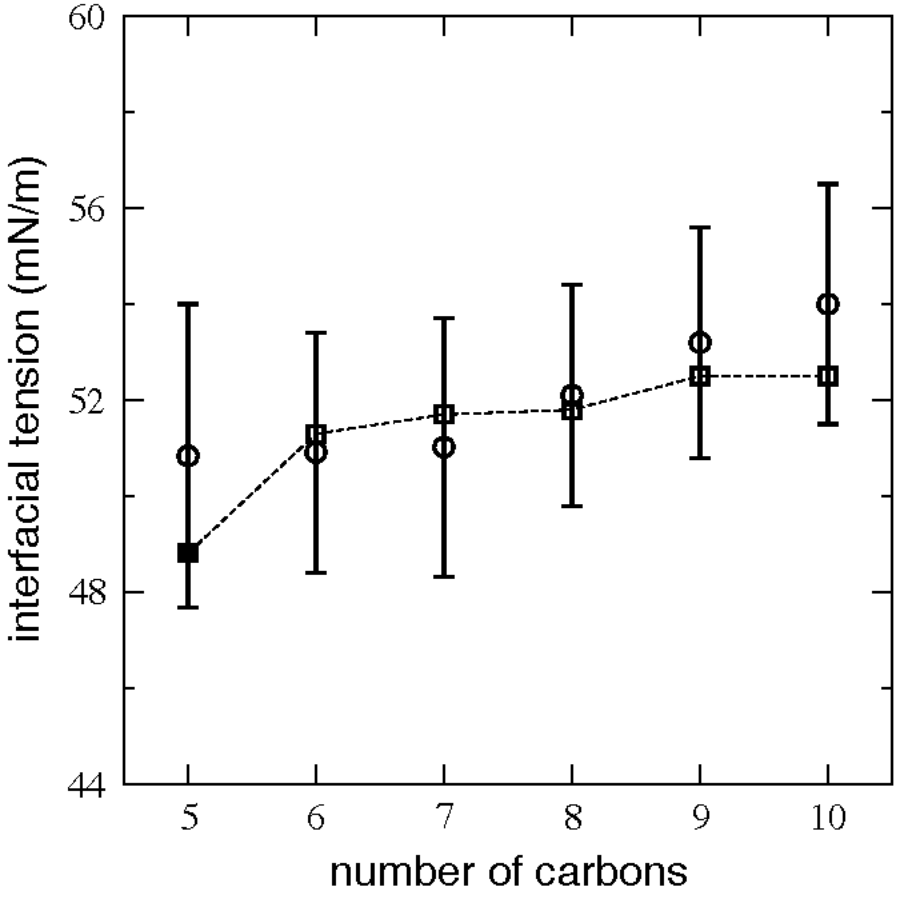


Figure 2.6: Interfacial tension of the liquid-liquid water–*n*-alkane systems as function of the number of carbons in the *n*-alkane molecule at 298.15 K. Filled and open squares represent experimental data from Matsubara *et al.* (1988) and Mitrinovic *et al.* (2000) respectively. Dashed line is only an eye guide. Circles represent results of this work.

In Figure 2.7 we present results of this work for the "10-50" intrinsic and total interfacial thickness ($= \sqrt{t_0^2 + t_C^2}$) as a function of the number of carbons in the water-*n*-alkane systems. As in the capillary-wave theory of Mitrinovic *et al.* (2000), the value for the $t_C$ employed was that obtained from the *n*-alkane density profiles. We compare our results with experimental data for water–*n*-hexane through water–*n*-decane from Mitrinovic *et al.* (1999, 2000) and with the predictions of the capillary-wave theory (Mitrinovic *et al.*, 2000). From the Figure, we can see that the results of this work underpredict the experimental values, but exhibit similar trends to the predictions of the capillary-wave theory (Mitrinovic *et al.*, 2000); the interfacial thickness grows monotonically with the size of the n-alkane chain. Our results have a constant negative deviation of ~2.5 Å from the theoretical predictions and the slope is similar to the experimental results.

Experimental data (Mitrinovic *et al.*, 2000) and theoretical predictions agree well for the systems with *n*-heptane, *n*-nonane, and *n*-decane. Figure 2.8 shows the average ratio profiles of oxygen/hydrogen atoms and $CH_3/CH_2$ groups along the simulation cell for the system water–*n*-pentane and Figure 2.9 for the water–*n*-decane system. These profiles are consecutive averages over 10 ps, with a time between samples of 20 ps. The agreement between theoretical results and experiments (Mitrinovic *et al.*, 2000) has been proposed as a result of highly ordered surfaces at the interface with *n*-alkane molecules having perpendicular

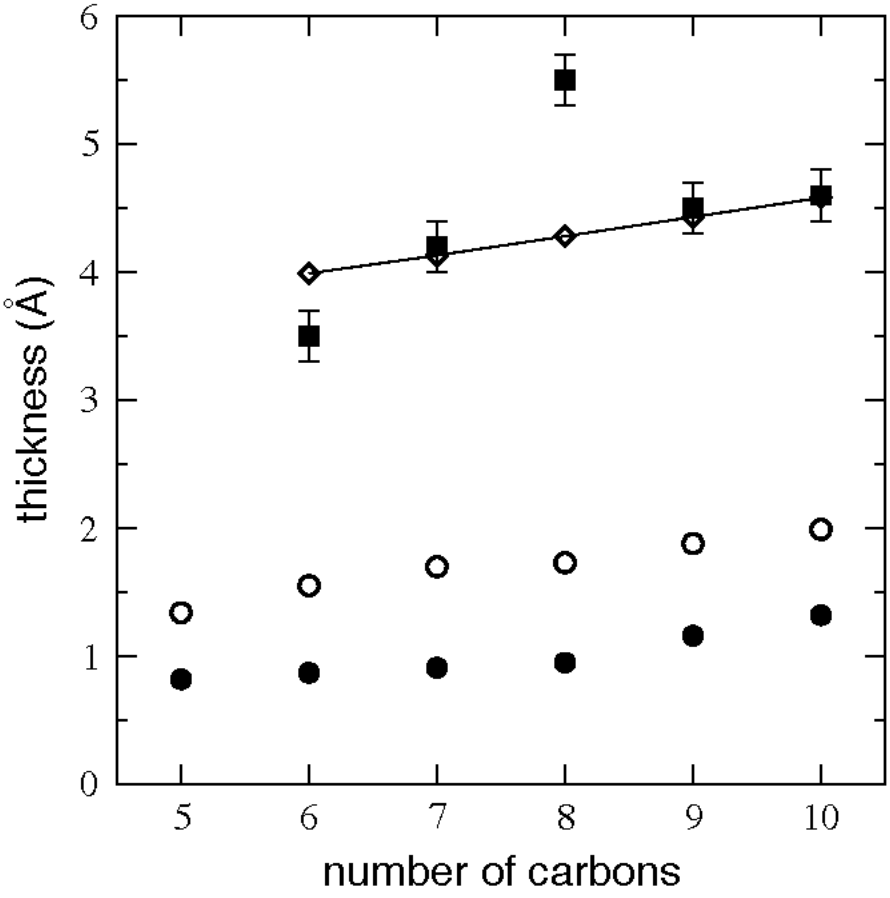


Figure 2.7: Interfacial thickness of the liquid-liquid water–*n*-alkane systems as function of the number of carbons in the *n*-alkane molecule at 298.15 K. Squares and diamonds represent experimental data and theoretical predictions from Mitrinovic *et al.* (2000) respectively. Filled and open circles represent results of this work for the intrinsic and total interfacial thicknesses respectively, based on the “10-50” criterion.

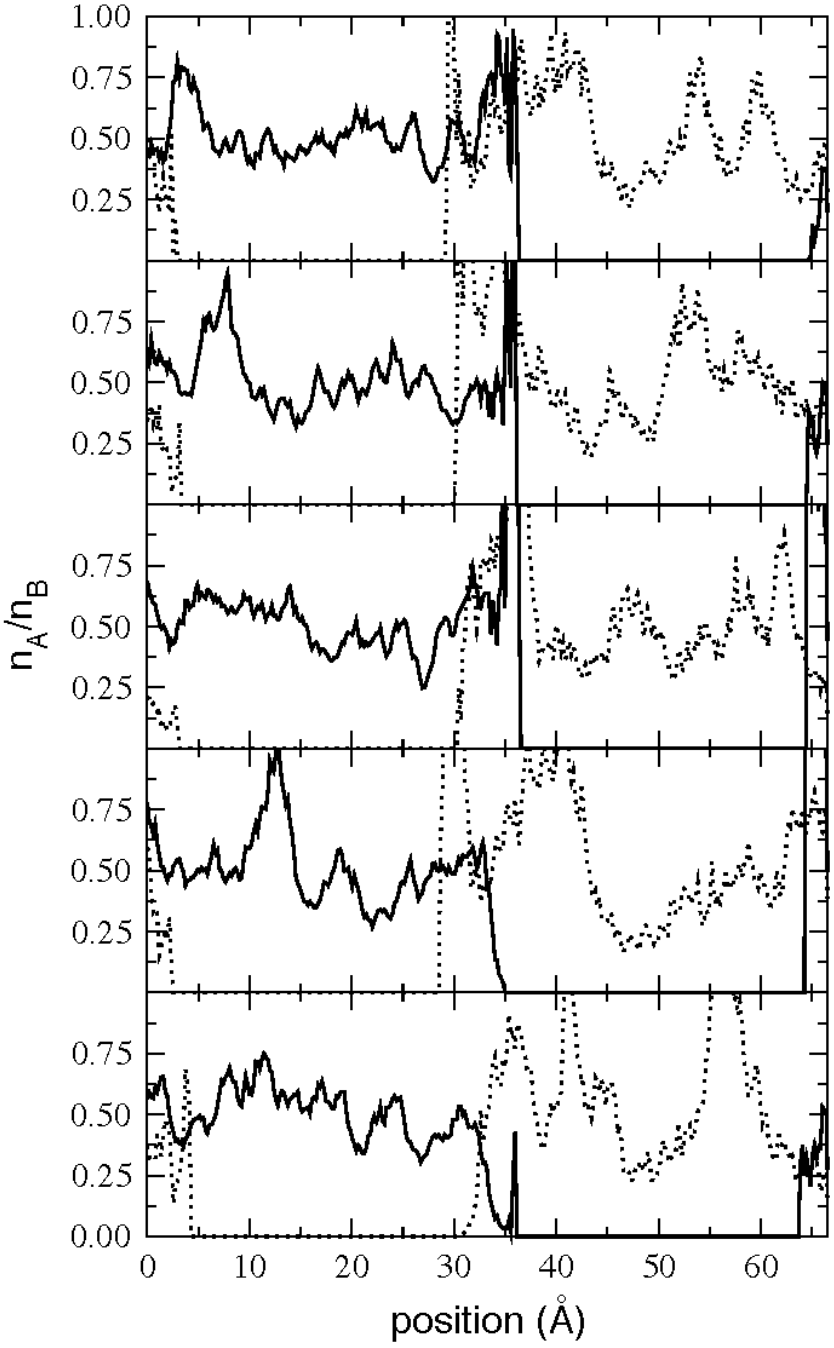


Figure 2.8: Hydrogen/oxygen (solid line) and $CH_3/CH_2$ (dotted line) ratio profiles at different stages of the simulation for the system water–*n*-pentane at 298.15 K. a) 110 ps, b) 140 ps, c) 170 ps, d) 200 ps, and e) 230 ps.

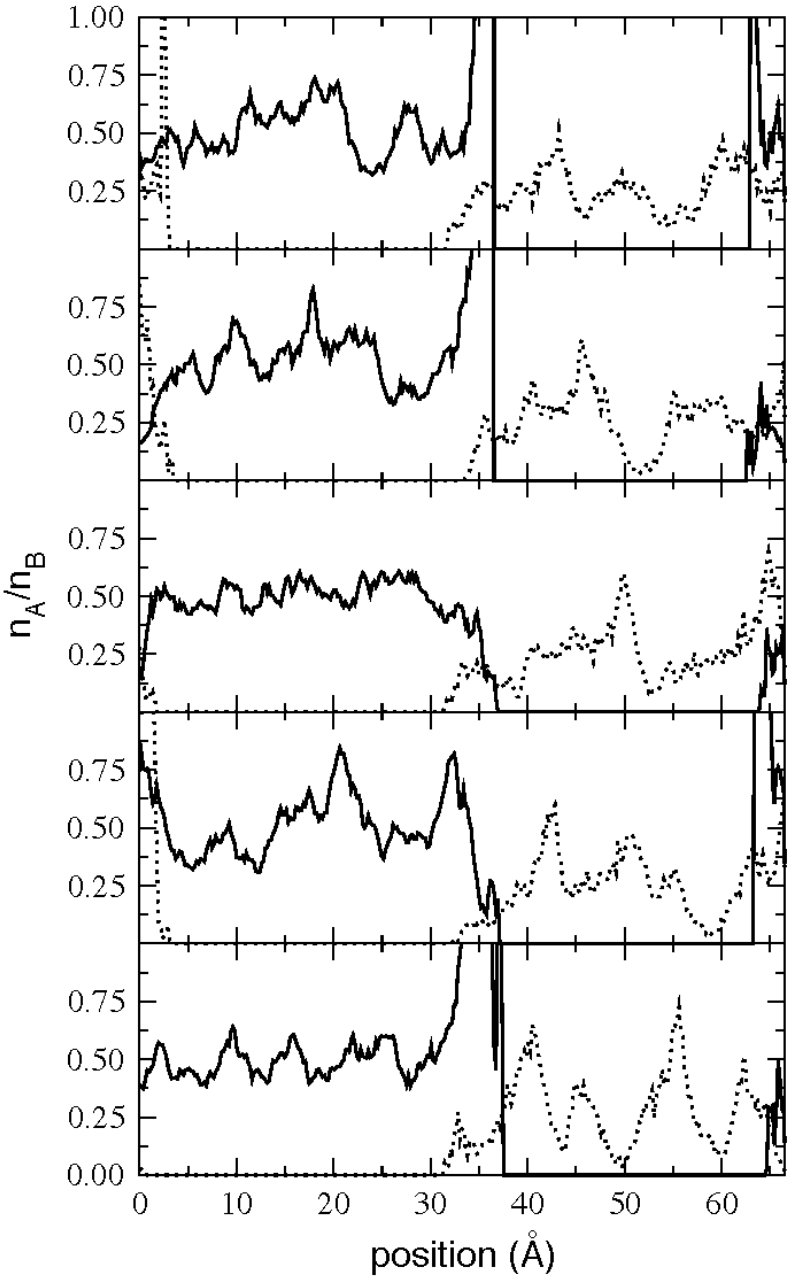


Figure 2.9: Hydrogen/oxygen (solid line) and $CH_3/CH_2$ (dotted line) ratio profiles at different stages of the simulation for the system water–*n*-decane at 298.15 K. a) 110 ps, b) 140 ps, c) 170 ps, d) 200 ps, and e) 230 ps.

orientation to the interface (Conboy et al., 1994). As seen in Figure 2.3, the small peaks in the *n*-alkane density profile show that *n*-alkane molecules are adsorbed at the interface. However, from Figures 2.8 and 2.9 we do not observe stable layer configurations of *n*-alkane molecules perpendicular to the interface. From the snapshots in Figure 2.10, where only *n*-alkane molecules are drawn in views of the *x*-*y* plane of a slab (depth $\Delta z$ = 5 Å) close to the interface for four configurations separated 100 ps in time, we see a preferred parallel orientation of *n*-alkane molecules close to the interface. This preferred parallel orientation of *n*-alkane molecules at the interface is consistent with the peaks observed in the density profiles, since a parallel orientation will produce better packing of the molecules and yield higher densities for the points close to the interface.

### 2.3.3. Liquid-liquid equilibrium for the system water–methanol–*n*-pentane

This liquid-liquid system was simulated (NVT-MD) using the equilibrated water–*n*-pentane system as the initial configuration. Water molecules were exchanged for methanol molecules to simulate systems with different compositions in the aqueous phase. Density profiles for compositions of 0.059 and 0.681 in the mole fraction of methanol are shown in Figures 2.11 and 2.12 respectively. For low concentrations of methanol, the methanol molecules show a preference to be located at the interface, having peaks of density at the interface.

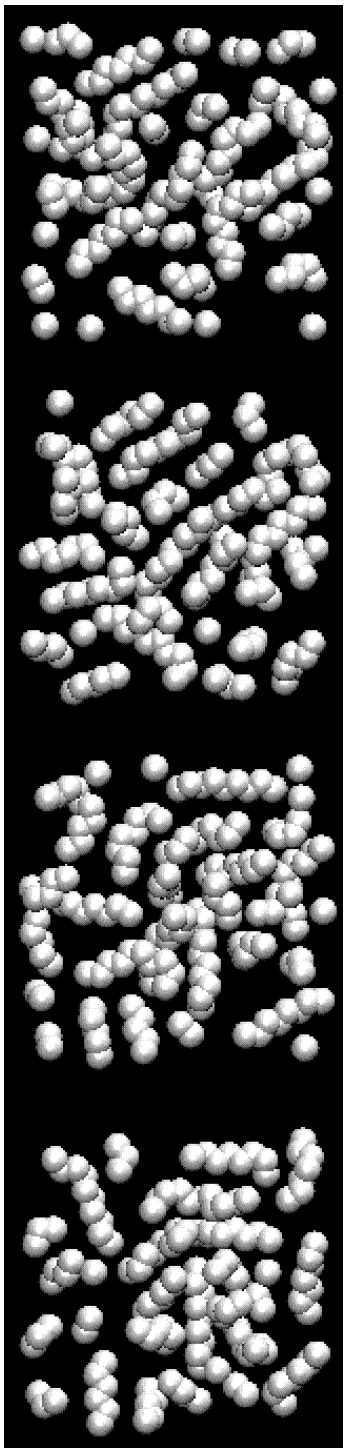

Figure 2.10: Snapshots of *n*-alkane molecules in the x-y plane at the interface (depth $\Delta z$ = 5 Å) in the system water– *n*-decane at 298.15 K and a) 300, b) 400, c) 500, and d) 600 ps.

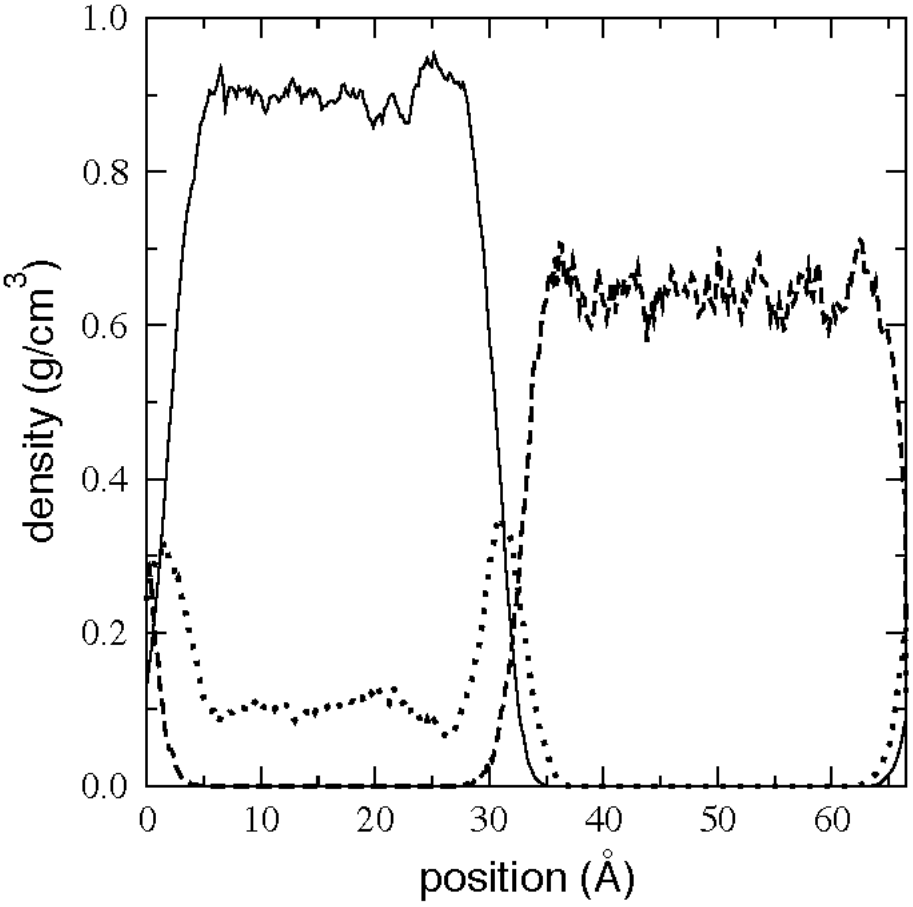


Figure 2.11: Density profiles of the liquid-liquid coexistence system water–methanol–*n*-pentane at low concentrations of methanol and 298.15 K. Continuous line is for water, dotted for methanol, and dashed for *n*-pentane.

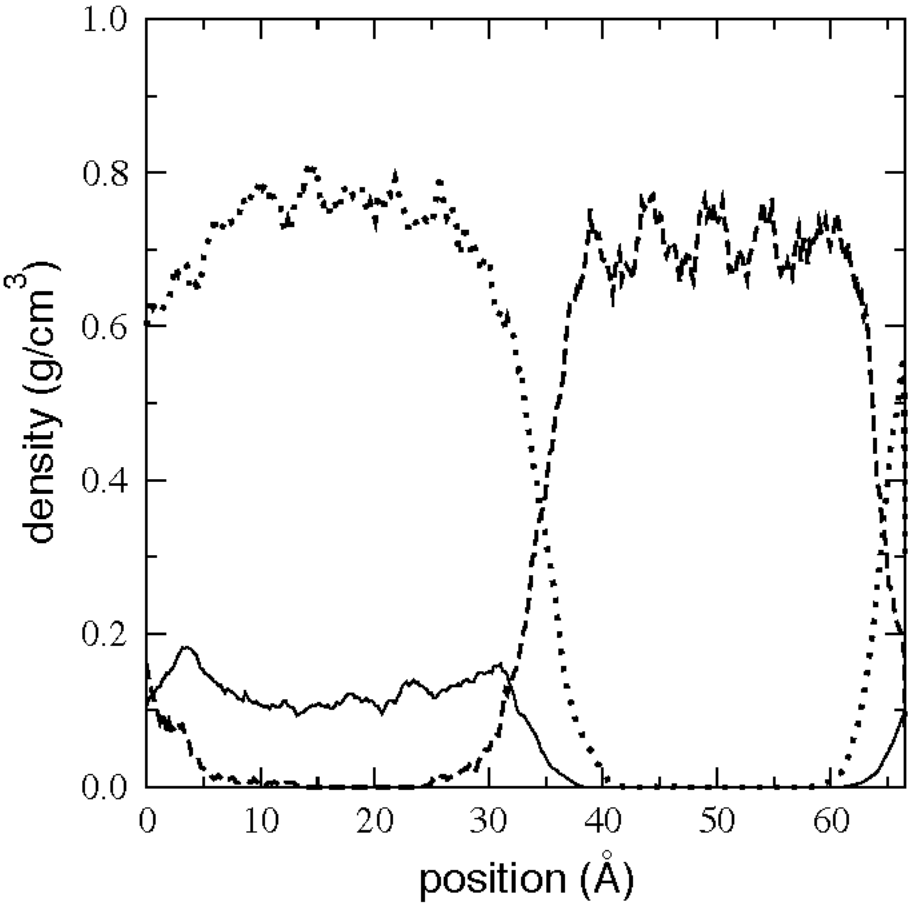


Figure 2.12: Density profiles of the liquid-liquid coexistence system water–methanol–*n*-pentane at high concentrations of methanol and 298.15 K. Continuous line is for water, dotted for methanol, and dashed for *n*-pentane.

The highest peak (0.4 g/cm$^3$) was observed for the system with a mole fraction of 0.179. For high concentrations of methanol, the water molecules prefer to be located away from the interface, inside the methanol rich phase, and an incipient concentration of *n*-alkane molecules is observed in the aqueous phase. A snapshot of the system at low concentration of methanol is shown in Figure 2.13 (note only methanol molecules are drawn at full size). As shown in the density profiles, methanol molecules prefer to be located at the interface or inside the aqueous phase (bottom) and no methanol molecules appear in the organic phase (top). When methanol is added to the original water–*n*-pentane system, there is no adsorption of *n*-pentane molecules at the interface for any concentration of methanol. Results of these simulations for interfacial tension as a function of the mole fraction of methanol in the aqueous phase are reported in Table 2.3.

The interfacial tension as a function of the mole fraction of methanol in the aqueous phase is shown in Figure 2.14, with experimental data from Hampton *et al.* (2001). Our simulation results agree quantitatively well with the experimental data available, showing that when methanol is added to the system the interfacial tension decreases. This is because methanol molecules behave like very small surfactants; the hydroxyl groups (OH) in the methanol molecule prefer to be located close to the aqueous phase, and methyl groups ($CH_3$) close to the

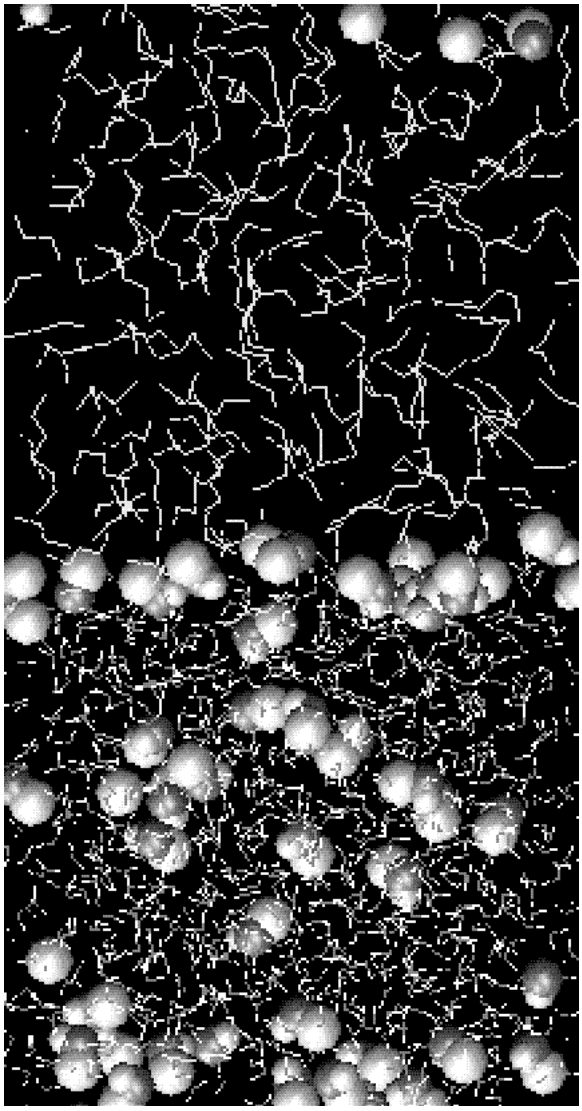

Figure 2.13: Snapshot of the system water–methanol–*n*-pentane at 298.15 K with a methanol mole fraction of 0.024 in the aqueous phase (bottom). Only methanol atoms were drawn with their actual size in order to have a clear picture of the system.

Table 2.3: Simulation results for water–methanol–*n*-pentane. Mole fraction of methanol in the aqueous phase $x_{met}$. Interfacial tension obtained during simulation $\gamma$. Numbers between parentheses indicate the precision of the total values.

| $x_{met}$ | $\gamma$ (mN/m) |
|---|---|
| 0.024 | 41.27 (2.64) |
| 0.059 | 35.96 (3.27) |
| 0.095 | 29.88 (3.06) |
| 0.179 | 24.03 (2.85) |
| 0.384 | 15.41 (3.16) |
| 0.522 | 10.11 (3.01) |
| 0.681 | 7.96 (2.69) |

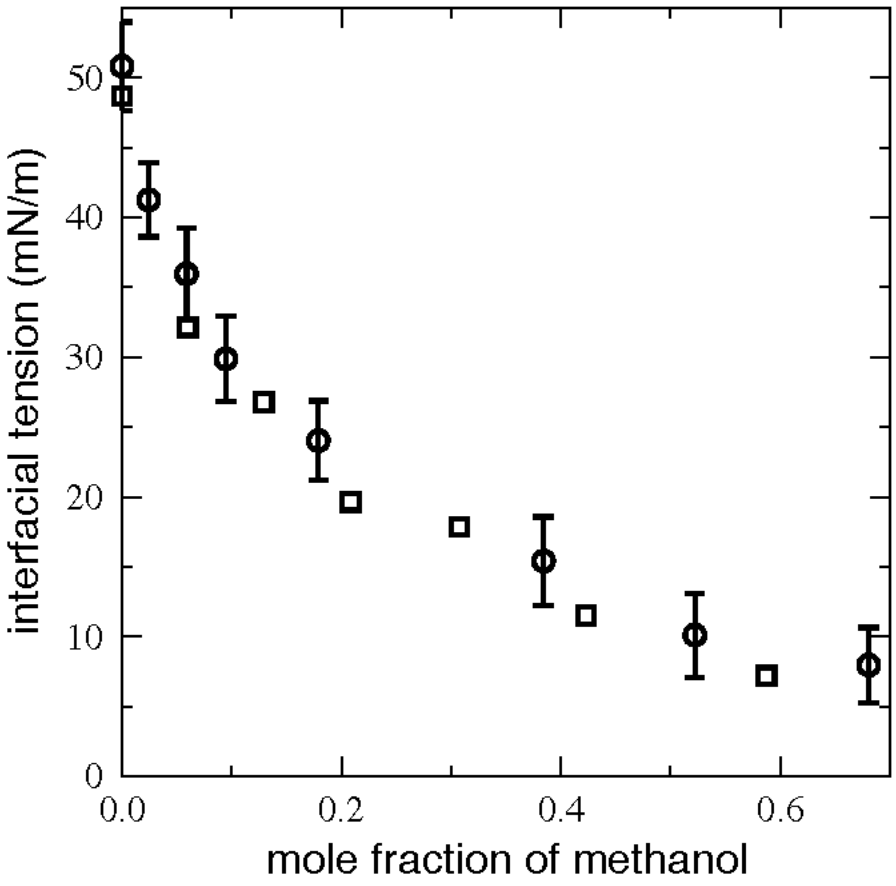


Figure 2.14: Interfacial tension of the liquid-liquid system water–methanol–*n*-pentane as function of the mole fraction of methanol in the aqueous phase at 298.15 K. Squares represent experimental data from Hampton *et al.* (2001). Circles represent results of this work.

organic phase. The overall effect is a reordering of the molecules with the inclusion of methanol molecules at the interface and a decrease in the interfacial tension of the system. The binary system methanol–*n*-pentane does not show liquid-liquid coexistence at this temperature, it only shows vapor-liquid coexistence. This is confirmed by Kiser *et al.* (1961) who reported the highest temperature where liquid-liquid coexistence is observed for methanol–*n*-pentane is 283.15 K, Orge *et al.* (1997) using a group contribution method calculated the vapor-liquid equilibria at 298.15 K, and Carrillo *et al.* (1996) also confirmed this showing that for methanol–*n*-alkane systems at 298.15 K liquid-liquid coexistence occurs only when the *n*-alkane employed has between 6 and 12 carbon atoms. Increasing the concentration of methanol beyond the highest mole fraction reported will allow more *n*-alkane molecules to diffuse to the aqueous phase and when the concentration of methanol is high enough the liquid-liquid system will mix becoming a vapor-liquid system. Studying model Lennard-Jones ternary liquid-liquid systems, Diaz-Herrera *et al.* (1999) and Smit (1988) found the same behavior when one of the species behaves like surfactant.

# Conclusions

The NERD potential for *n*-alkanes was validated for the prediction of interfacial properties in the vapor-liquid interface using *n*-pentane as an example. The

coexisting densities produced by these simulations agree well with the available experimental data and are consistent with previous simulations results for the same model and other models of *n*-alkanes. Unfortunately there is no experimental or theoretical data to compare the predicted interfacial thickness for *n*-pentane, though we note that the results are similar to and show the same behavior as previous simulation results of longer *n*-alkanes. The surface tension values predicted by this potential agree quantitatively well with experimental data in the range of temperatures studied.

Results of this work show that, adjusting the number of molecules to reproduce the liquid densities in the direct simulation method of the liquid-liquid coexistence, the potential models can predict quantitatively satisfactory values for the interfacial tension of the water–*n*-alkane systems. Simulation results agree well with experimental data for water–*n*-pentane through water–*n*-decane systems, though the error bar on the predicted results make the trend of the interfacial tension with chain length unclear. Compared to x-ray reflectivity studies, the results of these simulations underpredict the interfacial thickness as have previous simulation results for pure water. This underprediction of the interfacial thickness is at least in part due to suppression of thermal capillary waves and therefore due to the size of the system employed in this work [33]. Systems with larger interfacial area will produce more exact results for the chosen force fields and we will be performing larger-scale simulations in future work. Previous

predictions of the capillary-wave theory agree with experimental interfacial thickness results for some but not all systems and a trend for identifying which systems the theory should agree with experimental data is not clear. There appears to be no formation of stable ordered interfaces, but a preferred parallel orientation of *n*-alkane molecules close to the interface can be observed from snapshots of the system at all times of the simulation. Experimental results for interfacial thickness of water in the vapor-liquid region have an absolute difference ~ 1.1 Å at 298.15 K and our results for the liquid-liquid water–*n*-alkane have an average difference ~ 2.5 Å with experimental data and theoretical predictions. We believe that we have reported consistent experimental and simulation measures of the interfacial thickness – i.e., we have compared liquid-vapor interfacial thicknesses based on the "10-90" criterion used in the corresponding experiments and the liquid-liquid interfacial thicknesses have been calculated based on the "10-50" criterion, which we believe has been used in the corresponding experiments. However, differences between criteria used in the experiment and the simulation could contribute to the differences reported here.

By interchanging molecules of water with methanol, we can perform simulations with mole fractions in a wide range of compositions in the aqueous phase of the water–methanol–*n*-pentane system. Methanol is the smallest surfactant for this kind of system; when it is added to the water–*n*-pentane binary mixture it is adsorbed mainly at the interface, decreasing the interfacial tension through a

rearrangement of the molecules at the interface. Adsorbed molecules of *n*-alkane at the interface are no longer observed when methanol molecules are present in the system and profiles of these *n*-alkanes are now smooth and continuous without any peak at the interface. Experimental results for the interfacial tension of this system for concentrations of methanol up to mole fractions of 0.6 in the aqueous phase are available and they agree well with results of this work.

# Bibliography


Alejandre J., Tildesley D. J., and Chapela G. A., Fluid-phase equilibria using molecular dynamics: The surface tension of chlorine and hexane, *Mol. Phys.*, **85**, 651 (1995).

Alejandre J., Tildesley D. J., and Chapela G. A., Molecular dynamics simulations of the orthobaric densities and surface tension of water, *J. Chem. Phys.*, **102**, 4574 (1995).

Alejandre J., Rivera J. L., Mora M. A., and de la Garza V., Force field of monoethanolamine, *J. Phys. Chem. B*, **104**, 1332 (2000).

Arai K, Kusu F., and Takamura K., in *Liquid-liquid interfaces: Theory and Methods*; (CRC Press, Boca Raton, FL, 1996), p. 375.

Berendsen H. J. C., Grigera J. R., and Straatsma T. P., The missing term in effective pair potentials, *J. Phys. Chem.*, **91**, 6269 (1987).

Braslau A., Pershan P. S., Swislow G., Ocko B. M., and Nielsen J. A., Capillary waves on the surface of simple liquids measured by x-ray reflectivity, *Phys. Rev. A*, **38**, 2457 (1988).

Buff F. P., Lovett R. A., and Stillinger F. H., Interfacial density profile for fluids in the critical region, *Phys. Rev. Lett.*, **15**, 621 (1965).

Carpenter I. L., and Hehre W. J., A molecular dynamics study of the hexane/water interface, *J. Phys. Chem.*, **94**, 531 (1990).

Carrillo E., Talanquer V., and Costas M., Wetting transition at the liquid-air interface of methanol-alkane mixtures, *J. Phys. Chem.*, **100**, 5888 (1996).

Conboy J. C., Daschbach J. L., and Richmond G. L., Total internal-reflection generation-probing the alkane water interface, *Appl. Phys. A*, **59**, 623 (1994).

Diaz-Herrera E., Alejandre J., Ramirez-Santiago G., and Forstmann F., Interfacial tension behavior of binary and ternary mixtures of partially miscible Lennard-Jones fluids: A molecular dynamics simulation, *J. Chem. Phys.*, **110**, 8084 (1999).

Dickinson E., Euston S. R., and Woskett C. M., Prog. *Colloid Polym. Sci.*, **82**, 65 (1990).

Goebel A., and Lunkenheimer K., Interfacial tension of the water/*n*-alkane system, *Langmuir*, **13**, 369 (1997).

Grigoryev B. A., Nemzer B. V., Kurumov D. S., and Sengers J. V., Surface tension of normal pentane, hexane, heptane and octane, *Int. J. Thermophys.*, **13**, 453 (1992).

Hampton P., Darde T., James R., and Wines T. H., Liquid-liquid separation technology improves IFPEXOL process economics, *Oil & Gas J.*, **99**, 54. (2001).

Jennings H. Y., and Newman G. H., The effect of temperature and pressure on the interfacial tension of water against methane-normal decane mixtures, *Soc. Pet. Eng. J.*, **11**, 171 (1971).

Jorgensen W. L., Quantum and statistical mechanical studies of liquids. 11. Transferable intermolecular potential functions – application to liquid methanol including internal rotation, *J. Am. Chem. Soc.* **103**, 341 (1981).

Kiser R. W., Johnson G. D., and Sheltar M. D., Solubilities of various hydrocarbons in methanol, *J. Chem. Eng. Data*, **6**, 338 (1961).

Kuhn H., and Rehage H., Molecular orientation of monododecyl pentaethylene glycol at water/air and water/oil interfaces. A molecular dynamics computer simulation study, *Colloid Polym. Sci.*, **278**, 114 (2000).

Matsubara H., Murase M., Mori Y. H., and Nagashima A., Measurements of the surface tensions and the interfacial tensions of *n*-pentane-water and R113-water systems, *Int. J. Thermophys.*, **9**, 409 (1988).

Matsumoto M., and Kataoka Y., Study on liquid-vapor interface of water. I. Simulational result of thermodynamic properties and orientational structure, *J. Chem. Phys.*, **88**, 3233 (1988).

Michael D., and Benjamin I., Solute orientational dynamics and surface roughness of water/hydrocarbon interfaces, *J. Phys. Chem.*, **99**, 1530 (1995).

Mitrinovic D. M., Zhang Z., Williams S. M., Huang Z., and Schlossman M. L., X-ray reflectivity study of the water-hexane interface, *J. Phys. Chem. B*, **103**, 1779 (1999).

Mitrinovic D. M., Tikhonov A. M., Li M., Huang Z., and Schlossman M. L., Noncapillary-wave structure at the water-alkane interface, *Phys. Rev. Lett.*, **85**, 582 (2000).

Morrow N. M., in *Interfacial phenomena in petroleum recovery*; (Marcel Dekker Inc., New York, NY, 1991), p. 1.

Nath S. K., Escobedo F. A., and de Pablo J. J., On the simulation of vapor-liquid equilibria for alkanes, *J. Chem. Phys.*, **108**, 9905 (1998).

Ocko B. M., Wu X. Z., Sirota E. B., Sinha S. K., and Deutsch M., X-ray reflectivity study of thermal capillary waves on liquid surfaces, *Phys. Rev. Lett.*, **72**, 242 (1994).

Orge B., Iglesias M., Rodríguez A., Canosa J. M., and Tojo J., Mixing properties of (methanol, ethanol, or 1-propanol) with (*n*-pentane, *n*-hexnae, *n*-heptane and *n*-octane) at 298.15 K, *Fluid Phase Equil.*, **133**, 213 (1997).

Rivera J. L., and Alejandre J., Vapor-liquid equilibrium simulations of nitrogen and *n*-alkane binary mixtures, *Colloid Surf. A*, **207**, 223 (2002).

Rivera J. L., Predota M., Chialvo A. A., and Cummings P. T., Vapor-liquid equilibrium simulations of the SCPDP model of water, *Chem. Phys. Lett.*, **357**, 189 (2002).

Ryckaert J. P., and Bellemans A., *Faraday Discuss. Chem. Soc.*, **66**, 95 (1978).

Sachs W., and Meyn V., Pressure and temperature dependence of the surface tension in the system natural gas / water. Principles of investigation and the first precise experimental data for pure methane/water at 25°C up to 46.8 MPa, *Colloid Surf. A*, **94**, 291 (1995).

Senapti S., and Berkowitz M. L., Computer simulation study of the interface width of the liquid/liquid interface, *Phys. Rev. Lett.*, **87**, 176101 (2001).

Sferrazza M., Xiao C., Jones R. A. L., Bucknall D. G., Webster J., and Penfold J., Evidence for capillary waves at immiscible polymer/polymer interfaces, *Phys. Rev. Lett.*, **78**, 3693 (1997).

Smit B., Molecular-dynamics simulations of amphiphilic molecules at a liquid-liquid interface, *Phys. Rev. A*, **37**, 3431 (1988).

Smith B. D., and Srivastava R., *Thermodynamic Data for Pure Compounds: Part A Hydrocarbons and Ketones*, (Elsevier, Amsterdam, 1986).

Stryer L., *Protein Structure and Function* (W. H. Freeman and Company, New York, 1995).

Taylor R. S., Dang L. X., and Garret B. C., Molecular dynamics simulations of the liquid/vapor interface of SPC/E water, *J. Phys. Chem.*, **100**, 11720 (1996).

Trokhymchuck A., and Alejandre J., Computer simulations of liquid-vapor interface in Lennard-Jones fluids: Some questions and answers, *J. Chem. Phys.*, **111**, 8510 (1999).

van Buuren A. R., Marrink S-J., and Berendsen H. J. C., A molecular dynamics study of the decane/water interface, *J. Phys. Chem.*, **97**, 9206 (1993).

Zhang Y., Feller S. E., Brooks B. R., and Pastor R. W., Computer simulation of liquid/liquid interfaces. I. Theory and application to octane/water, *J. Chem. Phys.*, **103**, 10252 (1995).

Zuo Y-X., and Stenby E. H., Calculation of interfacial tension of hydrocarbon-water systems under reservoir conditions, *In Situ*, **22**, 157 (1998).

# Part 3. Layering behavior and axial phase equilibria of pure water and water / carbon dioxide inside single wall carbon nanotubes

# Summary

We studied the phase equilibrium and layering behavior of the liquid phase in water and water + $CO_2$ systems inside single wall carbon nanotubes. The system containing pure water was examined at temperatures between 274 and 500 K. At low temperatures and close to the wall of the nanotube, the formation of layers enclosing the liquid phase was observed. Upon addition of $CO_2$, gas-liquid equilibrium was observed, resulting in an enhanced layering effect in the liquid phase. The results of this work have been written up as J. L. Rivera, C. McCabe and P. T. Cummings, “"Layering behavior and axial phase equilibria of pure water and water + carbon dioxide inside single carbon nanotubes," and is now in press with *Nano Letters*. It was web-published on October 9, 2002, and can be viewed at *http://pubs3.acs.org/acs/journals/doilookup?in_doi=10.1021/nl0257566.*

# 3.1 Introduction

The recent experimental discovery by Gogotsi *et al.* (2001) that water and gases such as carbon dioxide and methane can be trapped inside carbon nanotubes during the formation of the nanotube has called to attention the phase equilibria (Brovchenko *et al.*, 2001), condensation (Werder *et al.*, 2001) and freezing (Koga *et al.*, 2001) processes of fluids inside carbon nanotubes. Carbon nanotubes can be considered as regular cylindrical graphitic nanopores with the difference that

the walls of the nanotube can be perfect surfaces made of concentric graphene sheets. There are many experimental studies (McDermont and Arnell, 1954; Puri *et al.*, 1961; Barton *et al.*, 1984) on the adsorption of water over graphitic surfaces for different pore sizes, and it has been found that the amount of adsorbed water is proportional to the number of sites that contain chemisorbed oxygen (McDermont and Arnell, 1954) or any another form of oxygen linked to the surface (Puri *et al.*, 1961; Barton *et al.*, 1984). This is also confirmed by first principles calculations (Zhao *et al.*, 2002) where it is shown that water, carbon dioxide, and methane adsorb weakly to the surface of carbon nanotubes, while oxygen and other molecules that behave as charge acceptors have adsorption energies four to five times larger than that of water.

Simulation studies (Brovchenko *et al.*, 2001; Brovchenko and Geiger, 2002; Shevade *et al.*, 2000; Spohr *et al.*, 1998;) of water inside nanopores have focused mainly on the adsorption process using perfect inelastic walls with both attractive and repulsive water – wall interactions. Brovchenko *et al.* (2001) studied the phase equilibria of water inside hydrophobic and hydrophilic pores and found that the coexistence curves are scaled versions of the bulk curve with critical points at ~540 and ~460 K for the hydrophobic and hydrophilic pores respectively. Using molecular dynamics simulations, Spohr *et al.* (1998) studied the adsorption of water inside attractive and repulsive pores and found that in both cases water molecules penetrate and condensate inside the pore.

Furthermore, the condensation is enhanced in the attractive pore with layering effects in the condensed phase, which are especially pronounced at the center of the pore. Shevade *et al.* (2000) studied water-methanol inside activated carbon pores using grand canonical ensemble Monte Carlo simulations and found that the adsorption process is enhanced when the pore surface is modified to have a higher heterogeneity by inclusion of chemically linked carboxylic groups to the surface of the pore. Using Gibbs ensemble Monte Carlo simulations Brovchenko and Geiger (2002) studied the phase equilibria between water inside nanopores and a bulk reservoir for different strengths of the wall – water interaction. They concluded that capillary condensation or evaporation is present depending on the strength of the interaction, and for the case of capillary condensation ordered layering of water molecules close to the wall was also observed.

While it has been experimentally (Dujardin *et al.*, 1994) established that liquids with a surface tension similar to that of water can wet carbon nanotubes surfaces and penetrate inside its internal volume, there are no experimental results that have demonstrated this behavior for water. In the experiment of Gogotsi *et al.* (2001), a ternary mixture containing 85.2 mole % of water, 7.4 % of carbon dioxide, and methane was trapped accidentally when the carbon nanotube was sealed at ~ 1000 K and ~ 100 MPa; the studied nanotube was multiwalled (~250 $\mathring{A}$ thick) and had a inner diameter of ~1500 $\mathring{A}$ and was at least 3500 $\mathring{A}$ in length. The mixture condensate formed drops with inner menisci indicating that the

mixture wets and adsorbs on the inner surface of the nanotube. This behavior is expected for water confined on hydrophilic walls, but is not representative of water confined on clean carbon surfaces, which are generally hydrophobic. The inner walls of this nanotube were not perfect since some parts of the inner layers terminated within the tube. Scanning electron microscopy graphs showed that the condensed phase had low mobility, and therefore molecules close to the wall of the nanotube had a strong interaction with the inner layers of the wall, but since the inner surface of the wall is not perfect, it is not clear if this behavior is due to the inner walls terminating within the tube (see Figure 4 of the work of Gogotsi *et al.*, 2001). Gogotsi *et al.* (2001) observed that consecutive evaporation and condensations of the drops in the experiment were not reversible. They concluded that water was filtering through defects in the wall of the nanotube, so the observed wetting behavior was not representative of the water – nanotube interaction. In this initial study of phase equilibria inside carbon nanotubes we examine how temperature and pressure affect the formation of layers in systems containing pure water and the binary mixture with carbon dioxide.

## 3.2 Methodology

The carbon nanotube was simulated using a fully flexible atomistic model, which consisted of stretching, bending, torsional, and coupled stretching - bending contributions (Guo *et al.*, 1991). The simple point charge extended model of water SPC/E (Berendsen *et al.* 1987), and the Harris-Yung (Harris and Yung, 1995) model for carbon dioxide were used. The SPC/E and the Harris-Yung models contain three electrostatic sites, and the corresponding interactions were truncated spherically based on distances between the centers of mass of the molecules. Lennard - Jones interactions between unlike sites were calculated using Lorentz - Berthelot mixing rules. The interaction between carbon atoms in the nanotube and sites in water and carbon dioxide molecules was purely repulsive, reflecting the hydrophobic nature of the nanotube surface (Gelb *et al.*, 1999; Radhakrishnan *et al.*, 2000). Previous simulation studies (Walther *et al.*, 2001; Werder *et al.*, 2001) of water inside and outside carbon nanotubes used parameters for the Lennard – Jones potential from parameterizations of molecular oxygen – graphite systems (Bojan and Steele, 1987), but as shown by first principle calculations (Zhao *et al.*, 2002), this interaction should be four times stronger than the water – carbon nanotube interaction. From this point of view, the purely repulsive potential is a better approximation for these interactions. A cutoff radius of 13.1Å was employed for all Lennard–Jones interactions, which corresponds to four times the Van der Waals distance between the oxygen and

carbon (nanotube) sites. The size of the simulation cell was chosen to cover the whole nanotube, and periodic boundary conditions were employed in the axial direction to calculate intramolecular interactions between the carbon atoms at the ends of the nanotube; periodic conditions in the remaining radial directions were unnecessary as the molecules of the condensed liquid are contained in the nanotube and those molecules cannot escape from the nanotube. The conformation of the simulated nanotube had a chiral vector of (20, 20), which corresponds to a diameter of 27.12 Å, and an axial length of 100 Å (replicated periodically). The simulations were carried out using the Verlet algorithm at constant temperature and the time step employed was 1.0 fs. For the simulations with pure water, 540 molecules were employed, and for the binary system, an additional 50, 100, 150, 200, and 222 molecules of carbon dioxide were employed to simulate systems with different pressures and compositions. After an equilibration period of 150 ps, the properties were calculated during a period of 450 ps.

## 3.3 Results

For analysis the volume inside the nanotube was divided into axial slabs, and each slab was subdivided into concentric cylindrical sub-slabs. During the data

collection period after equilibration, the number of molecules whose center of mass positions occurred in each sub-slab was stored and at the end of the simulation the probability maps of finding a certain number of molecules for each sub-slab was calculated. In Figure 3.1 we show the probability maps for pure water at temperatures of (from top to bottom) a) 274 K, b) 298.15 K, c) 350 K, d) 400 K, e) 450 K, and f) 500 K in a perpendicular view to the axial direction. The probabilities are drawn in a gray scale, where regions with the highest probability are white and black describes regions where there are no molecules. The number of molecules in each slab was also stored, and the average axial density profile is plotted on the right hand side of Figure 3.1; in calculating the density within a slab, we estimated the volume of each slab by assuming a radius of 13.56 Å – (3.283 Å)/2 = 11.919 Å, where 3.283 Å is the Van der Waals diameter between oxygen sites in water and carbon sites in the nanotube. For temperatures of 274 K and 298.15 K, we observe well defined layers of finite length (forming a curved vapor-liquid interface at each end) containing the condensed phase, which extends for ~60 Å; the molecules inside these layers exhibit regions of high and low probability, yielding characteristic formations probably due to a nucleation of water molecules; the density profiles show homogeneous axial regions in terms of the average density of each slab, and these homogeneous regions extend for ~40 Å. Upon increasing the temperature of the system to 350 and 400 K the condensed phase expanded to a region of

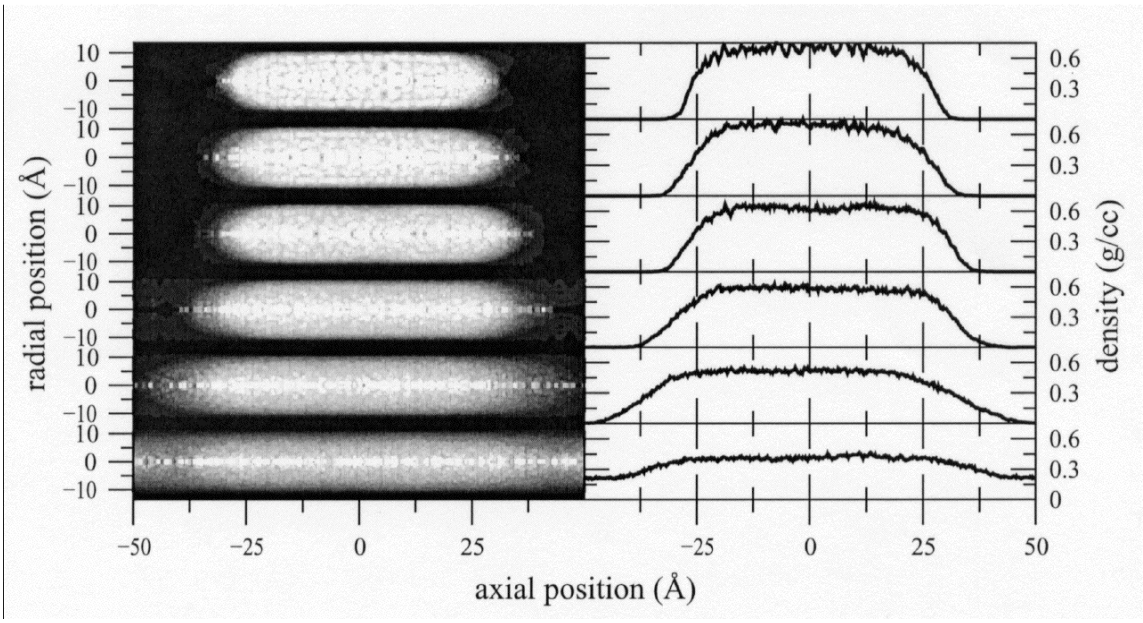


Figure 3.1: Probability maps (left), and density profiles (right) for pure water inside single wall carbon nanotube at a) 274, b) 298.15, c) 350, d) 400, e) 450, and f) 500 K (from top to bottom).

~75 Å and the homogeneous regions to ~50 Å. Although the condensed phase is well defined the layering has largely disappeared and the radial center of the nanotube is seen as the region where the higher probabilities are present; the same behavior was found by Spohr *et al.* (1998) in their theoretical study of water inside slit pores. At higher temperatures *viz.* 450 and 500 K, the water molecules occupy the whole space inside the nanotube. The radial center of the nanotube still shows regions of higher probability, and the homogeneous axial density regions extend for ~60 and ~70 Å at 450 and 500 K respectively. The nucleation of water to form layers at low temperatures is in agreement with x-ray and neutron scattering studies of water at hydrophobic surfaces (Bellissent-Funel *et al.*, 1996); these experiments showed that the properties of water molecules as close as 5 Å to the hydrophobic wall have a distorted hydrogen bond network compared to bulk water.

The average radial probability profiles were calculated for the homogeneous regions where the liquid density does not change in the density profiles of Figure 3.1. These average radial profiles are shown in Figure 3.2 for temperatures of 274 and 450 K in order to show the influence of temperature. In these plots the center of the nanotube is located at zero distance and the carbon atoms are at 13.56 Å. At 274 K, the profile has peaks at 1.29, 5.08 and 7.67 Å; the last peak is well defined and it corresponds to the outer layer observed in the probability map of Figure 3.1a; the two first peaks are not well defined and they correspond to the

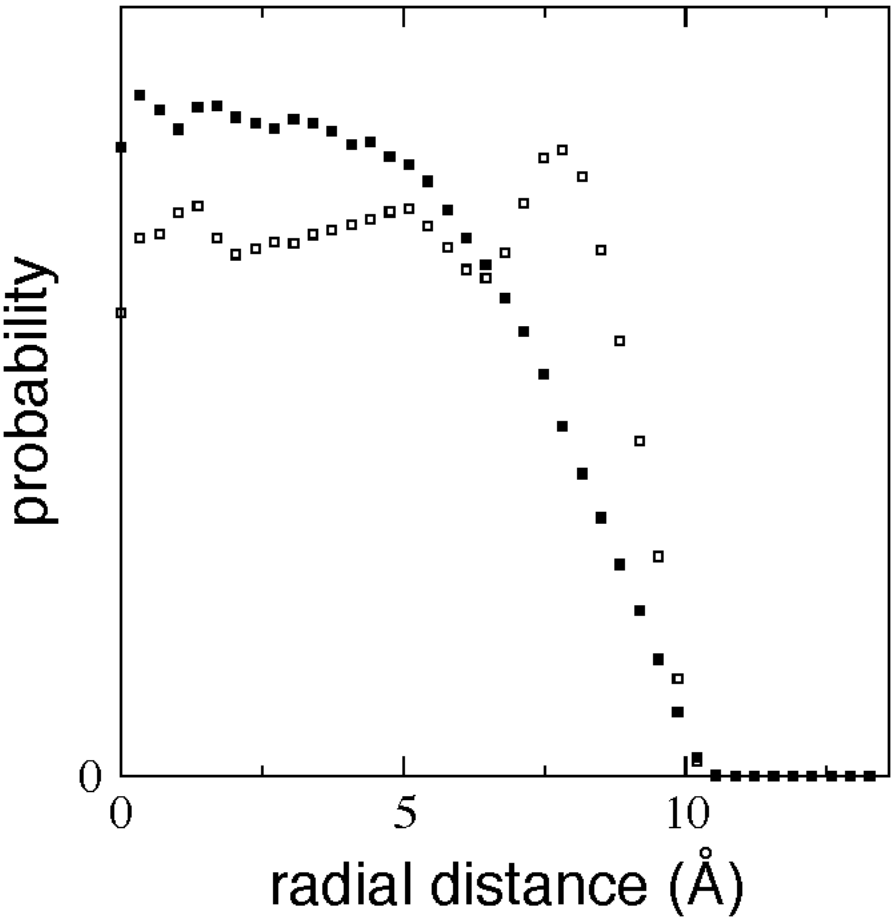


Figure 3.2: Radial probability profiles for pure water inside single wall carbon nanotube at 274 K (open squares), and 450 K (filled squares).

characteristic structures formed inside the outer layer, which we can conclude correspond to two more concentric layers not so well defined as the outer layer. Similar behavior has been observed in previous simulations of confined systems (Spohr *et al.*, 1998; Brovchenko and Geiger, 2002). At higher temperatures, there are still some structures at the center of the nanotube as can be seen from the probability maps, and on average the radial probability profile decays monotonically with the highest probability at the center of the nanotube.

The axial density profiles in Figure 3.1 were fitted using a common expression for bulk vapor-liquid equilibrium (Rivera *et al.*, 2002):

$$\rho(z) = 0.5(\rho_L + \rho_V) - 0.5(\rho_L - \rho_V)\tanh\left[\frac{z - z_0}{d}\right] \tag{3.1}$$

where $\rho_L$ is the density corresponding to the condensed liquid which is homogeneous in terms of the axial direction, $\rho_V$ is the density of the vapor which is zero for temperatures up to 450 K, $z_0$ is the position of the Gibbs' dividing surface related to the interface vapor-liquid equilibrium in the axial direction, and $d$ is a parameter related to the thickness of such an interface. Results of the fitted condensed liquid densities are shown in Figure 3.3 where they are compared with experimental results for bulk vapor-liquid equilibrium (Haar *et al.*, 1984), and simulation results of water inside hydrophobic cylindrical pores with

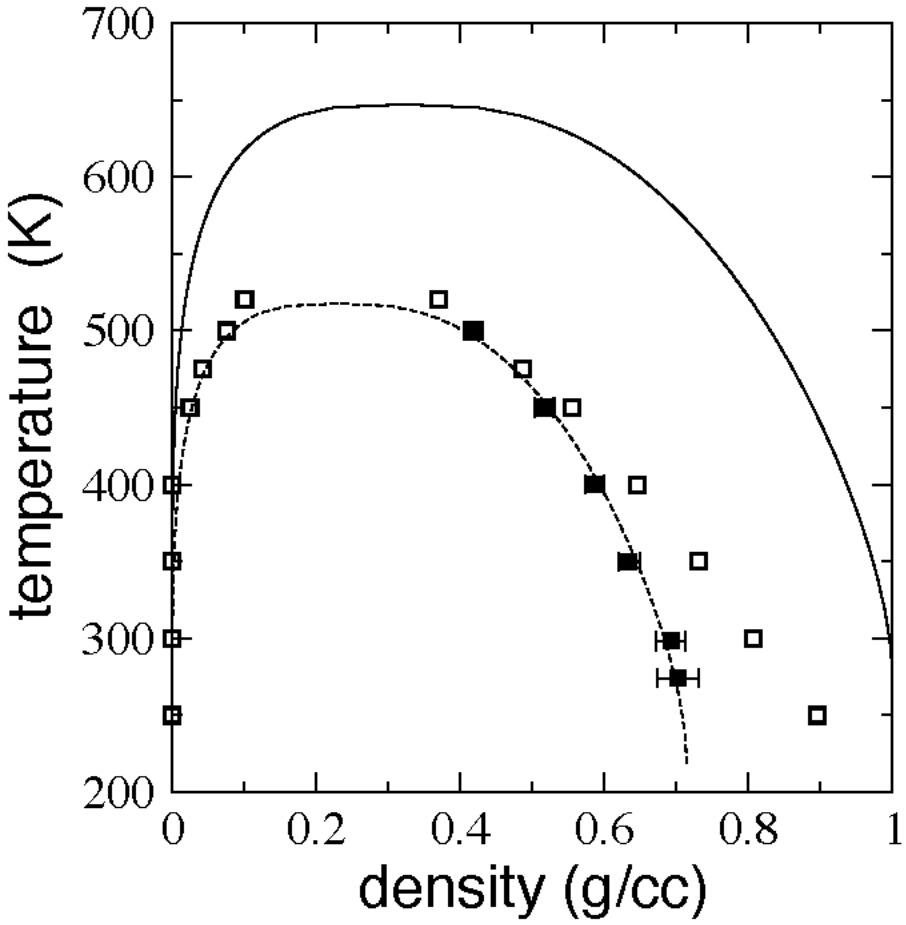


Figure 3.3: Liquid densities of confined water inside single wall carbon nanotube versus temperature (filled squares). The solid line represents experimental data for bulk vapor-liquid equilibrium (Haar *et al.*, 1984), the dashed line the scaled curve from the bulk experimental data, and the open squares the results of Brovchenko *et al.* (2001).

radius of 12 Å. Compared to the bulk, the curve of the confined liquid systems seems to be a scaled version of the bulk curve. Scaling the bulk curve by the optimized factors of 0.7 in density and 0.8 in temperature, we obtained a scaled version of the bulk curve that agrees well with our simulation results for the confined liquid. From the scaled curve we obtained a critical point for the confined system at ~512 K and ~0.23 g/cc, and a freezing point between 298.15 and 350 K. These simulation results are very similar to the results previously obtained for water inside cylindrical hydrophobic pores[2] with a similar radius to that employed in this work where the critical point was ~540 K and ~0.20 g/cc.

The effect of the pressure on the layering effect in condensed phases was studied by the addition of different amounts of carbon dioxide to the pure water system. The probability maps and the axial density profiles for systems with a) 0, b) 50, c) 100, d) 150, and e) 200 molecules of carbon dioxide are shown in Figure 3.4 at 298.15 K, and Figure 3.5 for the profiles at 500 K with an additional composition f) having 220 molecules of carbon dioxide. The inclusion of the first 50 molecules of carbon dioxide produced phase equilibrium in the axial direction with the condensed liquid located at the axial center of the nanotube and formed exclusively by water molecules as appreciated in the density profile of Figure 3.5b. As the number of molecules of carbon dioxide was increased, the internal pressure of the nanotube also increased, contracting the axial length of the liquid phase; for the case with 200 molecules of carbon dioxide at 298.15 K, the

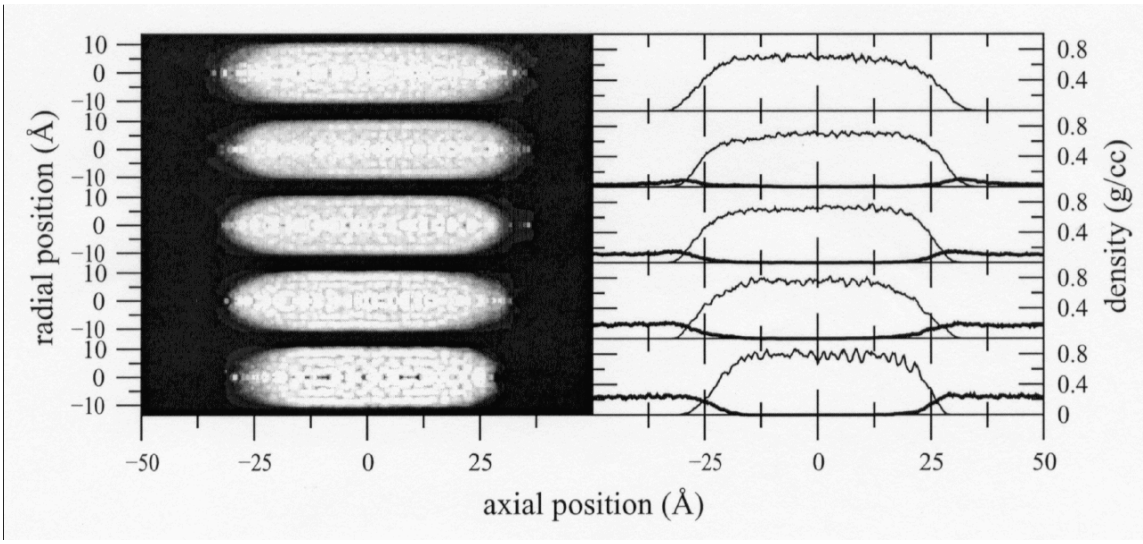


Figure 3.4: Probability maps (left), and density profiles (right) for the binary system water / carbon dioxide inside single wall carbon nanotube at 298.15 K using 540 molecules of water and a) 0, b) 50, c) 100, d) 150, and e) 200 molecules of carbon dioxide (from top to bottom). The continuous lines in the density profiles are for water and the solid lines for carbon dioxide.

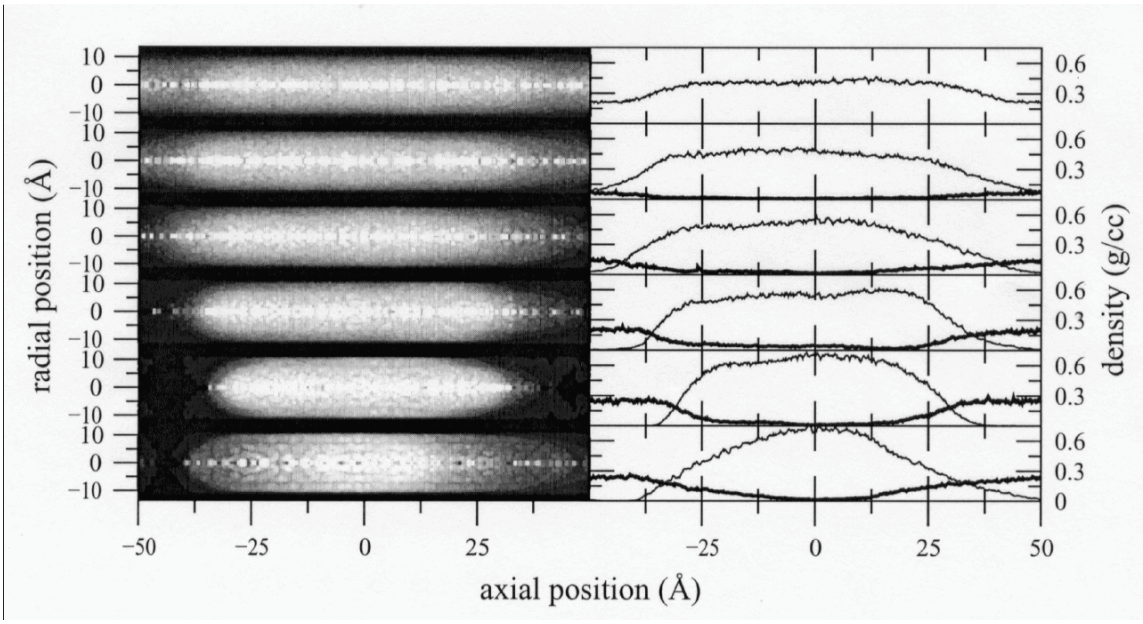


Figure 3.5: Probability maps (left), and density profiles (right) for the binary system water / carbon dioxide inside single wall carbon nanotube at 500 K using 540 molecules of water and a) 0, b) 50, c) 100, d) 150, e) 200, and g) 220 molecules of carbon dioxide (from top to bottom). The continuous lines in the density profiles are for water and the solid lines for carbon dioxide.

condensed liquid phase decreased its axial extension by ~10 Å, while for the same case at 500 K the decrement was ~35 Å. At 298.15 K we can appreciate an increased layering effect as the pressure inside the nanotube increases; for the last two cases e), and f), where the pressure is higher, we can observe six very well defined layers of finite length formed exclusively by the water molecules. This layering effect can also be observed in the radial probability profiles which are shown in Figure 3.6 for cases a) and e) in Figure 3.5 at 298.15 K. At these higher pressures inside the nanotube, the profile peaks are more pronounced, the first two peaks are at 1.84, and 5.38 Å, while at the higher pressure the last peak moved from 7.83 to 8.32 Å. These radial expansions of the molecular layers are due to the contraction in the axial length of the condensed phase due to the higher pressure exerted axially over the liquid phase. At 500 K, there is also a decrease in the axial extension of the condensed phase, but there appears to be a small layering effect on the condensed phase for the system with highest pressure. However, it should be noted that at this condition the liquid-vapor interface is very broad, resulting in a liquid phase of very limited extent; hence, we should exercise caution in drawing conclusions based on this simulation.

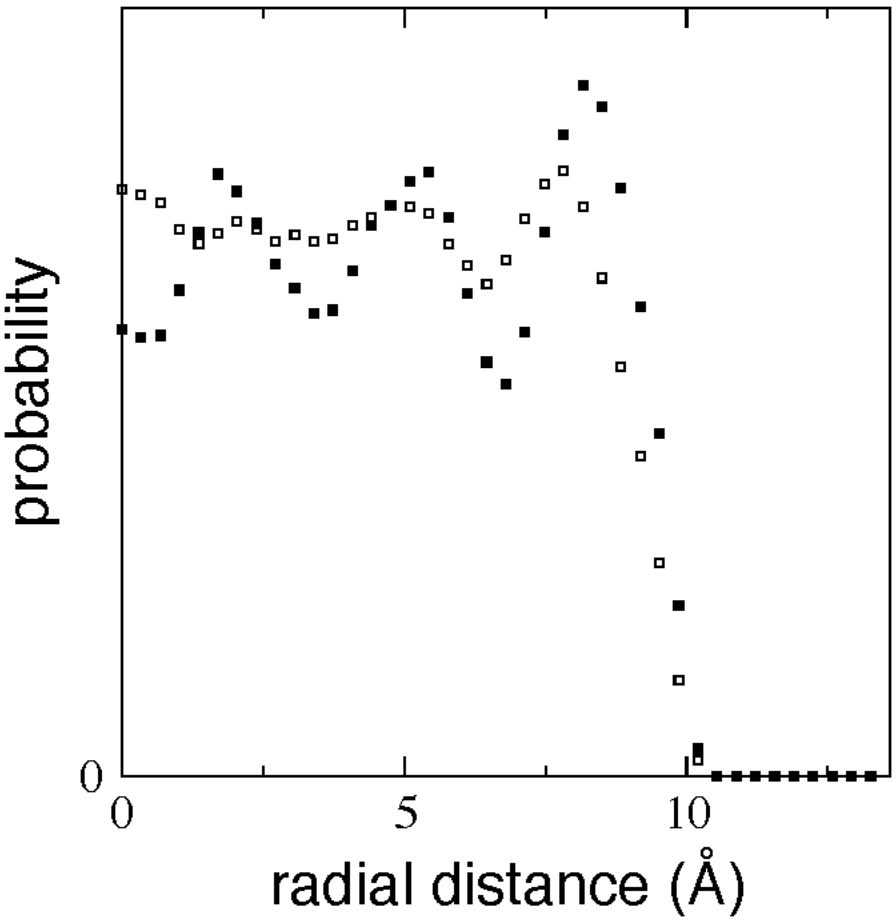


Figure 3.6: Radial probability profiles for the binary system water / carbon dioxide inside single wall carbon nanotube at 298.15 K using a) 540 molecules of pure water (open squares), and b) 540 molecules of water, and 200 molecules of carbon dioxide (filled squares).

# Conclusions

We have performed the first molecular dynamics simulations of condensed phases inside single wall carbon nanotubes. The effect of temperature and pressure on the phase equilibria and layer formation on the liquid phase was studied for both pure water and the binary system with carbon dioxide at temperatures up to 500 K. For the system with pure water, at all temperatures (except the lowest) there is a preference for the water molecules to be located close to the radial center of the nanotube (as evidenced by the maximum of the radial probability profile located at the center of the nanotube). At lower temperatures, the system formed a well-defined layer at the nanotube wall in agreement with x-ray and neutron scattering results of water at hydrophobic surfaces (Bellissent-Funel *et al.*, 1996). Compared to the bulk vapor-liquid coexistence the confined coexistence curve is a scaled version of the bulk, having a critical point at ~512 K and ~0.23 g/cc which is similar to previous simulation results (Brovchenko *et al.*, 2001) of water confined by hydrophobic cylindrical nanopores. The addition of carbon dioxide molecules increased the pressure of the system and decreased the axial extension of the liquid phase, producing better defined layered systems at 298.15 K while at 500 K the layering formations are not well defined probably because of the size of the simulated system.

# Bibliography


Barton S. S., Evans M. J. B., Holland J., and Koresh J. E., Water and cyclohexane water adsorption on oxidized porous carbon, *Carbon*, **22**, 265 (1984).

Bellissent-Funel M.-C., Sridi-Dorbez R., and Bosio L., X-ray and neutron scattering studies of the structure of water at a hydrophobic surface, *J. Chem. Phys.*, **104**, 10023 (1996).

Berendsen H. J. C., Grigera J. R., and Straatsma T. P., The missing term in effective pair potentials, *J. Phys. Chem.*, **91**, 6269 (1987).

Bojan M. J., and Steele W. A., Interactions of diatomic molecules with graphite, *Langmuir*, **3**, 1123 (1987).

Brovchenko I., Geiger A., and Oleinikova A., Phase equilibria of water in cylindrical nanopores, *Phys. Chem. Chem. Phys.*, **3**, 1567 (2001).

Brovchenko I., and Geiger A., Water in nanopores in equilibrium with a bulk reservoir – Gibbs ensemble Monte Carlo simulations, *J. Mol. Liq.*, **96-97**, 195 (2002).

Dujardin E., Ebbese T. W., Hiura H., and Tanigaki K., Capillarity and wetting of carbon nanotubes, *Science*, **265**, 1850 (1994).

Gelb L. D., Gubbins K. E., Radhakrishnan R, and Sliwinska-Bartkowiak M., Phase separation in confined systems, *Rep. Prog. Phys.*, **62**, 1573 (1999).

Gogotsi Y., Libera J. A., Guvenc-Yazicioglu A., and Megaridis C. M., In situ multiphase fluid experiments in hydrothermal carbon nanotubes, *Appl. Phys. Lett.*, **79**, 1021 (2001).

Guo Y., Karasawa N., and Goddard W. A., Prediction of fullerene packing in $C_{60}$ and $C_{70}$ crystals, *Nature*, **351**, 464 (1991).

Haar L., Gallagher J. S., and Kell G. S., *NBS/NRC Steam Tables*, (Hemisphere, Washington D. C., 1984).

Harris J. G., and Yung K. H., Carbon dioxide liquid-vapor coexistence curve and critical properties as predicted by a simple molecular model, *J. Phys. Chem.*, **99**, 12021 (1995).

Koga K., Gao G. T., Tanaka H., and Zeng X. C., Formation of ordered ice nanotubes inside carbon nanotubes, *Nature*, **412**, 802 (2001).

McDermont H. L., and Arnell J. C., *J. Phys. Chem.*, **58**, 492 (1954).

Puri B. R., Murari K., Singh D. D., *J. Phys. Chem.*, **65**, 37 (1961).

Radhakrishnan R., Gubbins K. E., and Sliwinska-Bartkowiak M., Effect of the fluid-wall interaction on freezing of confined fluids: Toward the development of a global phase diagram, *J. Chem. Phys.*, **112**, 11048 (2000).

Rivera J. L., Predota M., Chialvo A. A., and Cummings P. T., Vapor-liquid equilibrium simulations of the SCPDP model of water, *Chem. Phys. Lett.*, **357**, 189 (2002).

Shevade A. V., Jiang S., and Gubbins K. E., Molecular simulation study of water-methanol mixtures in activated carbon pores, *J. Chem. Phys.*, **113**, 6933 (2000).

Spohr E., Trokhymchuk A., and Henderson D., Adsorption of water molecules in slit pores, *J. Electroanal. Chem.*, **450**, 281(1998).

Walther J. H., Jaffe R., Halicioglu T., and Koumoutsakos P., Carbon nanotubes in water: Structural characteristics and energetics, *J. Phys. Chem. B*, **105**, 9980 (2001).

Werder T., Walther J. H., Jaffe R. L., Halicioglu T., Noca F., and Koumoutsakos P., Molecular dynamics simulation of contact angles of water droplets in carbon nanotubes, *Nano Lett.*, **1**, 697 (2001).

Zhao J., Buldum A., Ham J., and Lu, J. P., Gas molecules adsorption in carbon nanotubes and nanotube bundles, *Nanotechnology*, **13**, 195 (2002).

# Part 4. Oscillatory damped behavior of double-wall carbon nanotubes

# Summary

Mechanical properties of carbon nanotubes were studied through molecular dynamics simulations in the canonical ensemble. Double-wall systems with chiral conformations (7,0)/(9,9), (7,0)/(10,10), and (5,5)/(10,10) for the inner/outer nanotubes were simulated for systems with axial lengths from 12.21 to 98.24 nm at temperatures in the range of 275 to 450 K. These systems were prepared to simulate damped oscillations of the separation between their centers of mass. These oscillations showed frequencies in the scale of GHz, and the frequency decreased with the axial length of the system at 298.15 K. The time needed to reduce the amplitude of the oscillations to 4 nm showed almost a linear dependency with the length of the system; at higher temperatures, this time decreased. For systems with not equal lengths, the retraction force is reduced if it is compared to the system with equal lengths no matter if the outer nanotube is larger or smaller. This work is in the process of being prepared for publication.

# 4.1 Introduction

Theoretical research of nanoscale devices has rapidly grown in recent years (see, for example, Buldum and Lu, 2001; Merkle, 1996; Sohlberg *et al*., 1997; McCurdy *et al*., 2002). It is expected that these devices will be miniature versions of electronic integrated circuits and mechanical systems (Forro, 2000), which will

process precisely, efficiently, and with high productivity, matter, energy, and information (Drexler, 1992). Research has primarily focused on structures that require precise control over the positioning of molecular systems in order to be built and perform the activities for which they were developed (Drexler, 1999). Technologies to manipulate such systems are in the very early stage of development (Cumings and Zetl, 2000; Yu *et al.*, 2000; Yu *et al.*, 2000), and include atomic force microscopy (AFM), and high-resolution transmission (TEM) and scanning (SEM) electron microscopy techniques, which are used to quantify and verify the mechanical properties of nanoscale structures. A promising class of nano-materials are double- or multi-wall carbon nanotubes, which has the appropriated structure to build devices in the nano scale (Merkle, 1993, Forro, 2000; Zheng and Jiang, 2002).

### 4.1.1 Carbon nanotubes synthesis

The technology to create carbon nanotubes has been known for more than a decade (Iijima, 1991), however, the experimental parameters that influence nanotube formation and control of the outer diameter, number of shells, internal conformation, and axial length remain under investigation (Li *et al.*, 2001; Siegal *et al.*, 2002; Suh and Lee, 1999). Using chemical vapor deposition over catalytic nanoparticles of discrete sizes, Li *et al.* (2001) have produced carbon nanotubes with diameters close to the size of the catalytic nanoparticles. The nanoparticles

employed were made of iron oxide, and were put in contact with methane and hydrogen at 1173 K. The result is nanotubes with axial lengths in the range of 0.01 to 10 μm, and outer diameters in the range of 1 – 2, and 3 – 5 nm, depending on the size of the nanoparticles. Suh and Lee (1999) have prepared uniform arrays of carbon nanotubes supported on porous anodic alumina through an electrochemical process. This process uses the anodic alumina as a template where cobalt is deposited at the bottom of the template, reduced, and put in contact with pyrolized acetylene to form well ordered nanotubes with highly uniform outer diameters (43.8 ± 0.8 nm), and lengths, which are confirmed by scanning electron micrographs. Using thermal chemical vapor deposition at atmospheric pressure, Siegal *et al.* (2002) have growth carbon nanotubes from a nickel film using a mixture of acetylene and nitrogen. These nanotubes have a very uniform outer diameter, which depends exponentially on the temperature employed during the process. Using a temperature of 923 K, this method produces nanotubes with an outer diameter of 5 nm, and 350 nm at 1073 K.

### 4.1.2 The internal conformation

Despite success in controlling the outer diameter, axial length and ordering of nanotubes supported on a surface, limited progress has been made in controlling the internal conformation of each wall in the system, which is the most important parameter in determining electric and mechanical phenomena. The internal

conformation is characterized by the chiral vector $(n,m)$. This vector dictates in which direction the graphite sheet is bent and rolled over to form the nanotube (Dresselhaus *et al.*, 2000). Nanotubes can be either of the armchair $(n = m)$, zigzag $(n = 0$, or $m = 0)$, or chair (any other $n$ and $m$) variety. This internal conformation can be determined experimentally using scanning tunneling microscopy for single-wall carbon nanotubes (Wildoer *et al.*, 1998; Odom *et al.*, 1998), but for double and multiwall nanotubes this method cannot be employed. Combining transmission electron microscopy and electron diffraction techniques, recently Kociak *et al.* (2002) have been able to deduce the chiral conformation of double wall carbon nanotubes, but experimental methods that can produce nanotubes with a specific chiral conformation have not been reported in the literature.

In terms of electrical properties, single-wall carbon nanotubes can be metallic or semiconducting (Baughman, *et al.*, 2002, Collins *et al.*, 2001); if they have the armchair conformation they are metallic; other conformations are semiconducting. Multiwall carbon nanotubes are complex composite mixtures of metallic and semiconducting nanotubes (Collins *et al.*, 2001). The metallic nanotubes support large current densities (Collins *et al.*, 2001, Fischer *et al.*, 1997), while semiconducting nanotubes have been employed to fabricate transistors at room temperature (Tans *et al.*, 1998).

Among the interesting mechanical properties exhibited by double-wall carbon nanotubes, superlubricity (very low friction forces compared to graphite) between their walls has been predicted theoretically (Damnjanovic *et al.*, 2002; Kolmogorov and Crespi, 2000). Using calculations of the corrugation energy, Damnjanovic *et al.* (2002) h ad predicted that, in general, the friction between the walls will be extremely low in multiwall nanotubes, and superlubricity is present for the case of incommensurate systems. This is a consequence of the low symmetry, or even complete disorder, between the walls in these systems. For any two nanotubes with chiral conformation $(n,m)$, and $(n',m')$, typically they will be incommensurate (but not always) if $n/m \neq n'/m'$, and commensurate if $n/m = n'/m'$ (Damnjanovic *et al.*, 1999). Using the same type of calculations, Kolmogorov and Crespi (2000) have estimated that the shear strength will be ~ 1 MPa for the commensurate systems where the corrugation energy scales with the size of the system and for incommensurate systems they find that the corrugation energy does not scale with size and the shear strength is ill defined. For simulation purposes, the internal conformations of multiwall carbon nanotubes can be chosen in order to produce systems that fall into the commensurate or incommensurate definitions.

### 4.1.3 Degree of commensurability and friction forces

There are several simulation and experimental studies of friction forces between surfaces at the atomic scale (Muser and Robbins, 2000; Wenning and Musser, 2001; Donnet *et al.*, 1996), which deal with the commensurability of the surfaces. Using molecular dynamics simulations in curved, non-adhering, dry surfaces, Wenning and Muser (2001) found different behavior for the friction force $F_f$ in commensurate, incommensurate, and amorphous systems with respect to the normal load $L$. For commensurate systems the dependence was found to be linear in the load, i.e. $F_f \approx L$; for amorphous systems $F_f \approx L^{0.66}$; for incommensurate systems the dependence was not clear, similar to the conclusion of Kolmogorov and Crespi (2000) for nanotube surfaces. If these incommensurate surfaces are contaminated with small lubricant molecules, then the dependence between the friction force and the normal load is well behaved, and $F_f \approx L^{0.85}$. Muser and Robbins (2000) have also studied flat commensurate and incommensurate atomically smooth surfaces; they found that commensurate surfaces hold together at zero lateral force and positive normal pressures, while incommensurate surfaces hold together at zero lateral force only when mobile atoms are present in the interface between the surfaces or if the walls are particularly soft.

Super-low friction has been observed experimentally in molybdenum disulphide coatings at high vacuum conditions, and in the presence of nitrogen atmospheres (Donnet *et al.*, 1996). Donnet *et al.* (1996) conclude that the presence of carbon, water, or oxygen increase the value of the shear strength, which at atmospheric air conditions is 56.0 MPa, while at ultra high vacuum conditions this decreased to 0.7 MPa.

In the case of double-wall carbon nanotubes, there is no possibility for molecules or atoms to be located between the walls that form the system because the intershell distance is 0.34 nm (same as graphite), which corresponds to the van der Waals diameter between carbon – carbon interactions.

### 4.1.4 Friction forces in the outer surface of carbon nanotubes

The friction force between the outer surfaces of carbon nanotubes with other material surfaces has been the focus of several molecular simulation studies (Buldum and Lu, 1999; Frankland *et al.*, 2002; Ni and Sinnott, 2001). For example, the sliding and rolling of carbon nanotubes on a graphite surface has been studied by Buldum and Lu (1999), who found that each chiral conformation of a nanotube has a unique minimum energy orientation with respect to the graphite surface. If the nanotube is pushed in any direction along the graphite

surface, the nanotube not only slides but also spins looking for a new energy minimum.

Using molecular dynamics simulations, Ni and Sinnott (2001) studied the responses of bundles of carbon nanotubes to shear forces between two sliding hydrogen-terminated diamond forces. They used an analytic reactive empirical bond-order potential coupled to a long-range Lennard-Jones potential (Mao *et al.*, 1999) and found that the shear forces are relatively weak at low compression levels (~ 0 GPa) of the diamond surfaces. At high compression levels (13.7 GPa), the nanotubes bend in the radial direction, producing forces 3 orders of magnitude higher than the system at low compression levels.

A many-body bond-order potential (Brenner, 1990) was used by Frankland *et al.* (2002) to study the carbon nanotube – polymer interface for cases when the nanotube was not linked to the polymer and when the nanotube formed cross-links involving ~ 1 % of the nanotube carbon atoms. For carbon nanotubes with chiral conformation (10,10) and a length of 5.3 nm, they found that when the nanotube was not linked, the shear strength is ~ 2.75 MPa independent of where the polymer formed a crystalline or amorphous matrix; for the case when the nanotube was linked to the matrix, the shear strength was 30 MPa for an amorphous matrix, and 110 MPa for the crystalline matrix.

Composite materials of carbon nanotubes and metals (Dong *et al.*, 2001), polymers (Lordi and Yao, 2000; Xu *et al.*, 2002; Liao and Li, 2001), and fullerenes (Kuzumaki *et al.*, 1998) have been the subject of several molecular simulation and experimental studies. Using a copper matrix reinforced with carbon nanotubes, Dong *et al.* (2001) found experimentally that the coefficient of friction decreased with the volume fraction content of carbon nanotubes in the composite. When the content of carbon nanotubes changed from 4 to 20 %, the friction coefficient decreased from 0.39 to 0.29. The effect is larger for the matrix carbon-reinforced / copper, where changing the same amount of carbon nanotubes, the coefficient of friction decreased from 0.43 to 0.29.

Carbon nanotube - reinforced epoxy thin films have been investigated experimentally by Xu *et al.* (2002), and using molecular mechanics simulations and micromechanics calculations. They found that strong interfacial adhesion exists using very low volume fractions of multiwall carbon nanotubes. Similar behavior was also found by Liao and Li (2001) in their simulations of carbon nanotube-polystyrene composites.

The shear strength of carbon nanotubes - fullerene composites was estimated experimentally by Kuzumaki *et al.* (1998) and, contrary to the behavior with polymers composites, this interface showed a shear strength of 0.044 MPa.

Shear sliding is observed probably caused by the weak bonding between these molecules.

### 4.1.5 Friction forces in the inner walls of carbon nanotubes

As shown by Damnjanovic *et al.* (2002), carbon nanotubes in general exhibit extremely low friction forces between their nested walls. The friction force and shear strength between these inner walls has been estimated experimentally by two groups. Yu *et al.*, (2000) attached a multiwall carbon nanotube to two tips through electric discharges and then proceeded to apply a tensile load until the outer shell of the multiwall nanotube broke. Using atomic force and scanning electron microscopy, the interaction force between the walls as a function of the contact length between the outer and the inner nanotubes was measured. Two systems were studied, one 2.2 μm in length with outer diameter of 30 nm and the second 7.5 μm in length and outer diameter of 36 nm. Analyzing the forces that act in this system, Yu *et al.* (2000) estimated that the dynamic and static shear strength were very low and equal; for the smaller system it was 0.30 MPa, while for the larger system it was 0.08 MPa. The difference between these two values was attributed to different interlayer spacing between the neighboring shells and the degree of commensurability in the studied systems.

Cumings and Zetl (2000) performed a similar experiment, where one end of a multiwall carbon nanotube was attached to a surface, while the other end was opened through a chemical reaction. The inner shell of the multiwall nanotube was attached to a tip through an electrical discharge. The inner shell was then pulled apart, released from the tip through another discharge, and the nanotube retracted by itself in a period of less than 1 ns. The exact time could not been quantified due to the physical limitations, but the experiment was observed using transmission electron microscopy. Based on this upper limit for the retraction time and estimating the van der Waals forces, they estimated that the static shear strength should be less than 0.66 MPa, while the dynamic shear strength should be less than 0.43 MPa.

### 4.1.6 Mechanical and electromechanical applications of multiwall carbon nanotubes

Simulations (Tuzun et al., 1995; Kolmogorov and Crespi, 2000), and theoretical studies (Merkle, 1993, Forro, 2000; Zheng and Jiang, 2002) have predicted interesting mechanical and electromechanical applications for these multiwall carbon nanotubes. Applications as rotational molecular nanobearings had been proposed by Merkle (1993), and Tuzun *et al.* (1995). They found that the potential energy of this nanobearing is periodic and a function of the rotational position; if the conformation of the walls is chosen to have short periods for the

potential energy, then the nanobearing will rotate without difficulty. The performance of these nanobearings will depend on the temperature, velocity, the size of the system, and the number of vibrational motions present in the walls (Kahn and Lu, 1999). Modifying this system to have electrical charges in the inner nanotube, Tuzun *et al.* (1995) proposed that these nanobearings could work as rotational molecular motors when two oscillating laser fields are applied to the system. From their simulation results, they obtained stable rotational motion at speeds up to about $10^{12}$ Hz. Forro (2000) proposed that by modifying the inner shell to have charges, an electron current will produce a separation of the inner shell due to the Faraday cage effect; when the system is released of electron current, van der Waals interactions will restore the system to its original position. Taking into account these two effects, this system is proposed to work as an electromechanical nanoswitch.

The last application was proposed by Zheng and coworkers (Jiang (2002), and Zheng *et al*., (2002)), and is the object of study in this work. They proposed that if both ends of the outer nanotube are eliminated, and the inner shells are pulled apart from the outer nanotube to a distance where there is still some contact area, then the nanotube will retract and will cross the outer nanotube starting a process of oscillation which will stop after some period of time. Based on estimations for the van der Waals interactions between the shells of the

nanotubes, they predicted that those oscillations will show frequencies in the scale of GHz.

## 4.2 Potential model

The potential model employed in this work for carbon nanotubes was developed by Guo *et al.* (1991). This model consist of bond stretching (Morse potential), angle bending, coupled bond stretching - angle bending, twofold torsions for the intramolecular interactions, and Lennard-Jones intermolecular interactions between the carbon atoms that form the nanotubes. The model was fitted for $sp^2$ carbon centers using experimental lattice parameters, elastic constants and phonon frequencies for graphite. This model has been used to predict the packing structures of fullerenes $C_{60}$ and $C_{70}$. It has also predicted heats of sublimation for these molecules in excellent agreement with experimental results (Pan *et al.*, 1991). Other studies used this model to predict uniaxial-strain behavior, packing structure, lattice parameters, vibrational modes and frequencies for bulk, and insolated carbon nanotubes (Gao *et al.*, *Nanotechnology*, 1998), and doped carbon nanotubes with potassium atoms (Gao *et al.*, *Phys. Rev. Lett.*, 1998). Tuzun *et al.* (1996) simulated for first time the flow of fluids inside carbon nanotubes using this potential model; they

compared the flow of helium and argon and found that both molecules flow more easily through static a carbon nanotube than a dynamic one and as expected helium flowed more easily than argon.

### 4.2.1 Description of the potential

In the Gao *et al.* (1991) potential, the intramolecular interactions are given in the following equations where $E_{INT2}$, $E_{INT3}$, $E_{INT2-3}$, and $E_{INT4}$ are the 2-, 3-, coupled 2 and 3-, and 4-body interactions, respectively:

$$E_{INT2}(r_{ij}) = D_2\left[1-\exp\left(-\alpha\left(r_{ij}-r_e\right)\right)\right]^2 \tag{4.1}$$

$$E_{INT3}(\theta) = \frac{1}{2}D_3\left(\cos\theta-\cos\theta_e\right)^2 \tag{4.2}$$

$$\begin{aligned} E_{INT2-3}(\theta) = {} & D_{2-3,1}\left(r_A-r_e\right)\left(\cos\theta-\cos\theta_e\right)-D_{2-3,2}\left(r_C-r_e\right)\left(\cos\theta-\cos\theta_e\right)- \\ & D_{2-3,3}\left(r_A-r_e\right)\left(r_C-r_e\right) \end{aligned} \tag{4.3}$$

$$E_{INT4}(\phi) = D_4\left[1-\cos(2\phi)\right] \tag{4.4}$$

where $r_{ij}$ is the distance between sites $i$ and $j$, $\theta$ is the angle formed by the contiguous bonds $r_A$ and $r_C$, and $\phi$ is the dihedral angle. The parameters for

equations (4.1) – (4.4) are: $D_2$ = 3283.88 K, $\alpha$ = 2.18676 $\text{A}^{-1}$, $r_e$ = 1.418 A, $D_3$ = 98706.59 K, $\theta_e$ = 120.00, $D_{2-3,1}$ = $D_{2-3,2}$ = -36441.87 $\text{KA}^{-1}$, $D_{2-3,3}$ = 34222.44 $\text{KA}^{-2}$, and $D_4$ = 5354.81 K.

Intermolecular interactions include Lennard-Jones interactions between carbon atoms of different atoms:

$$E_{LJ}\left(r_{ij}\right) = 4\varepsilon\left[\left(\frac{\sigma}{r_{ij}}\right)^{12} - \left(\frac{\sigma}{r_{ij}}\right)^{6}\right] \tag{4.5}$$

where $\varepsilon$ = 34.83 K, and $\sigma$ = 3.4 A.

## 4.2.2 Implementation for carbon nanotubes

Carbon nanotubes are large molecules with hundreds of atoms, each of which can participate in up to three bond-stretch, nine angle-bend, and 26 torsional interactions. However, the periodicity of the unit cells that form the nanotube helps define and calculate these interactions in a computationally efficient manor in a simulation program. Consider the case of bond stretching in a carbon nanotube with chiral conformation (3,3). Taking a graphite sheet with an orientation as shown in Figure 4.1, the chiral vector indicates that we move 3 hexagons to the right, and 3 hexagons at a 60° angle (shown in red vectors),

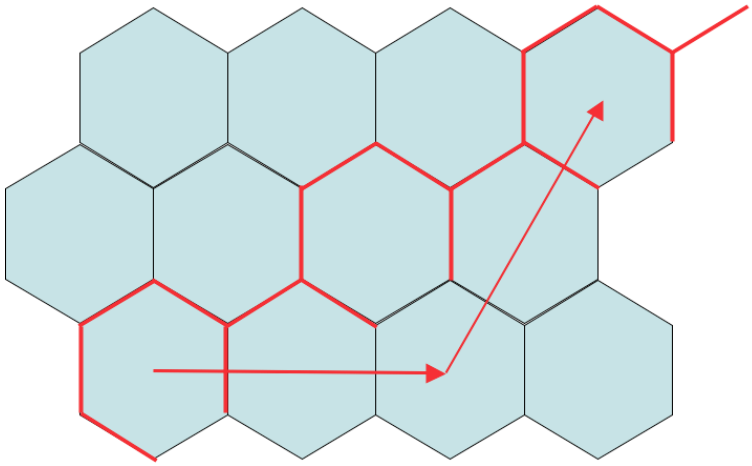

Figure 4.1. The graphite sheet with the chiral vectors that represent the conformation (3,3). The red lines represent the basic unit cell for this chiral conformation.

and then we will find the position of the hexagon (3,3) to which the original hexagon is linked. The red lines indicate the atoms and the bonds that form the minimum unit cell.

This unit cell repeats along the axial direction of the nanotube. If we numerate the atoms with the order: (number of cell, number of subcell, position in cell), then we see that there are two subcells, and every subcell contains twice the number of the chiral vector (i.e. 2 x 3), as shown in Figure 4.2.

If we index the atoms in this way, we can calculate the total contribution in the nanotube to the intramolecular potential due to bond stretching:

$$
\begin{aligned}
E_{INT2,TOTAL} = \sum_{i=1}^{N_{cells}-1} \Bigg\{ & \left( \sum_{j1=1,3,\ldots,N_{ASC}-1} U_{INT2}\left(r_{(i,1,j1),(i,1,j1+1)}\right) \right) + \left( \sum_{j2=2,4,\ldots,N_{ASC-2}} U_{INT2}\left(r_{(i,2,j2),(i,2,j2+1)}\right) \right) + \\
& U_{INT2}\left(r_{(i,2,1),(i,2,N_{ASC-2})}\right) + \\
& \left( \sum_{j3=1}^{N_{ASC}} \left( U_{INT2}\left(r_{(i,1,j3),(i,2,j3)}\right) + U_{INT2}\left(r_{(i,2,j3),(i+1,1,j3)}\right) \right) \right) \Bigg\} \\
+ & \sum_{j4=1,3,\ldots,N_{ASC}-1} U_{INT2}\left(r_{(N_{CELL},1,j4),(N_{CELL},1,j4+1)}\right)
\end{aligned}
\tag{4.6}
$$

where $N_{CELL}$ is the number of cells, $N_{ASC}$ is the number of atoms per subcell. Notice that the last cell should contain only the atoms corresponding to the first

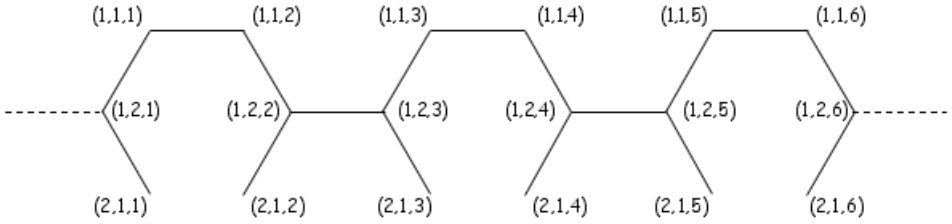


Figure 4.2 The basic unit cell for the chiral conformation (3,3). The numbers in the parenthesis represent the order of each atom: (number of cell, number of subcell, position in subcell).

subcell. Equation (4.6) is only valid for nanotubes with chiral conformation $(n,n)$, but similar expressions can be derived for nanotubes with different chiral conformation, and similar indexing can be used to calculate the rest of the intramolecular interactions.

# 4.3 Methodology

## 4.3.1 Nanotubes: Cartesian coordinates

In order to perform the molecular simulations, we obtained the Cartesian coordinates of the carbon atoms using the relations established by White *et al.* (1993), and Ebbesen (1997) which use the helical and rotational symmetric properties of the nanotubes to obtain the $(x,y,z)$ positions of each atom.

Every nanotube has a periodic unit cell that repeats along the axial direction of the nanotube and depends on the chiral conformation $(n,m)$ . This unit cell is conformed by carbon atoms forming helical structures. For example, for a nanotube with chiral conformation (3,2), the unit cell consists of a delimited surface of graphite as shown in Figure 4.3 (left). This unit cell repeats in the

axial direction of the nanotube as shown in the Figure 4.3 (right). If we introduce the set of primitive vectors $\mathbf{r}_1$ and $\mathbf{r}_2$, then vector $\mathbf{B}$ which properly characterizes the chiral conformation is the vector formed by the sum of vectors $n\mathbf{r}_1$ and $m\mathbf{r}_2$. Vector $\mathbf{B}$ is a vector in the radial direction of the nanotube, and it forms the base of the nanotube. The direction of vector $\mathbf{H}$ forms the helical structure with respect to the vector base $\mathbf{B}$. Along this vector $\mathbf{H}$, the first two atoms of the helical structure are located. These two atoms are located at the positions $\mathbf{d} = (\mathbf{r}_1 + \mathbf{r}_2)/3$ and $2\mathbf{d}$ with respect to the center of the original hexagon.

The nanotube has a radius of $|\mathbf{B}|/2\pi$, and a symmetrical rotational axis $C_N$, where $N$ is the largest common divisor of $m$, and $n$. To build the nanotube, the first atom is located arbitrarily in any point of the surface of the nanotube and the second atom is located by rotating the first point by $2\pi(\mathbf{d}\cdot\mathbf{B})/|\mathbf{B}|^2$ radians about the cylinder axis with a translation $|\mathbf{d}\times\mathbf{B}|/|\mathbf{B}|$. The positions of these two atoms are used to locate the rest of the atoms that are located at the same axial distance and they repeat $N-1$ times, then those atoms are located by rotating the first two by $2\pi/N$ radians, $N-1$ rotations, and this procedure complete the basic subcell of the nanotube. In order to find the rest of the positions of the atoms we need to determine the "screw" function $S(h,\alpha)$, which represents a translation of $h$ units along the nanotube axis in conjunction with a rotation of $\alpha$ radians. This screw function requires that there must exist a real lattice vector $\mathbf{H} = p\mathbf{r}_1 + q\mathbf{r}_2$ in the

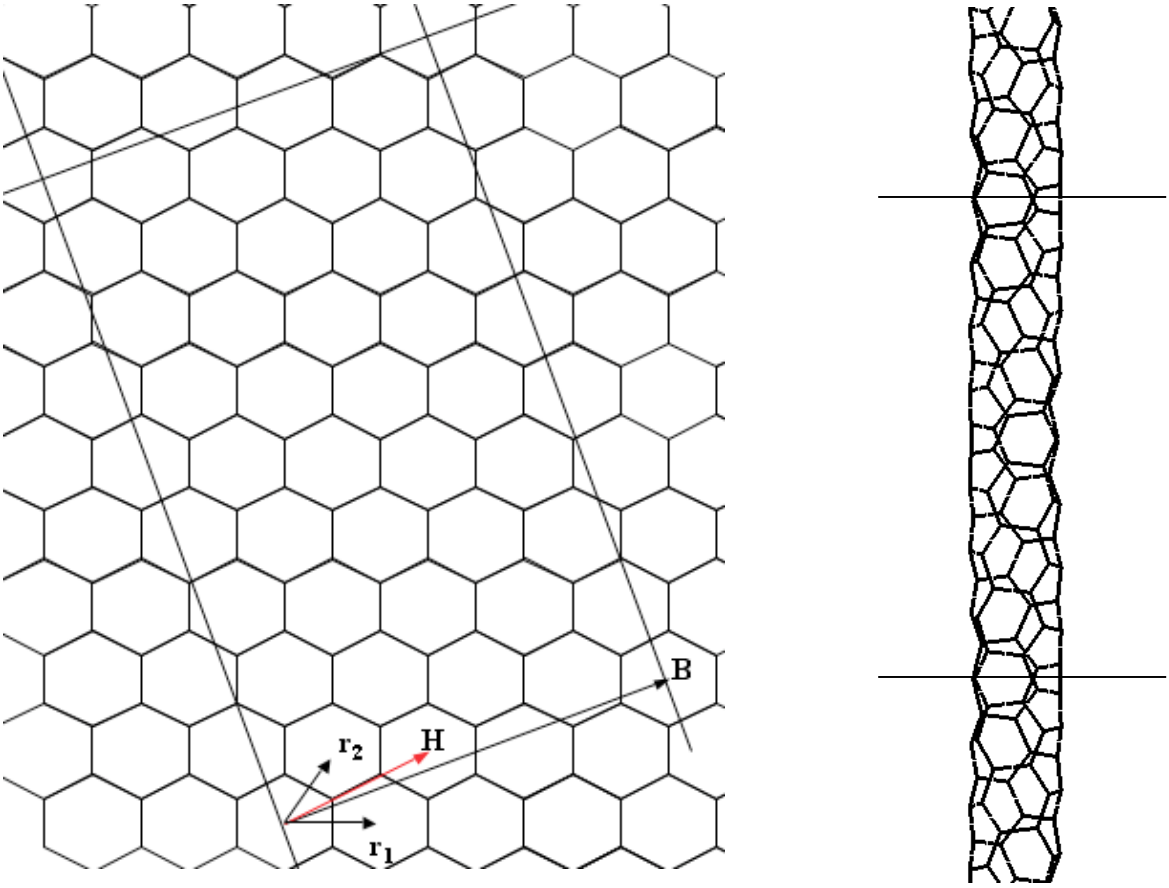


Figure 4.3 The graphite sheet with the chiral vectors $\mathbf{r}_1$, $\mathbf{r}_2$ that represent the chiral conformation (3,2). $\mathbf{B}$ represent the base vector, and $\mathbf{H}$ the helical vector. The rectangular area represents the cylindrical area of the nanotube, which covered an axial length represented in the right side of the figure.

honeycomb lattice such that $h = |\mathbf{H} \times \mathbf{B}|/|\mathbf{B}|$, and $\alpha = 2\pi(H \cdot \mathbf{B})/|\mathbf{B}|^2$, and therefore $(p,q)$ of vector $\mathbf{H}$ must satisfy $pm - qn = \pm N$. Once the screw function is defined, the rest of the atoms are located by applying it to the original subcell.

## 4.3.2 Molecular simulations details

The algorithm employed to integrate the equations of motion was the reversible reference system propagator algorithm (r-RESPA) developed by Tuckerman *et al.* (1991) with a Nose´ thermostat (Nose, 1984; Tuckerman *et al.*, 1992). In this algorithm, fast (intramolecular forces), and slow motions (intermolecular interactions) are integrated over different time scales. The system is coupled to a Nose´ bath with an appropriated coupling variable that produces small fluctuations when the temperature of the bath is readjusted. This algorithm has been tested for macromolecules (proteins and fullerenes) (Humphreys *et al.*, 1994, Procacci and Berne, 1994) and compared to standard Verlet algorithms it has been shown to speed up the computation time between 4 - 5, and 20 – 40 times for systems with and without electrostatic interactions, respectively. The time-steps for slow and fast motion employed in this work were 2.21 fs, and 0.221 fs, respectively.

In this work, molecular simulations of the oscillatory behavior of double-wall carbon nanotubes proposed by Zheng and Jiang (2002) were performed using molecular dynamics in the canonical ensemble. Before the oscillatory

phenomena can occur, the systems should be pulled apart in order to have a small area of contact and the retraction occurs followed by the oscillations. Simulations were carried out in 3 steps, initial equilibration with no external force, followed by a period with external force applied until separation occurs, and simulation of the oscillatory behavior. The initial configurations were equilibrated for a period of 22 ps. After that, an external force was applied to the inner nanotube, and a force with the same magnitude but opposite sign was applied to the outer nanotube.

The magnitude profile of the applied force as function of the simulation time is plotted in Figure 4.4. This profile was built mixing step and hyperbolic tangent functions. The advantage of using this profile is that there are short periods when the force is incremented followed by periods where the force remains constant; this allows the system to relax before a new increment in the magnitude of the force occurs. Before using this profile of the force, constant increments of the external force produced very low separations or complete separation of the two nanotubes, since the low friction forces in these systems makes it difficult to control the distance of separation. A sketch of the phenomena simulated is shown in Figure 4.5, where at step (a) two external forces are applied to an equilibrated double-wall carbon nanotube with opposite directions. Once the magnitude of the force is high enough, the system starts to separate and before the system separates completely the external force is eliminated (b).

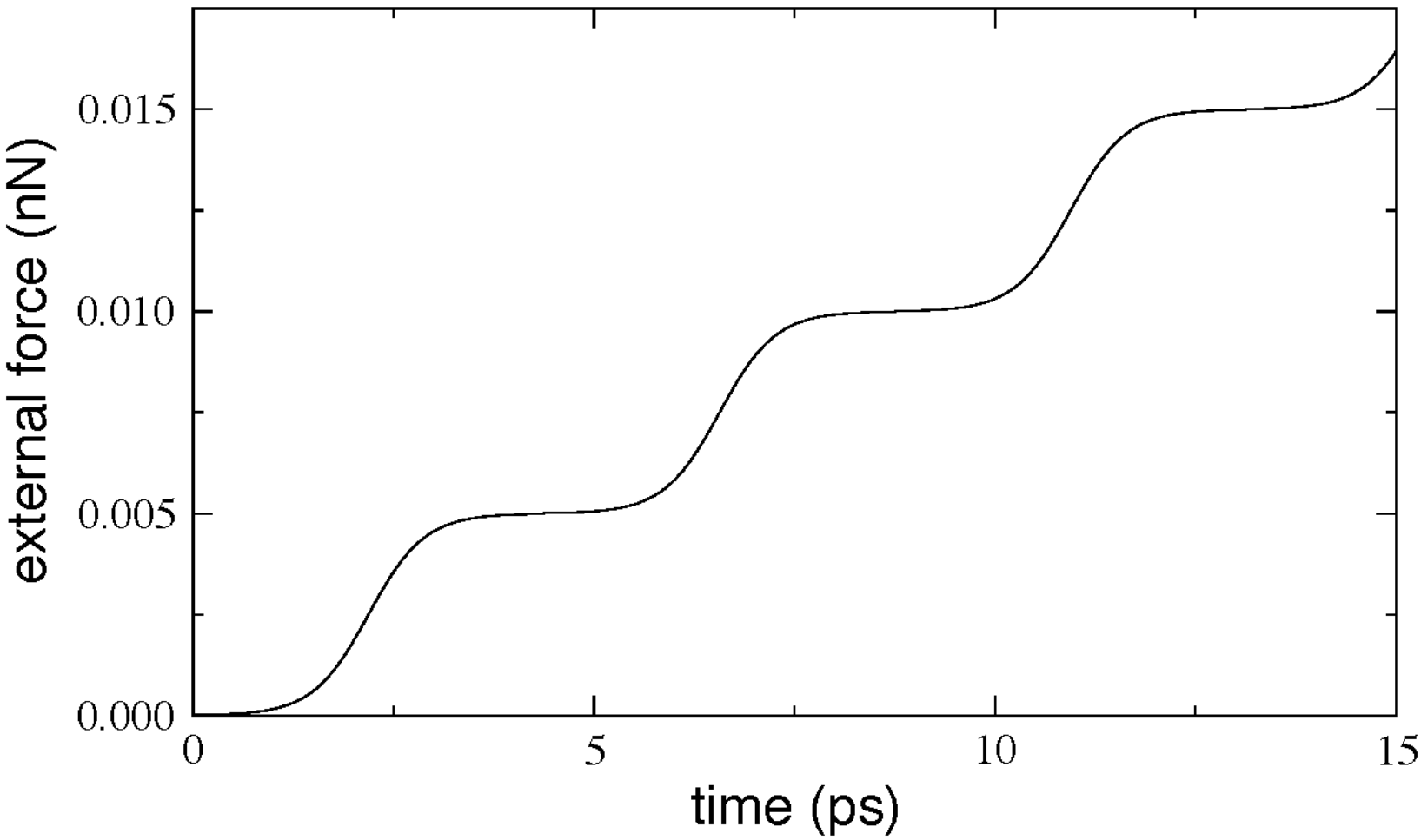


Figure 4.4 Profile of the applied external force to the inner nanotubes. An equivalent force with opposite sign was applied to the outer nanotube.

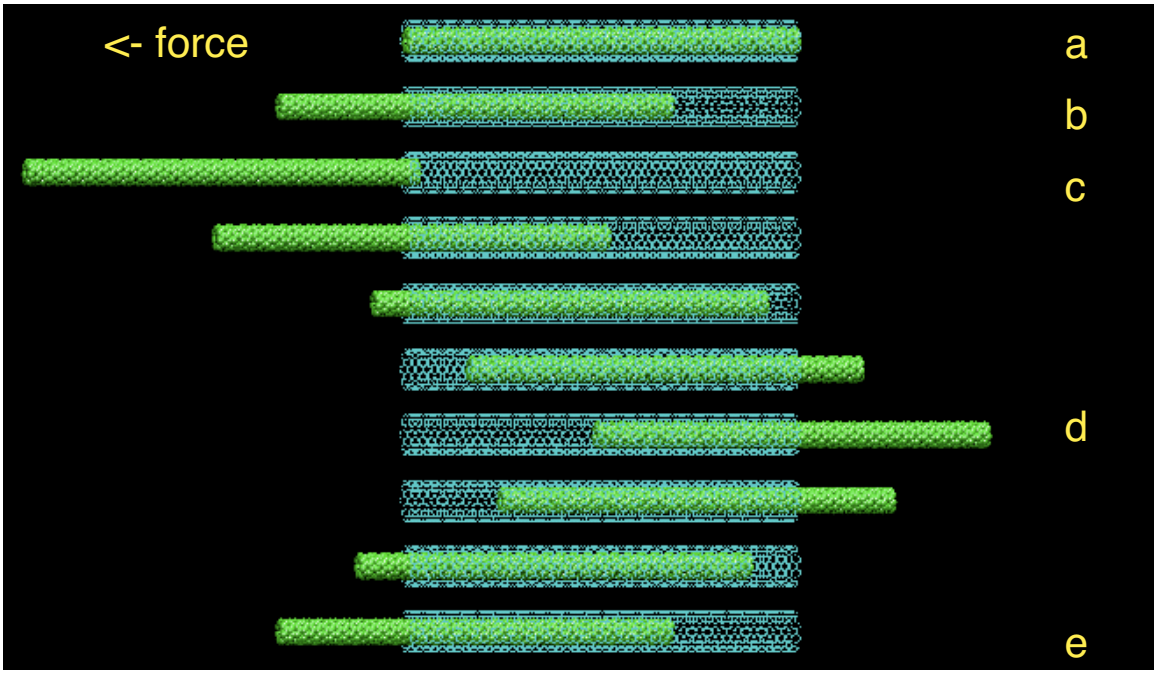


Figure 4.5: Snapshots of the induced separation through an external force and the damped oscillatory behavior after the system was released from the external force. The system plotted corresponds to chiral conformations (7,0) / (9,9) with length of 12.21 nm. The labeled steps are a) force applied to the initial equilibrated system, b) releasing the system from the external force, c) first maxima of separation in the first end, d) first maxima in the second end, and e) second minima in the first end.

Due to the impulse of the external applied force and the low friction forces between the walls, the nanotube continues separating until it reaches a separation with a minimum contact area (c). The time (b) where the external force is eliminated was tested by trial and error until the separation at time (c) corresponded to a contact area of a few Angstroms. After this event, the inner nanotube retracted by itself due to the attractive van der Waals interactions and after reaching a zero separation, the nanotube continued its movement and separated through the other end, until it reaches a maximum (d), and continues oscillating until reaching an equilibrated position again.

The effect of the magnitude of the initial applied external force is shown in Figure 4.6 for a double-wall carbon nanotube with chiral conformations (7,0) / (9,9) and a length of 98.24 nm. In this figure the separations in the axial direction between the centers of mass of both nanotubes are plotted as a function of time. After 50 ps of increments in the magnitude of the external force, the system starts to separate and at point (b) (~125 ps) the system is released of the external force. Even though the system has a separation of only ~32 nm at this point, the system continues separating until it reaches a maximum separation of ~83 nm at ~243 ps, corresponding to a minimal overlap between inner and outer nanotubes. Points (d) and (e) correspond to the similar events marked in the sketch of Figure 4.5. Lines red and green correspond to the second and third experiments where the magnitude of the external force was smaller. For the second

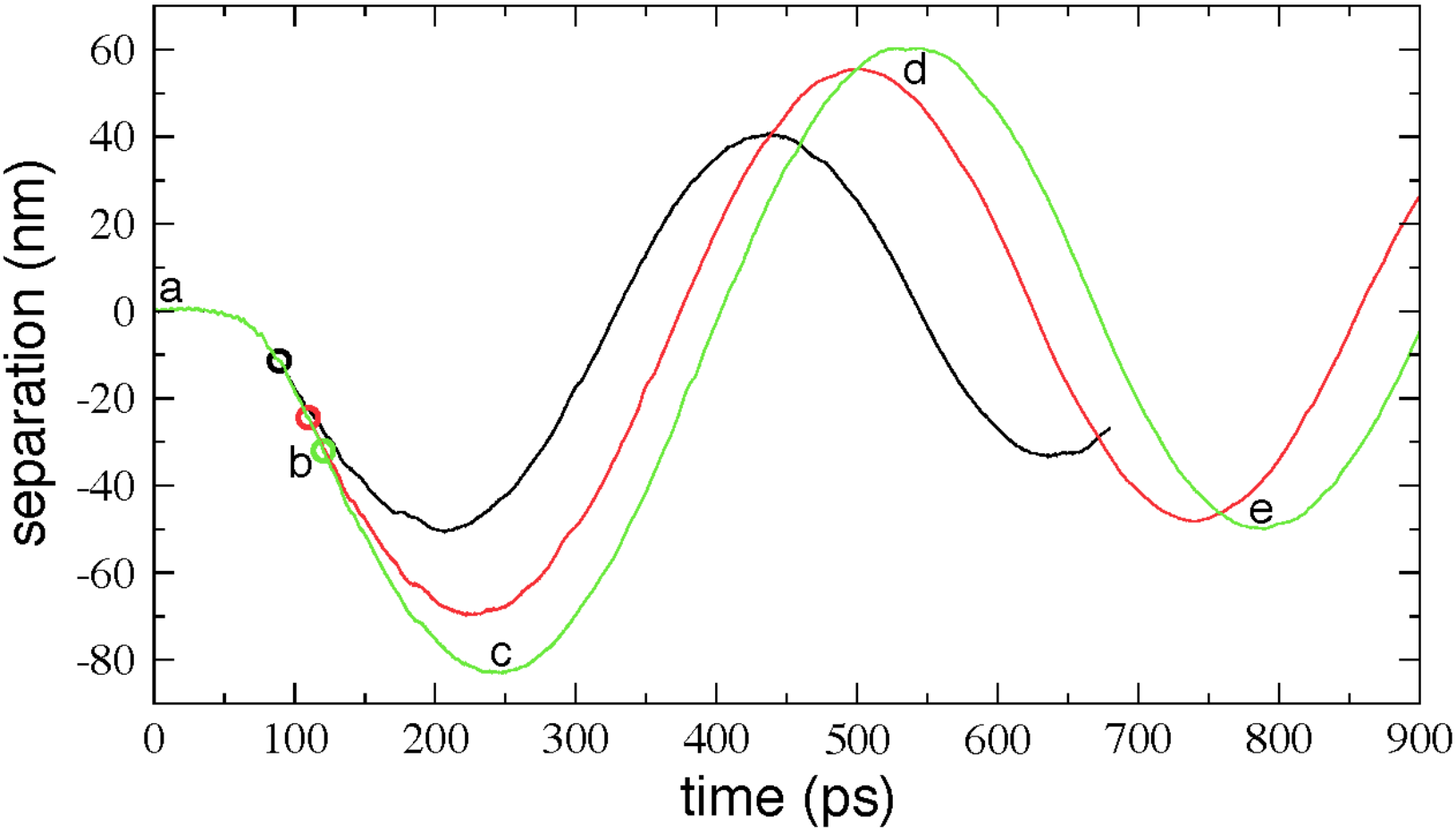


Figure 4.6: Separation of centers of mass as function of time for chiral conformations (7,0) / (9,9) and length of 98.24 nm. The three lines correspond to the system exposed to longer periods of external force. Points a) through e) correspond to the snapshots in Figure 4.5.

experiment even though the initial separation at point (b) is ~24 nm, the system reached a maximum at ~70 nm, for the third experiment the corresponding separations were ~11 and ~50 nm. This nanotube takes ~540 ps to complete the initial oscillation.

## 4.4 Results

The procedure described in section 4.3.3 was applied to incommensurate double-wall carbon nanotube systems with the same chiral conformations (7,0)/(9,9), but different axial lengths: 12.21, 24.56, 36.92, 49.27, and 98.24 nm at 298.15 K. For these systems, the inner and outer shell had the same axial lengths. Another set of simulations were performed keeping the inner length at 12.21 nm and using axial lengths for the outer nanotube with -30% to +40% increments with respect to the inner nanotube axial length. The effect of the temperature was studied for the system with axial length of 12.21 nm in the range of temperatures from 275 to 450 K. The effect of larger intershell separation was studied using the system with chiral conformations (7,0)/(10,10) and lengths from 24.56 to 49.27 nm at 298.15 K. Commensurate systems were studied using the chiral conformations (5,5)/(10,10) with axial lengths from 12.21 to 49.27 at 298.15 K.

### 4.4.1 The incommensurate system (7,0) / (9,9)

The incommensurate system with chiral conformations (7,0)/(9,9) was simulated using equal axial lengths for the inner and outer nanotubes at 298.15 K. For this conformation, the carbons in the outer shell are located in a cylinder with outer diameter of 1.22 nm and the intershell separation between the inner and outer cylinders is 0.34 nm. Five systems were simulated using axial lengths of 12.21, 24.56, 36.92, 49.27, and 98.24 nm. These systems contained between 2600 and 21000 carbon sites. Results of the separation between the centers of mass as a function of time are shown in Figure 4.7; this plot shows the simulation results starting from the point where the system reached the first minimum or point (c) in Figure 4.5. This facilitates comparison between the different simulations. Simulations were performed for 3 ns and over this period of time only the smallest system ceased oscillations almost completely at ~2.5 ns. For the largest system only 0.85 ns were simulated because of the long time required to simulate such a system with 21000 carbon sites. In this shorter time period with almost two oscillations, it showed the same tendencies as the smaller systems. The first oscillation in all systems seemed to have different dynamics than the rest of the oscillations, because the relation between the minimum and maximum separations in that oscillation had a significantly bigger ratio than the following oscillations.

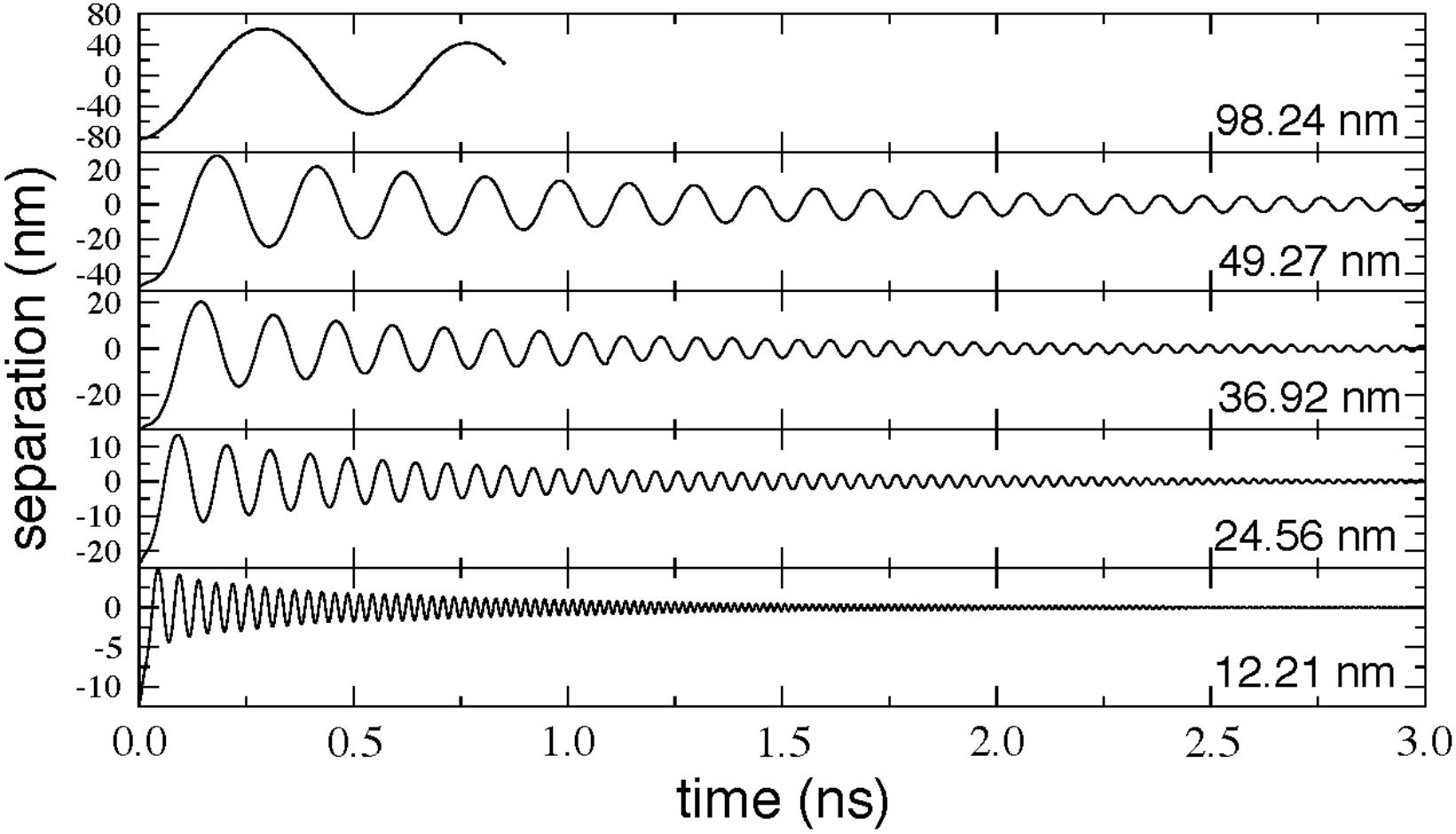


Figure 4.7: Separation of centers of mass as a function of time for 5 systems with chiral conformations (7,0) / (9,9) and lengths from 12.21 to 98.24 nm. The initial separation corresponds to a contact length of 0.3 nm.

The frequency of each oscillation was calculated for all systems in this period of time and the profile of these frequencies of oscillation are plotted in Figure 4.8 as function of the simulation time. All systems showed frequencies on the order of GHz, consistent with prior theoretical work (Zheng and Jiang, 2002; Zheng *et al.*, 2002). Frequencies of this magnitude have also been reported for other nanoscale systems such as the oscillatory attraction-repulsion of two nanoparticles of long hydrocarbon molecules in vacuum (Hathorn *et al.*, 2002). In general terms, the average value of the frequency in each profile decreases with the axial length of the system. For the smallest nanotube, frequencies started at ~19 GHz, increased almost linearly for ~1.65 ns to a value of ~63 GHz with a slope of ~27 GHz/ps. After this point, the frequencies remained almost constant for the remainder of the simulation. After the damped oscillations almost ceased at ~2.5 ns, the natural modes in the axial vibration of both nanotubes make small oscillations with high frequencies having an average value ~75 GHz but with large fluctuations (~8 GHz). For the system with axial length of 24.56, 36.92, and 49.27 nm, there is also a period of time where the simulations increased linearly with slopes of 9.68, 6.43, and 2.91 GHz/ps, respectively. From these profiles it is obvious that the systems with axial lengths of 24.56 nm and up did not reach an equilibrated configuration where the oscillation started to fluctuate around a constant value. We were only able to run the biggest system for a period corresponding to two oscillations, so the dependence of frequencies on time cannot be extracted over such a short trajectory.

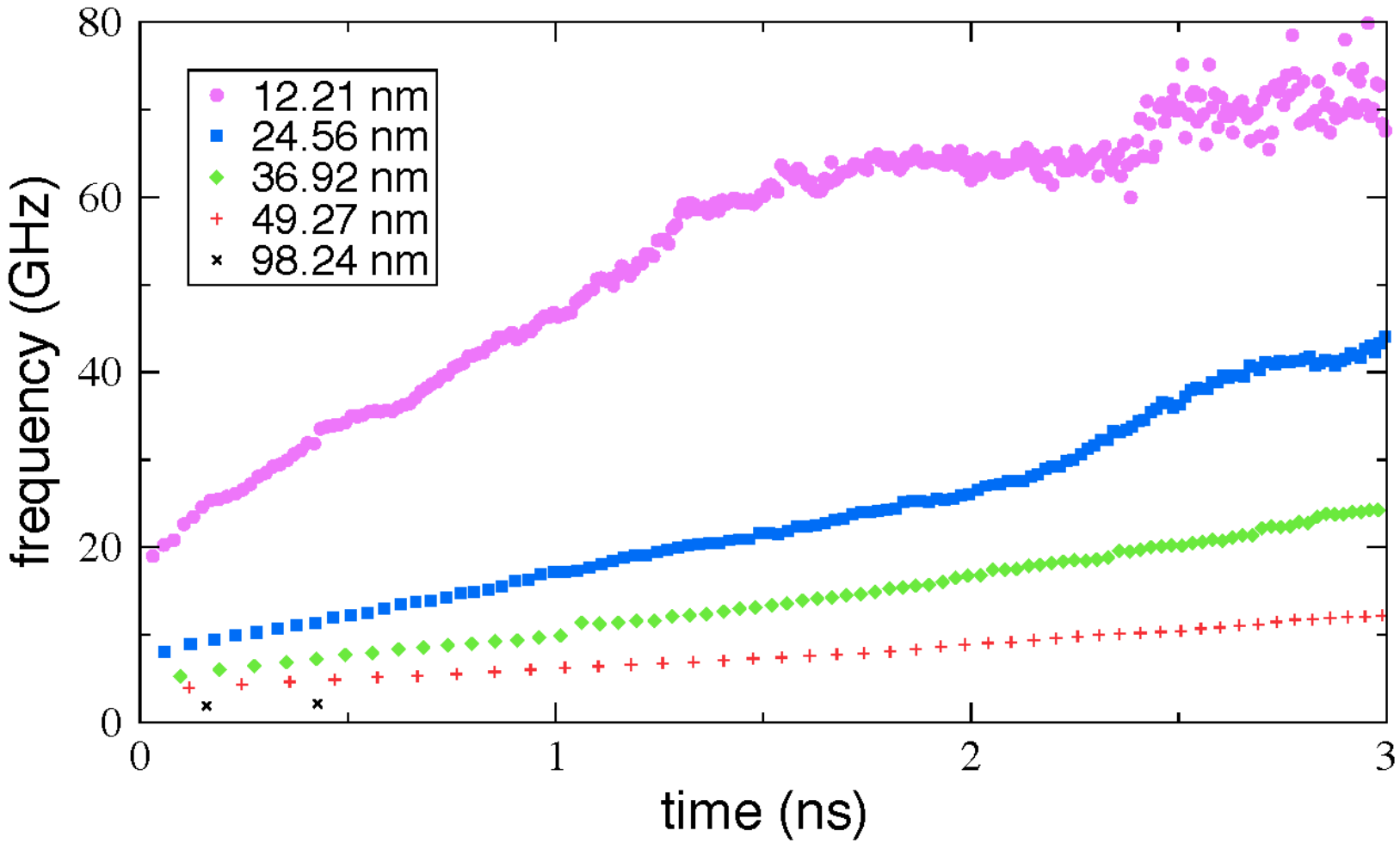


Figure 4.8: Frequency of the damped oscillations as a function of time for 5 systems with chiral conformations (7,0) / (9,9) and axial lengths from 12.21 to 98.24 nm.

In order to perform a more rigorous comparison between the frequencies and the axial length of the system, the initial frequency is plotted against the axial length in Figure 4.9. The open circles represent the simulation results for the frequency $f$ and the red line represents the best fitting using a function proportional to the inverse of the axial length:

$$f\left(GHz\right) = \frac{197.903\ GHz\ nm}{length\ (nm)} \tag{4.7}$$

This behavior is in agreement with theoretical predictions of Zheng and Jiang (2002), where they estimated that the frequency of these oscillations as:

$$f = \frac{\beta}{4}\sqrt{\frac{c_1 \Pi}{L_C \Delta}} \tag{4.8}$$

with $\beta = \sqrt{1-\delta}\,/\left(1-\delta/2\right)$, where, $\delta = \left|L_o - L_c\right|/2\Delta$ is the relative length mismatch, $\Delta$ is the initial extrusion, $L_o$ and $L_c$ are the length of the inner and outer shells respectively, $c_1$ is a variable that depends on the number of shells and their intershell separation, and $\Pi$ is an average value for the van der Waals interactions that depends only on the number of shells in the core. For our simulations, the inner and outer shells had the same length $\left(\beta = 1\right)$, and the frequency will depend only on the extrusion and inner shell lengths, which for our case had almost the same value $\left(\Delta \approx L_c\right)$, therefore the frequency will be proportional to the inverse of the axial length, as we found in the simulation results.

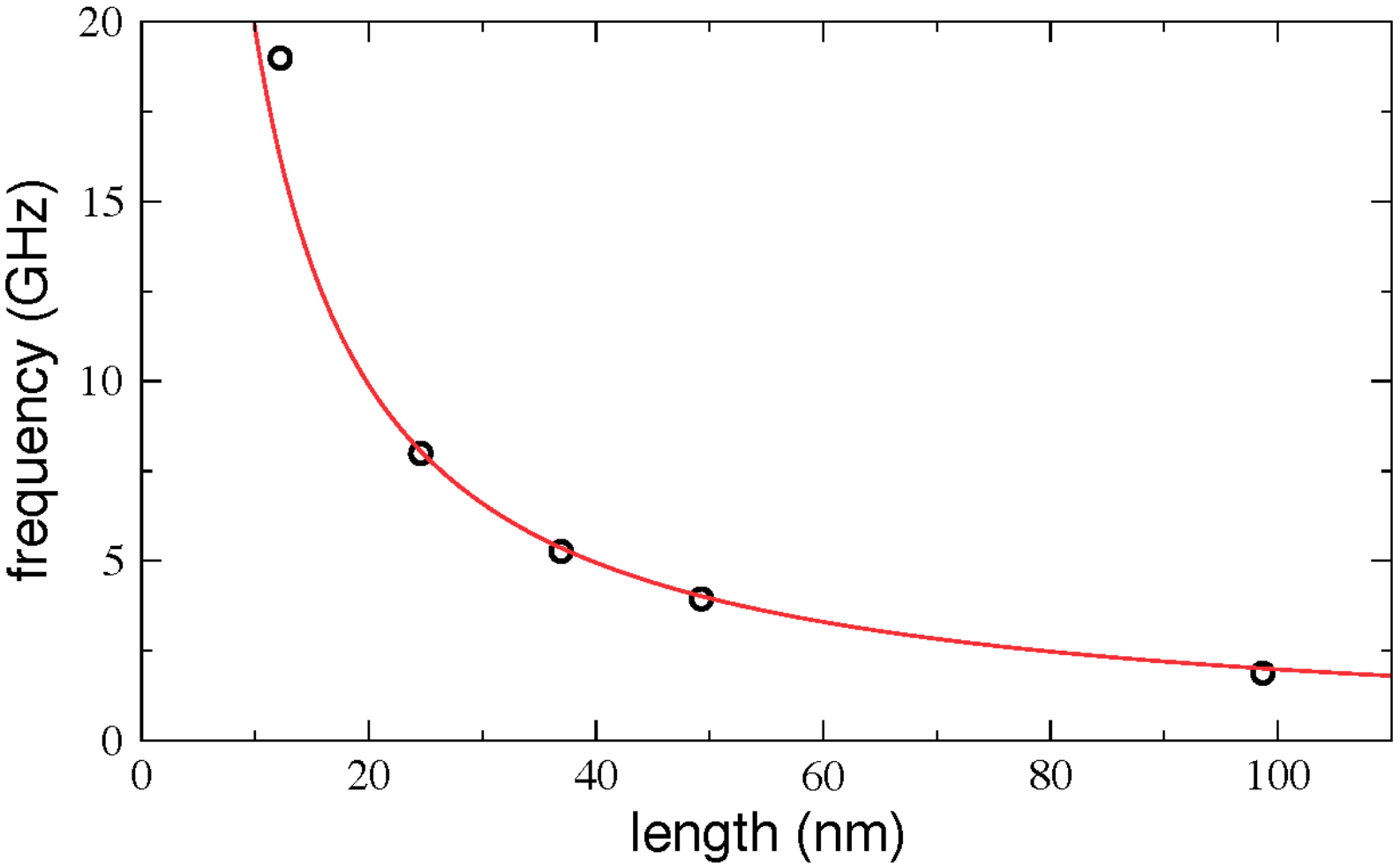


Figure 4.9: Frequency of the initial oscillation as a function of the axial length of the nanotubes for chiral conformations (7,0) / (9,9). The red line is the fitted curve to the inverse of the length.

### 4.4.2 Mechanical model with constant effective forces

In order to understand the forces that contribute significantly to this damped oscillatory behavior, a mechanical model was developed. In Figure 4.10, two oscillations for the nanotube with axial length of 24.56 nm are shown in the top of the Figure from 0.05 to 0.28 ns. The velocities of these separations were calculated as the numerical derivatives and are also shown in Figure 4.10. The axial and normal forces acting on the inner nanotube were computed during the simulation and are plotted in the bottom of Figure 4.10. The velocities showed small fluctuations close to the zero separations, reflecting the behavior of the axial force, which changes abruptly in sign at those points. From the velocity profiles we can conclude that the slopes are constant, therefore the acceleration should be constant and will depend only on the sign of the separation, hence a constant effective force should describe this behavior. Looking at the profiles of the axial force, we can see that the inner nanotube feels almost constant axial forces when the inner nanotube is entering or leaving the outer nanotube and changes sign when the nanotube is passing through zero separation. The normal forces acting over the inner nanotube are high compared to the axial forces (~5/1), but the actual forces that dictate how the system behaves, will be a fraction of these forces.

If we divide one oscillation into four regions as shown in Figure 4.11, then we can

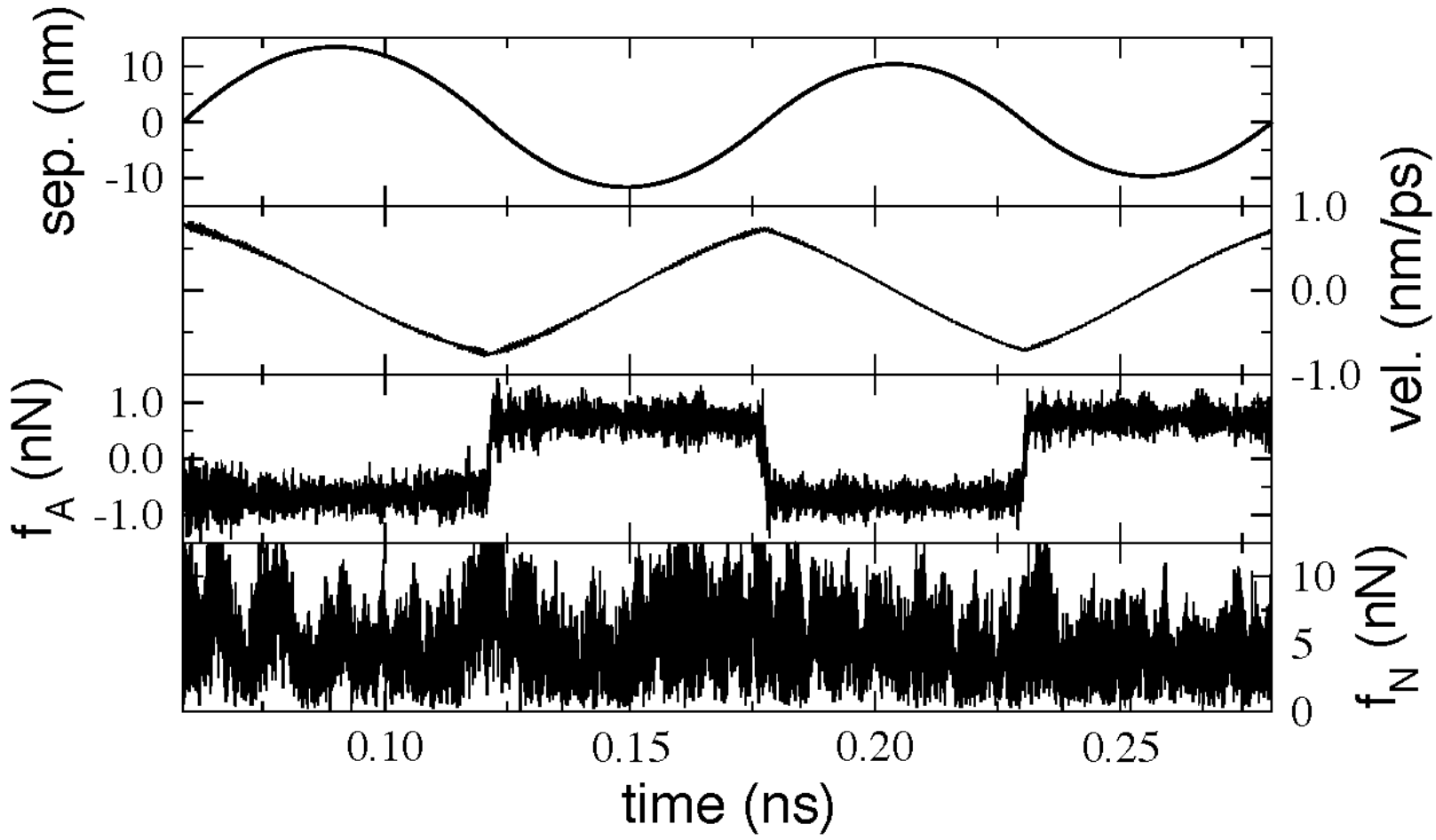


Figure 4.10: Two oscillations of the separation of the centers of mass for the system with length of 24.56 nm. Velocities are the numerical derivatives of the separation. $f_A$ and $f_N$ are the axial and normal forces, respectively, acting over the inner nanotube during the simulation.

see that we have equivalent regions when the inner nanotube is entering the outer nanotube from one or the other end, and when the inner nanotube is leaving. In region I of Figure 4.11, when the inner nanotube is entering from one end we assume that the tube experiences a constant force $F_I$ that opposes the motion (see Figure 4.10). We can solve the differential equation with its boundary conditions:

$$\begin{aligned} F_I &= m_n \frac{d^2 z}{dt^2} \\ \frac{dz}{dt}(t=0) &= 0 \\ z(0) &= z_0 \end{aligned} \tag{4.9}$$

to produce:

$$z = z_0 + \frac{F_I}{2m_n} t^2 \tag{4.10}$$

where $m_n$ is the mass of the inner nanotube, $z$ is the separation of the inner nanotube center of mass from the outer nanotube center of mass, and $z_0$ is the minimum value of the separation. For region III, the same equation applies but the effective force has an opposite sign. For region II, a similar procedure yields:

$$z = v_0 t - \frac{F_{II}}{2m_n} t^2 \tag{4.11}$$

where $v_0$ is the initial velocity at $z = 0$ in region II. The profile in Figure 4.11 was fitted to these expressions, and they are shown with the dotted red lines for regions I, and III, and dotted green lines for regions II, and IV.

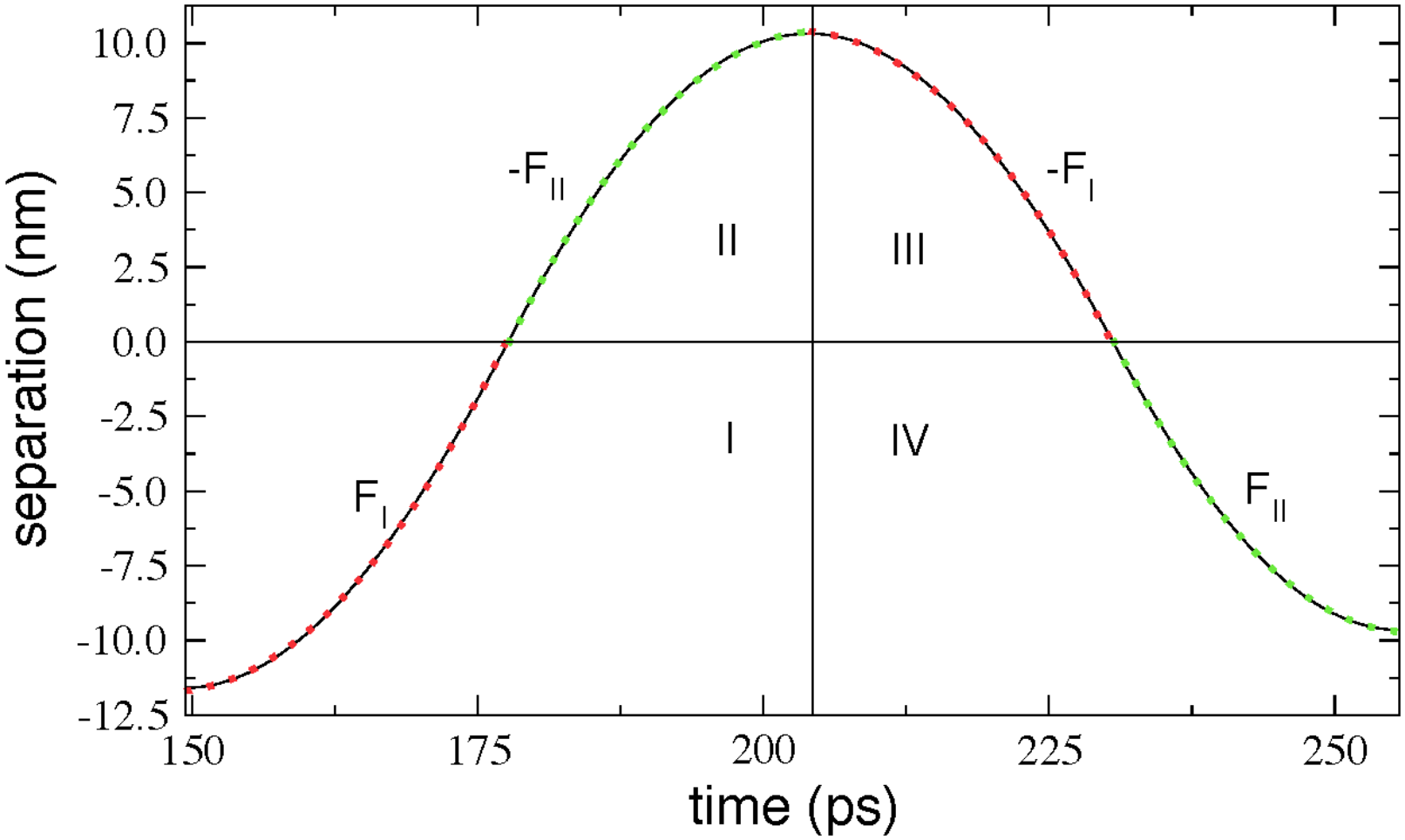


Figure 4.11: Division of the oscillation in four sections with different constant effective forces. Red and green dotted lines represent the fitting to the mechanical model.

Each oscillation of the system with axial length of 24.56 nm was fitted using equations (4.10) and (4.11) and the equivalent equations for regions III, and IV. Results of the absolute fitted values for the effective forces ($F_I$ and $F_{II}$) are shown in the top of Figure 4.12. For this system, the effective forces have almost the same value and remain constant from the second or third oscillation to ~2.5 ns, then the mechanical model proposed using a constant value for these effective forces will be valid for the same period of time. If we divide these forces into a contribution due to the van der Waals attractions and a force that opposes the movement of the nanotube ("friction force"), which will have an opposite sign to the direction of the velocity of the inner nanotube, then we can express $F_I$ and $F_{II}$ as:

$$\begin{aligned}
&I: \quad F_I = F_{VDW} - F_{FR}, && dz/dt > 0, \quad z < 0 \\
&II: \quad F_{II} = -F_{VDW} - F_{FR}, && dz/dt > 0, \quad z > 0 \\
&III: F_{III} = -F_{VDW} + F_{FR} = -F_I, && dz/dt < 0, \quad z > 0 \\
&IV: F_{IV} = F_{VDW} + F_{FR} = -F_{II}, && dz/dt < 0, \quad z < 0
\end{aligned} \tag{4.12}$$

Using equations (4.12) to fit every region of each oscillation, we calculated $F_{VDW}$ and $F_{FR}$ as function of the simulation time and are plotted in the bottom of Figure 4.12. From these plots we can see the so called "Friction force" is very low compared to the van der Waals attractions and that there are other contributions that make the effective forces decrease at the beginning and after 2.5 ns when the amplitude of the oscillations decreases considerably.

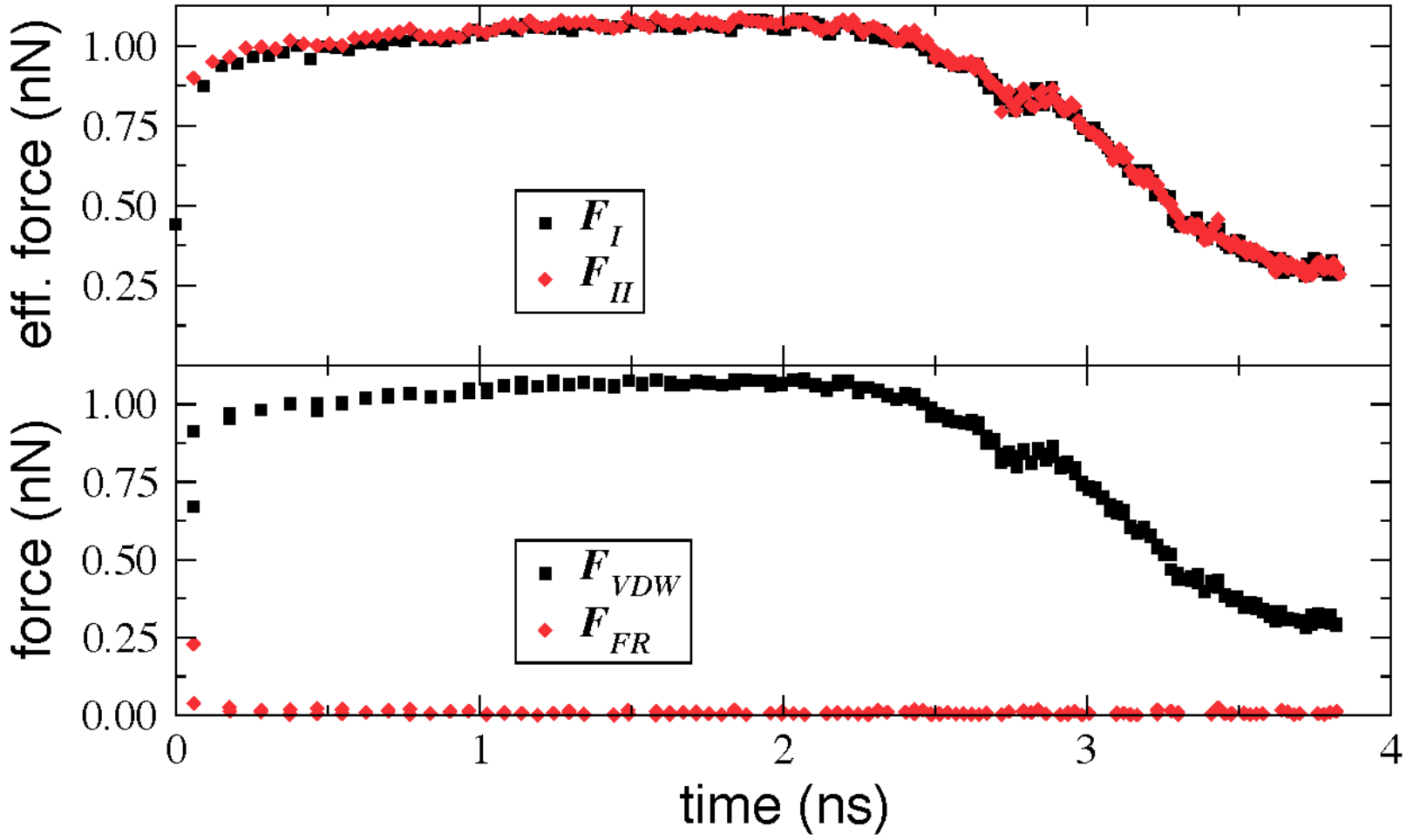


Figure 4.12: Values of the constant effective forces ($F_I$ and $F_{II}$) for the system with chiral conformations (7,0) / (9,9) and length of 24.56 nm (top). Contributions ($F_{VDW}$ and $F_{FR}$) to the constant effective forces (bottom).

Using an averaged value of $F_{VDW}$ and $F_{FR}$ from the bottom of Figure 4.12 in the period of 0.2 to 2.5 ns as an initial estimation, these values were optimized to reproduce the points corresponding to a zero separation for the system with an axial length of 24.56 nm. This procedure produced values of 1.050254 and 0.02438138 nN for the $F_{VDW}$ and $F_{FR}$ respectively. These parameters are highly coupled and changes of either one by as little as 1% can modify the behavior. With these parameters, the damped oscillations were reproduced for the studied systems using equations (4.10 and 4.11). The results of these predictions from the mechanical model for the separation between the centers of mass are shown in Figure 4.13 through 4.15 in red lines, with the black lines corresponding to the simulation results. For the nanotube with axial length of 12.21 nm, the mechanical model reproduces well the profile of the simulations up to ~0.8 ns, and is observed to oscillate with the same amplitude. For the system with 24.56 nm, the model predictions reproduce the behavior up ~1.75 ns; for the systems with 36.92 and 49.27 nm the predictions agree well up to ~2.6 ns, however the model missed two oscillations at ~1.5 and ~2.0 ns for the system with 36.92 nm and one oscillation at ~2.2 ns for the system with 49.27 nm. The regions of mismatch between the simulations and the model for the 36.92 and 49.27 nm, suggest that the frequency of motion being predicted by the model is just slightly off from the measured value. This is not surprising with such a simple model. In Figure 4.15 the predicted results for the system with 98.24 nm are plotted and the long periods needed to decrease the amplitude of the oscillations by ~97%.

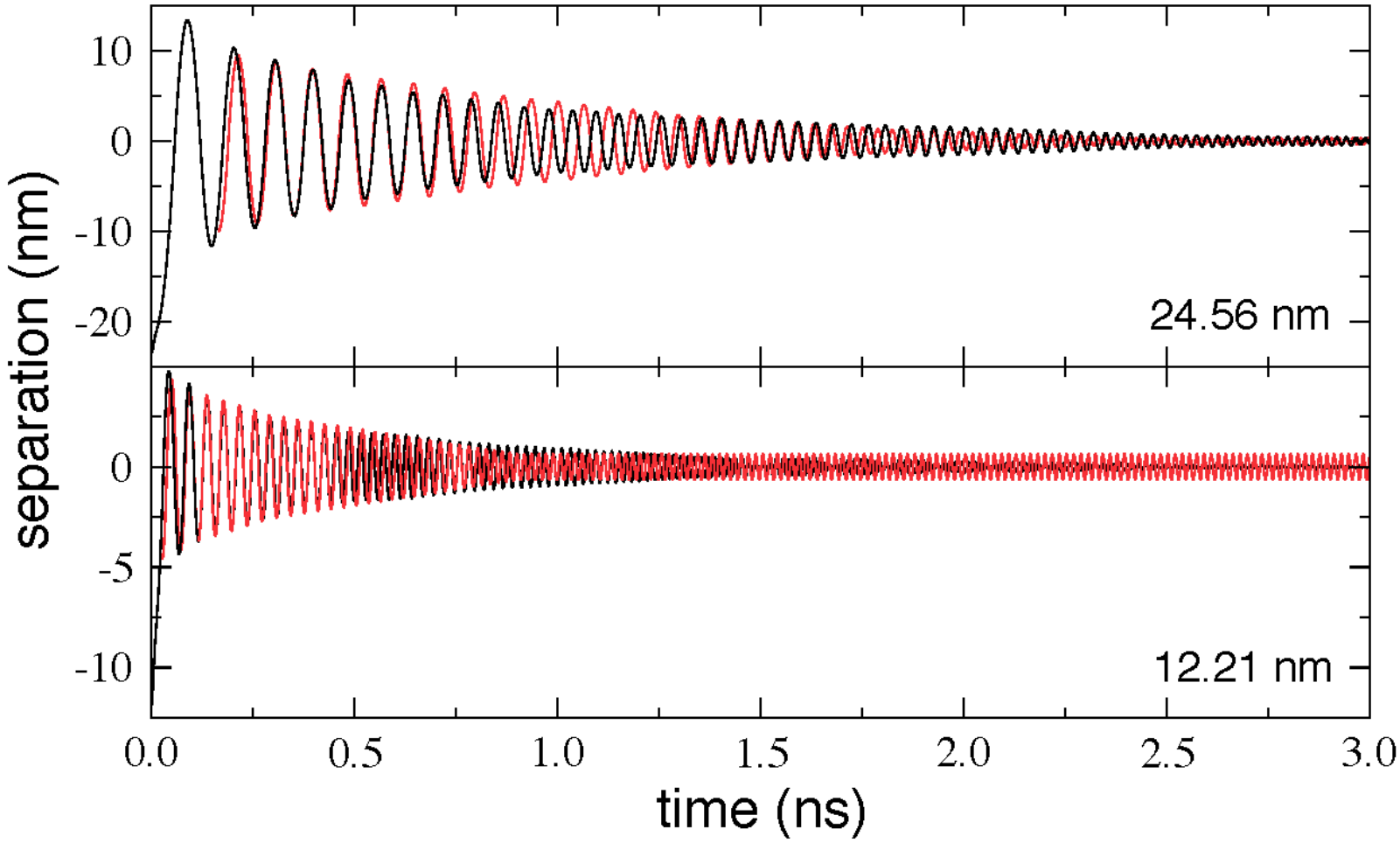


Figure 4.13: Damped oscillations from simulations (black line) and predictions (red line) of the mechanical model with constant effective forces for the system with chiral conformations (7,0) / (9,9).

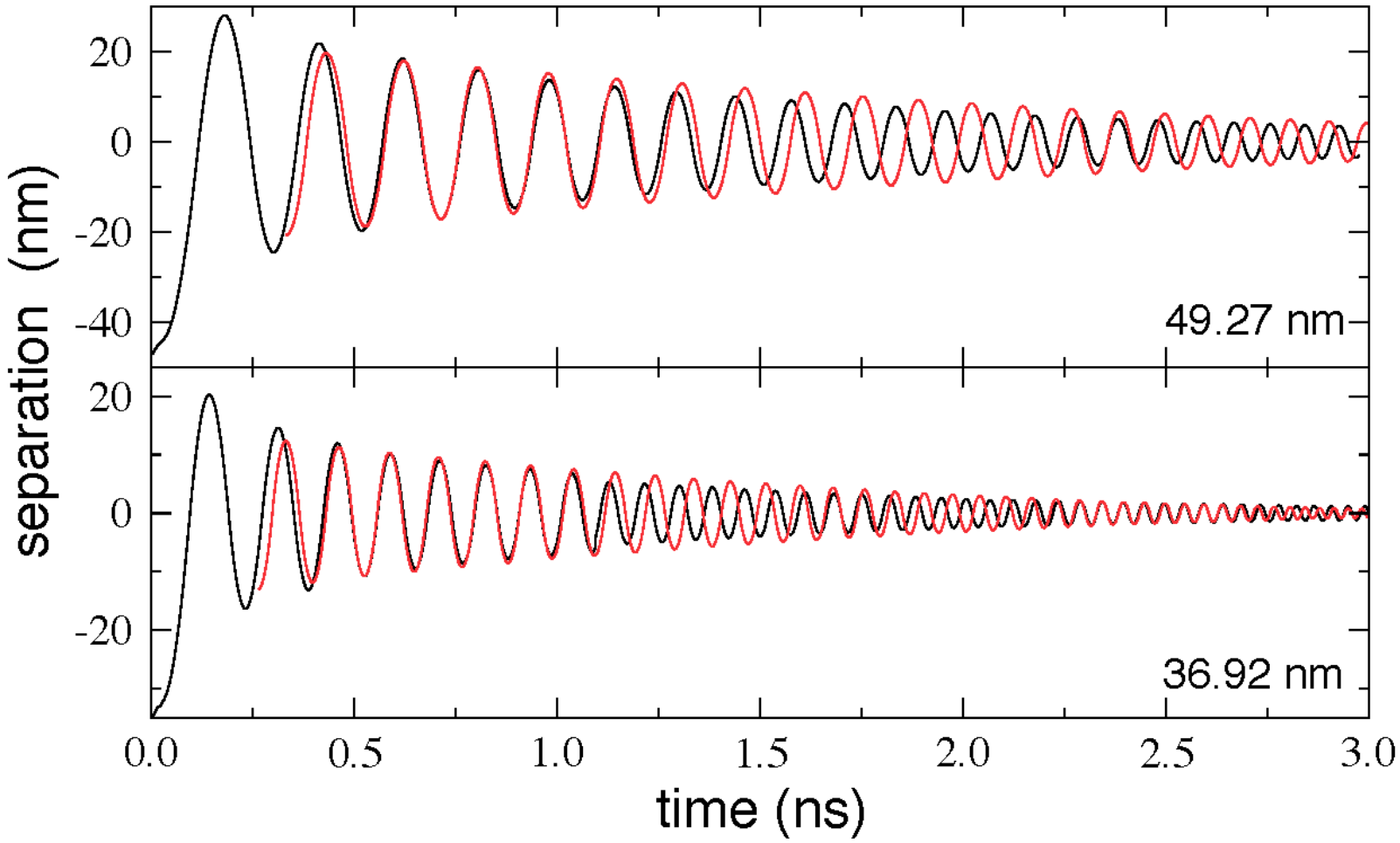


Figure 4.14: Damped oscillations of simulations (black line) and predictions (red line) of the mechanical model with constant effective forces for the system with chiral conformations (7,0) / (9,9)

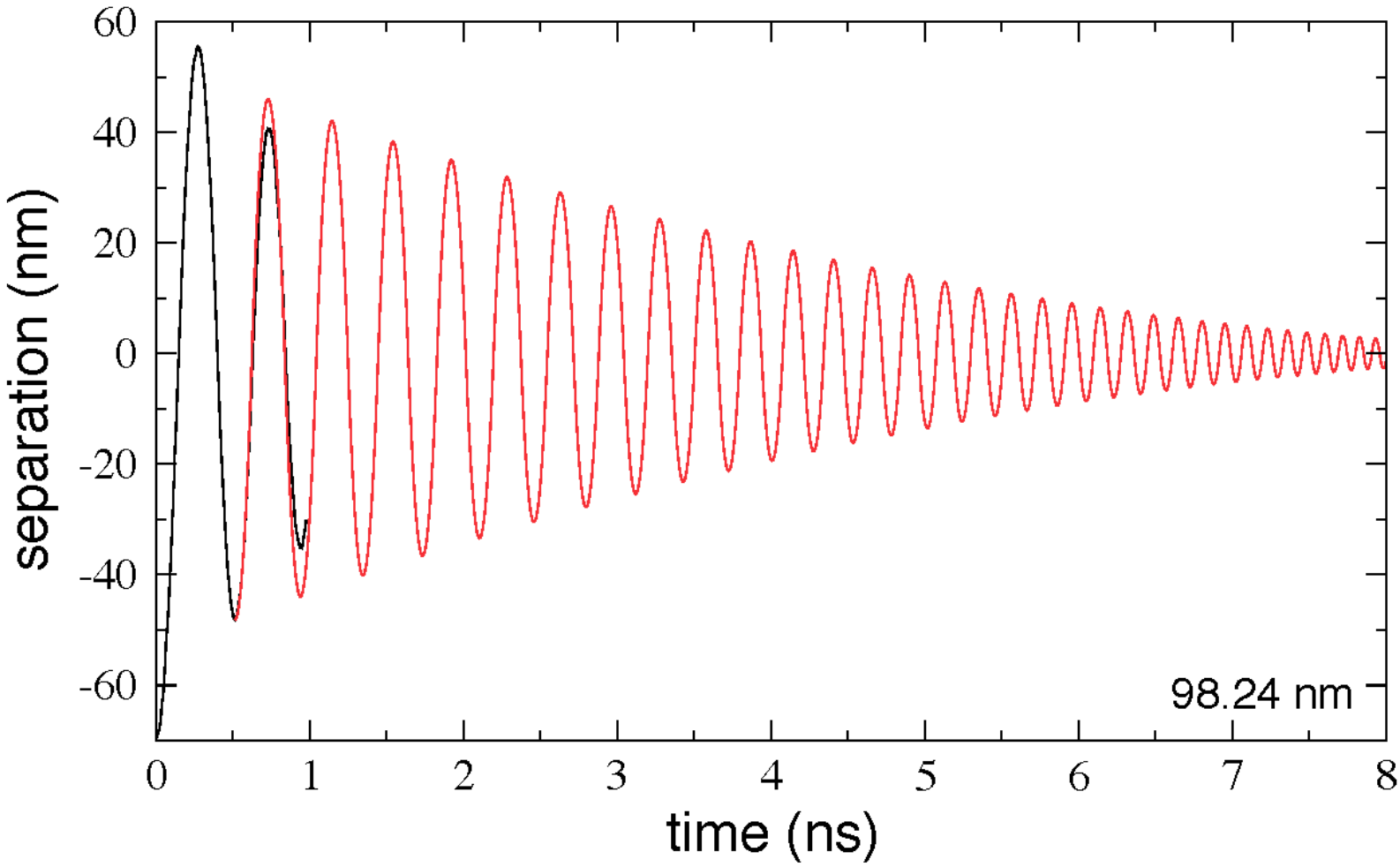


Figure 4.15: Damped oscillations of simulations (black line) and predictions (red line) of the mechanical with constant effective forces for the system with chiral conformations (7,0) / (9,9).

### 4.4.3 Mechanical model with constant effective forces depending on the initial conditions

Snapshots from the simulations showing the early stages of the damped oscillation are presented in Figure 4.16 for the system with an axial length of 12.21 nm. Deformations in the cylinder of the nanotubes are observed for both the inner and outer nanotubes. These deformations make it more difficult for the inner nanotube to enter into the outer nanotube and therefore these forces have opposite sign to the van der Waals interactions and will reduce the absolute value of the effective force. On the other hand, when the nanotube is close to a zero separation, both ends of the inner nanotube are close to their corresponding ends in the outer nanotube and the magnitude of the effective force probably does not change from positive to negative instantaneously, but over some short period of time (or equivalently distance). For this reason after 2.5 ns when the oscillations almost cease, the magnitude of the effective force in Figure 4.12 also starts to decrease. We were not able to produce a profile with the real instantaneous force as a function of the separation that produces a better description of the damped oscillations than in the constant effective forces model. Given the shortcomings of the first model a second model was identified. In the second mechanical model described in this section, the model uses constant effective forces along each region (I, II, III, IV) as in the previous model, but the

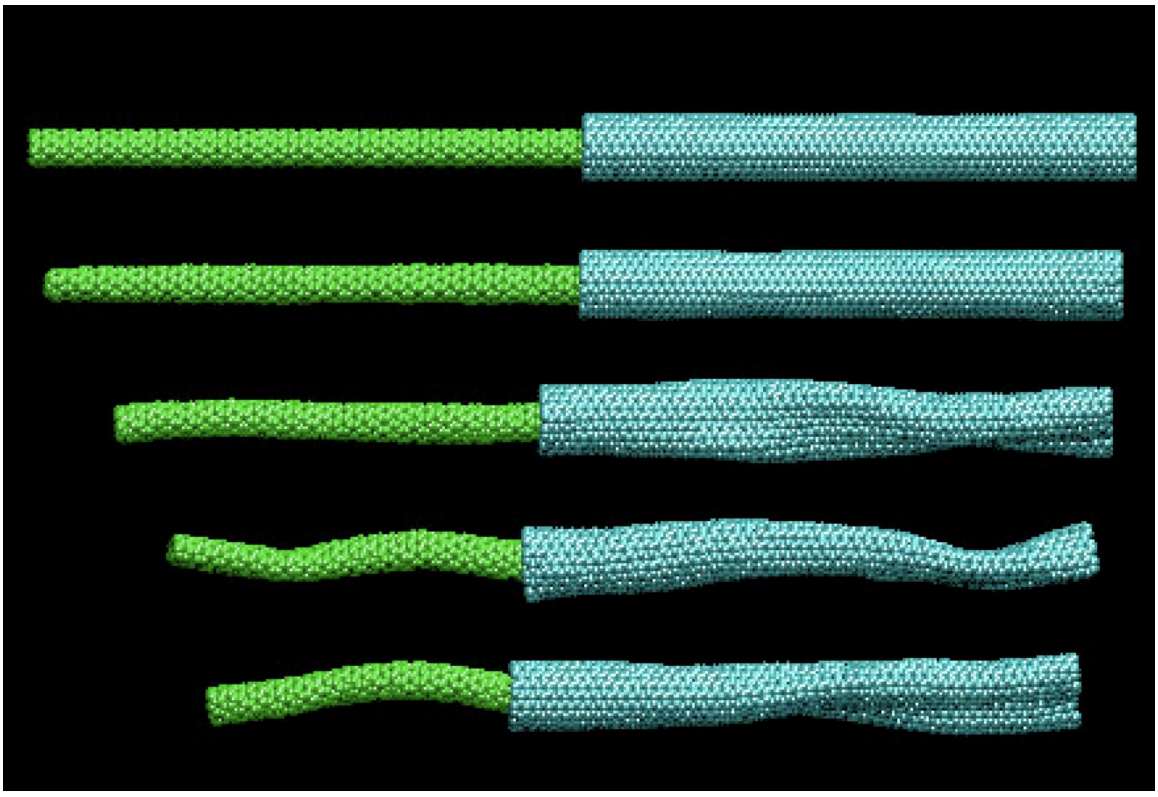

Figure 4.16: Snapshots of the initial oscillation for the system with chiral conformations (7,0) / (9,9), and axial length of 12.21 nm. Deformation in both, inner and outer nanotubes are observed. This deformation forces decrease the effective forces, especially at long initial separations.

value of the constant effective forces depends on the initial separation for regions I, and III, and on the initial velocity for regions II, and IV.

In order to build the second mechanical model that takes into account the deformation forces for longer separations and a better description of the effective forces close to zero separation, the oscillations of all systems were fitted to equations (4.10) and (4.11). The fitted values for the effective forces divided by the mass of the inner nanotube for regions I, and III are plotted in Figure 4.17. The separations plotted in Figure 4.17 are the initial separation for regions I, and III, at the beginning of those regions, or in other words, they are the maximum and minimum separations reached in those regions respectively. Under these terms, the forces do not seem to have any correlation, but as shown in Figure 4.18 they have almost the same profile if only the absolute effective force is plotted and the initial separation is reduced with the axial length of the system. Only the smallest system has a different behavior for initial reduced separations up to 0.15. The points for the rest of the systems seem to lie in the same master profile. In this master profile at the beginning there is a linear increment of the absolute effective force with the initial reduced separation up to a separation of ~0.05. At this point the effective forces have a maximum, and from this point to separations close to 1.0, the effective forces decrease with the reduced separation. From reduced separations of ~0.3 and up, the points showed some dispersion but follow the general tendency to decrease with the reduced

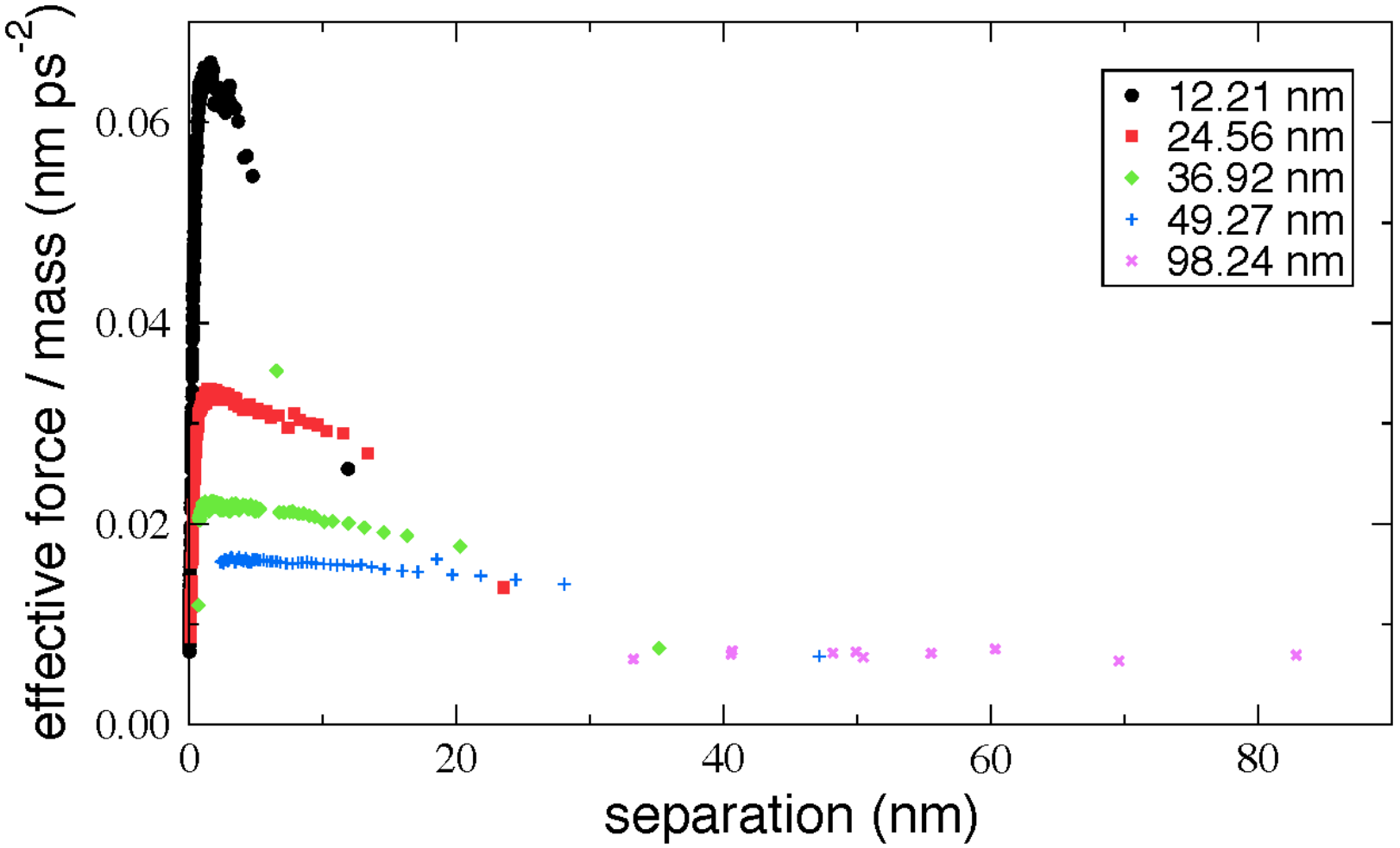


Figure 4.17: Effective forces (I, III) as a function of the initial separation for systems with chiral conformations (7,0) / (9,9) and axial lengths from 12.21 to 98.24 nm.

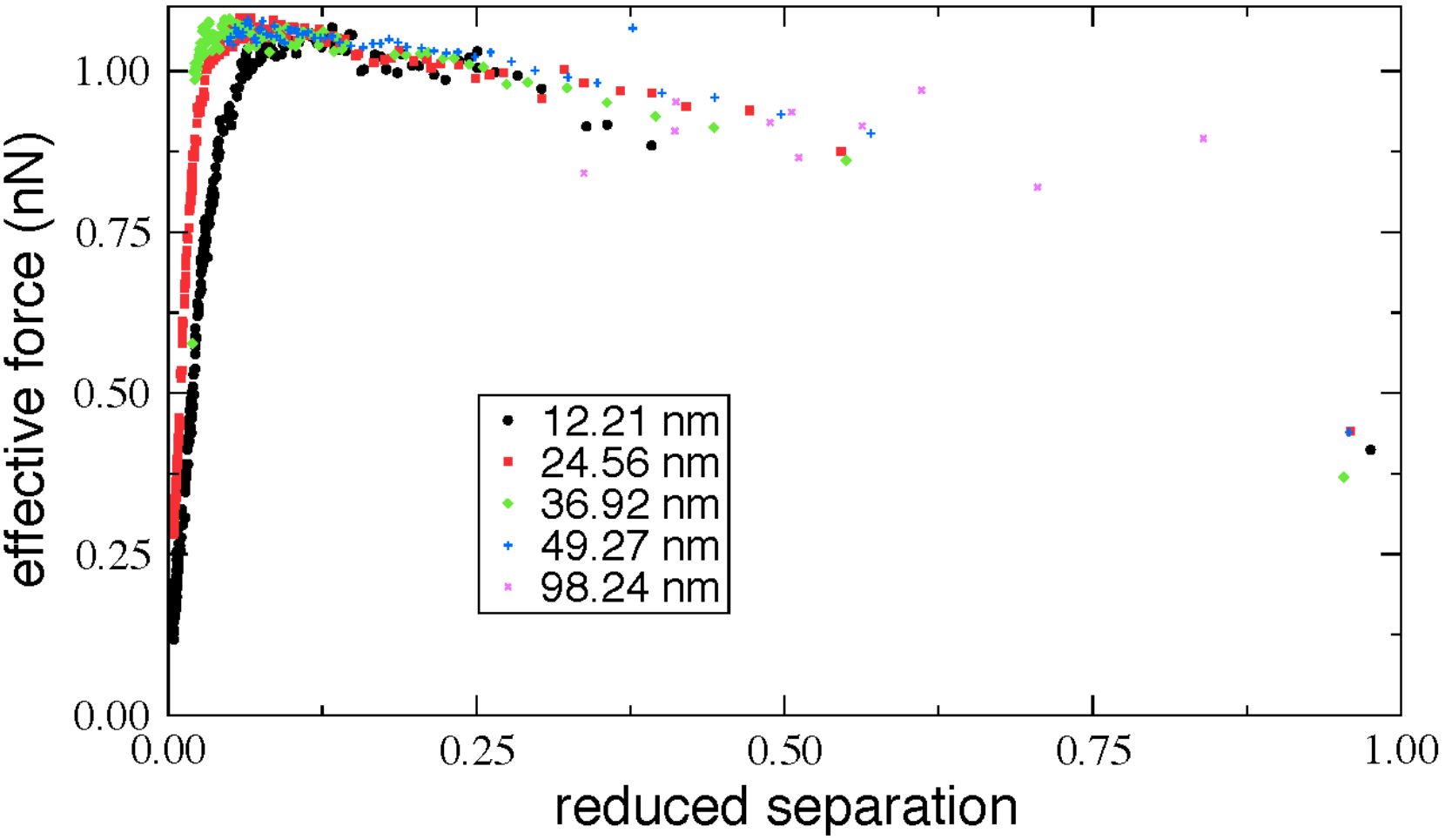


Figure 4.18: Effective forces (I, III) as a function of the initial reduced separation for systems with chiral conformations (7,0) / (9,9) and axial lengths from 12.21 to 98.24 nm.

separation. For regions II and IV, the fitted values to equation (4.11) for the absolute effective forces divided by the mass of the inner nanotube are plotted in Figure 4.19 as function of the initial velocity and only the absolute effective forces are plotted in Figure 4.20. Here it is clear that the smallest system behaves differently from the rest of the systems. These profiles show the same tendency as those for regions I and III, i.e. an initial linear increase at low initial velocities, reaching a maximum from which the absolute effective forces decrease with the initial velocity.

Using only the points of absolute effective forces that correspond to the systems with axial lengths from 24.56 to 98.24 nm, two functions were fitted for the absolute effective forces, one depending on the initial reduced separation (regions I, and III), and one for the absolute forces depending on the initial velocity (regions II, and IV). Those functions are:

$$F_I = A_0 \tanh\left(\frac{z_r}{A_1}\right) - A_2\left(z_r\right)^{A_3} \tag{4.13}$$

$$F_{II} = B_0 \tanh\left(\frac{v_0}{B_1}\right) - B_2\left(v_0\right)^{B_3} \tag{4.14}$$

These functions were first fitted to the points of Figure 4.21 and then optimized to

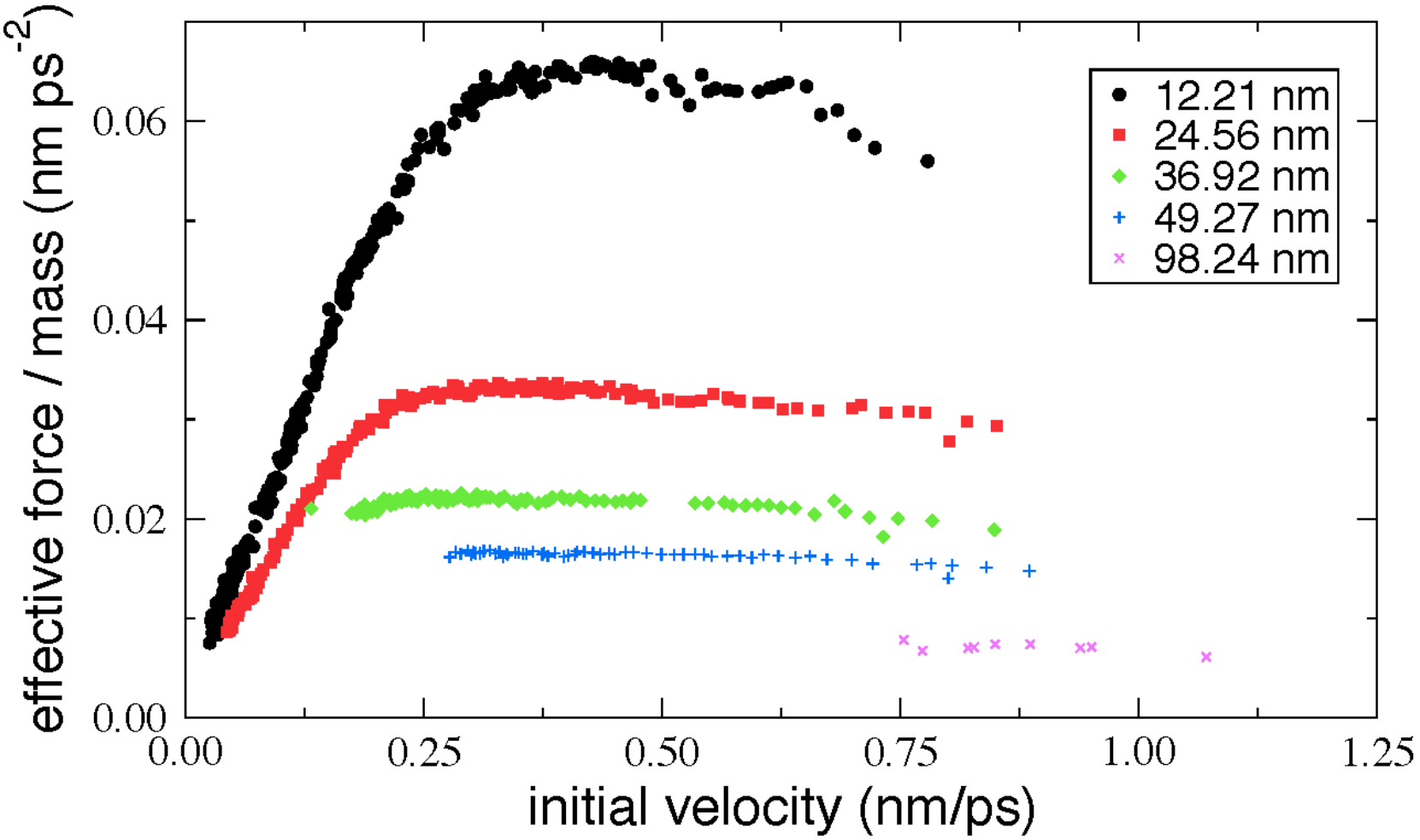


Figure 4.19: Effective forces (II, IV) as a function of the initial velocity for systems with chiral conformations (7,0) / (9,9) and axial lengths from 12.21 to 98.24 nm.

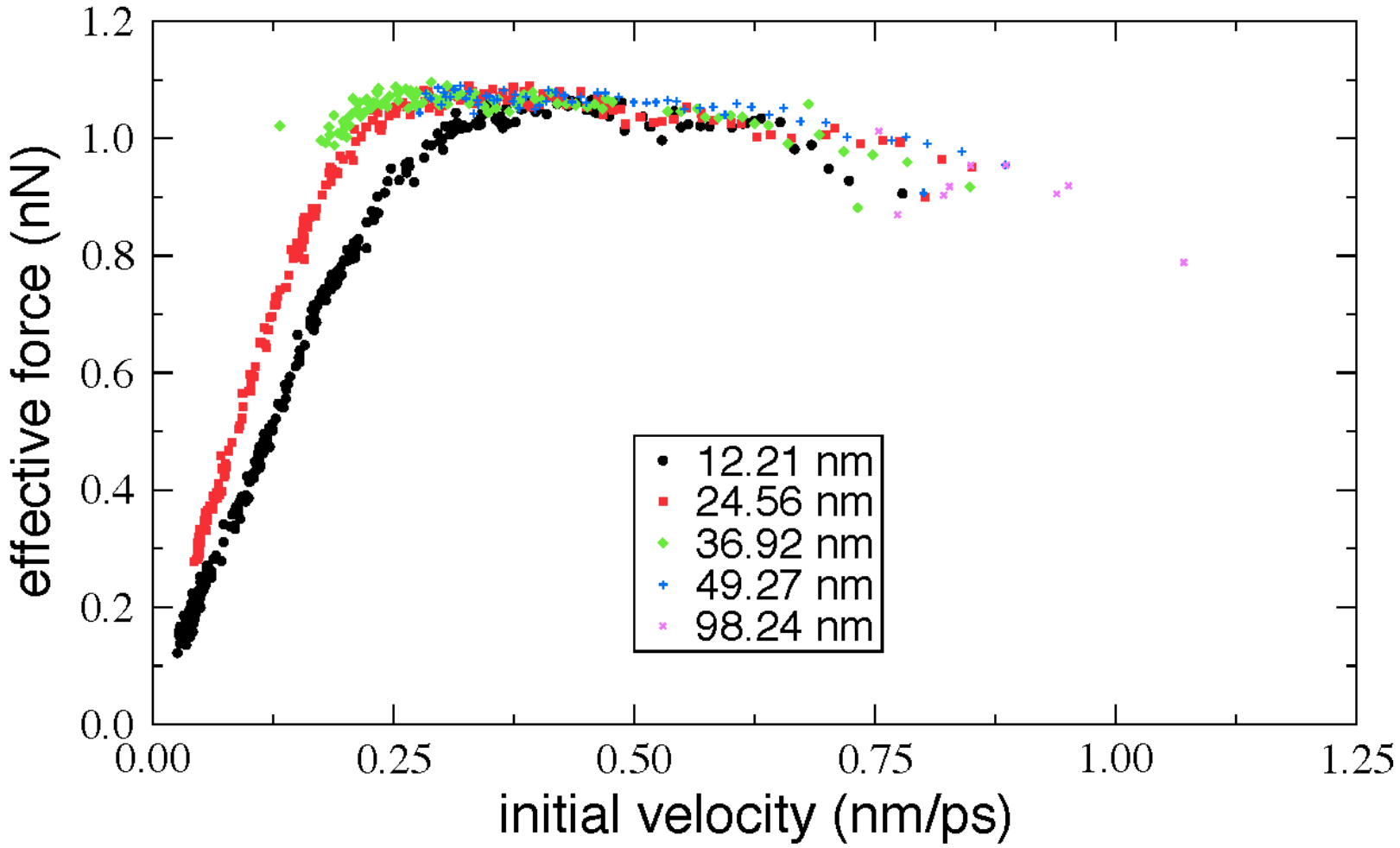


Figure 4.20: Effective forces (II, IV) as a function of the initial velocity for systems with chiral conformations (7,0) / (9,9) and axial lengths from 12.21 to 98.24 nm.

reproduce the zeros of the separation profile for the system with axial length of 24.56 nm. The optimized parameters were: $A_0$ = 1.014281 nN, $A_1$ = 0.037059, $A_2$ = 0.74332 nN, $A_3$ = 1.4107, $B_0$ = 1.6358 nN, $B_1$ = 0.21701 nm/ps, $B_2$ = 0.87821 nN, and $B_3$ = 0.51500. The optimized functions with the used points for the absolute forces are shown in Figure 4.21. The functions fit the values for initial reduced separations up to 0.25 and ~0.30 nm/ps for the initial velocities very well.

Calculating the effective absolute effective forces using functions (4.14) and (4.15), we can reproduce the whole simulation process as shown in Figures 4.22 and 4.20 for the systems with axial lengths from 24.56 to 49.27 nm. The predicted behavior of the mechanical model dependent on the initial conditions is shown in red lines and the simulation results in black lines. The best agreement between the damped oscillations of the simulations and the predicted oscillations by the mechanical model are for times up to 1 ns in the system with axial length of 24.56 nm, while for times after 2.25 ns the best predicted behavior is for the system with axial length of 36.92 nm. For the system with axial length of 24.56 nm, the poor results obtained using this model are probably due to the small disagreement between the optimized curve and the fitted values of $F_{II}$ for initial velocities between 0.3 and 0.6 in the bottom of Figure 4.21.

Using the maximum for the absolute effective force in Figure 4.18 as the dynamic

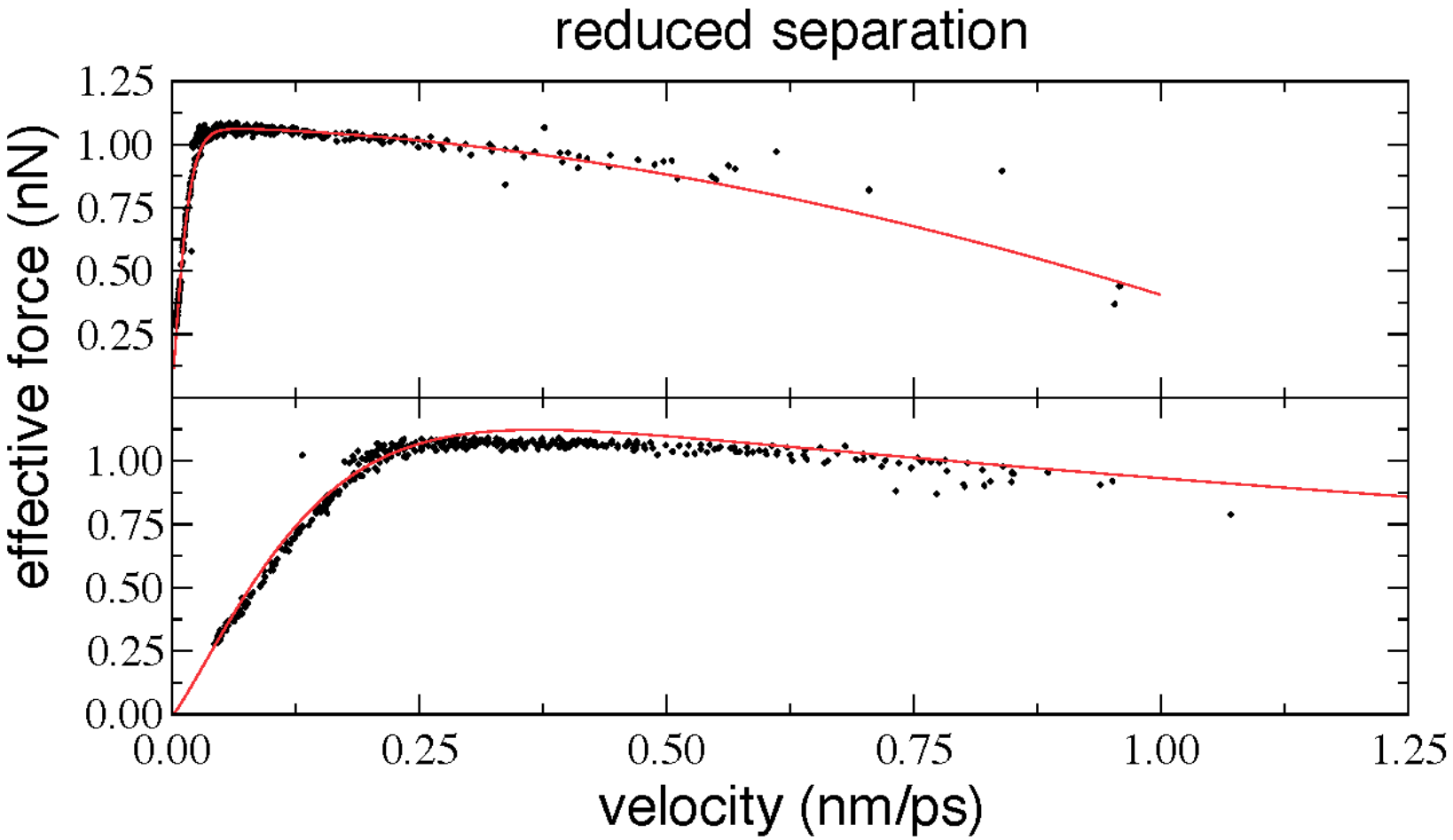


Figure 4.21: Effective forces as function of the reduced initial separation (top) and the initial velocity (bottom) for chiral conformations (7,0) / (9,9) and axial lengths from 24.56 to 98.24 nm. The red lines are the optimized functions to reproduce the behavior of the system with axial length of 24.56 nm.

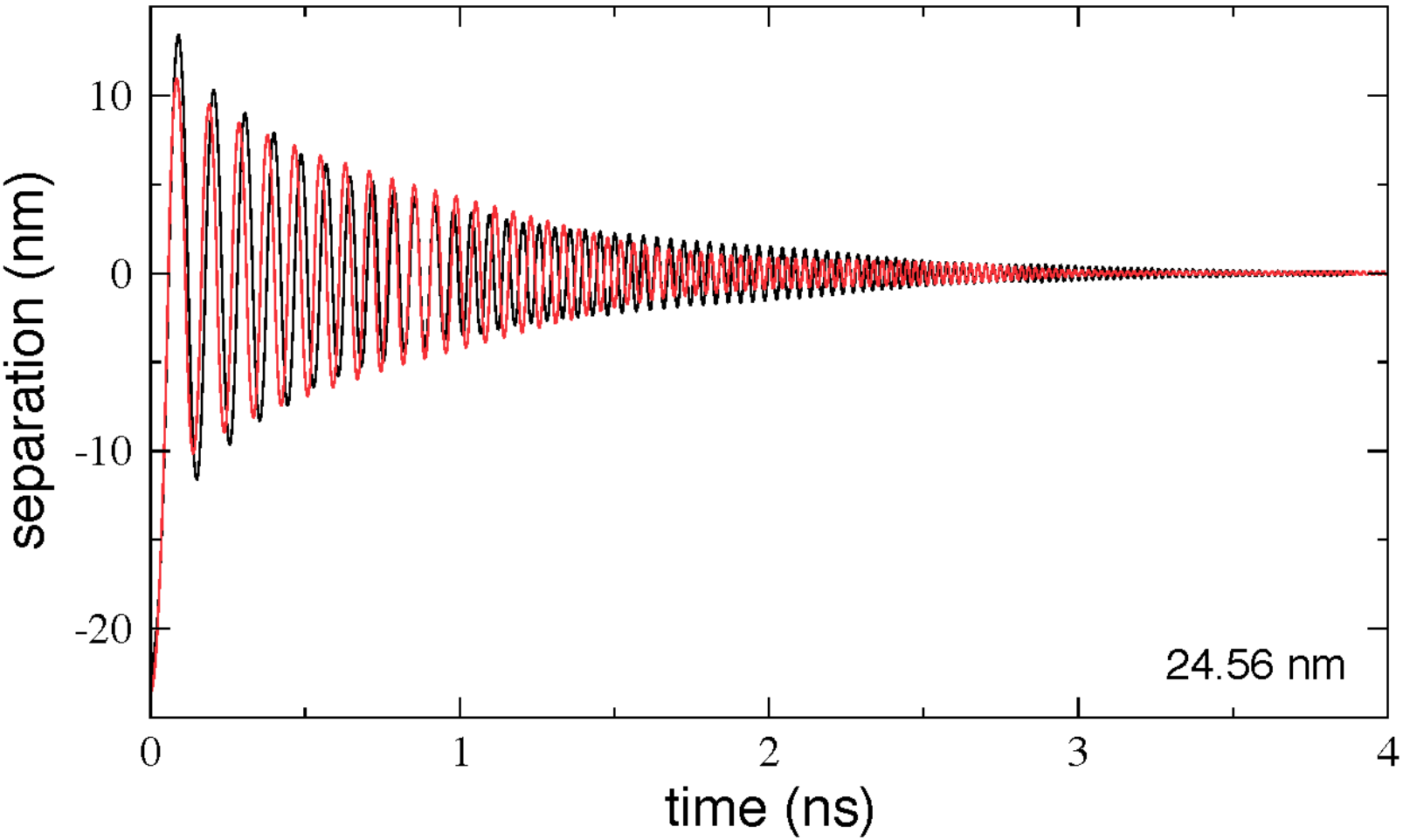


Figure 4.22: Damped oscillations of simulations (black line) and predictions (red line) of the mechanical model with effective forces dependent of the initial conditions. The systems has chiral conformations (7,0) / (9,9).

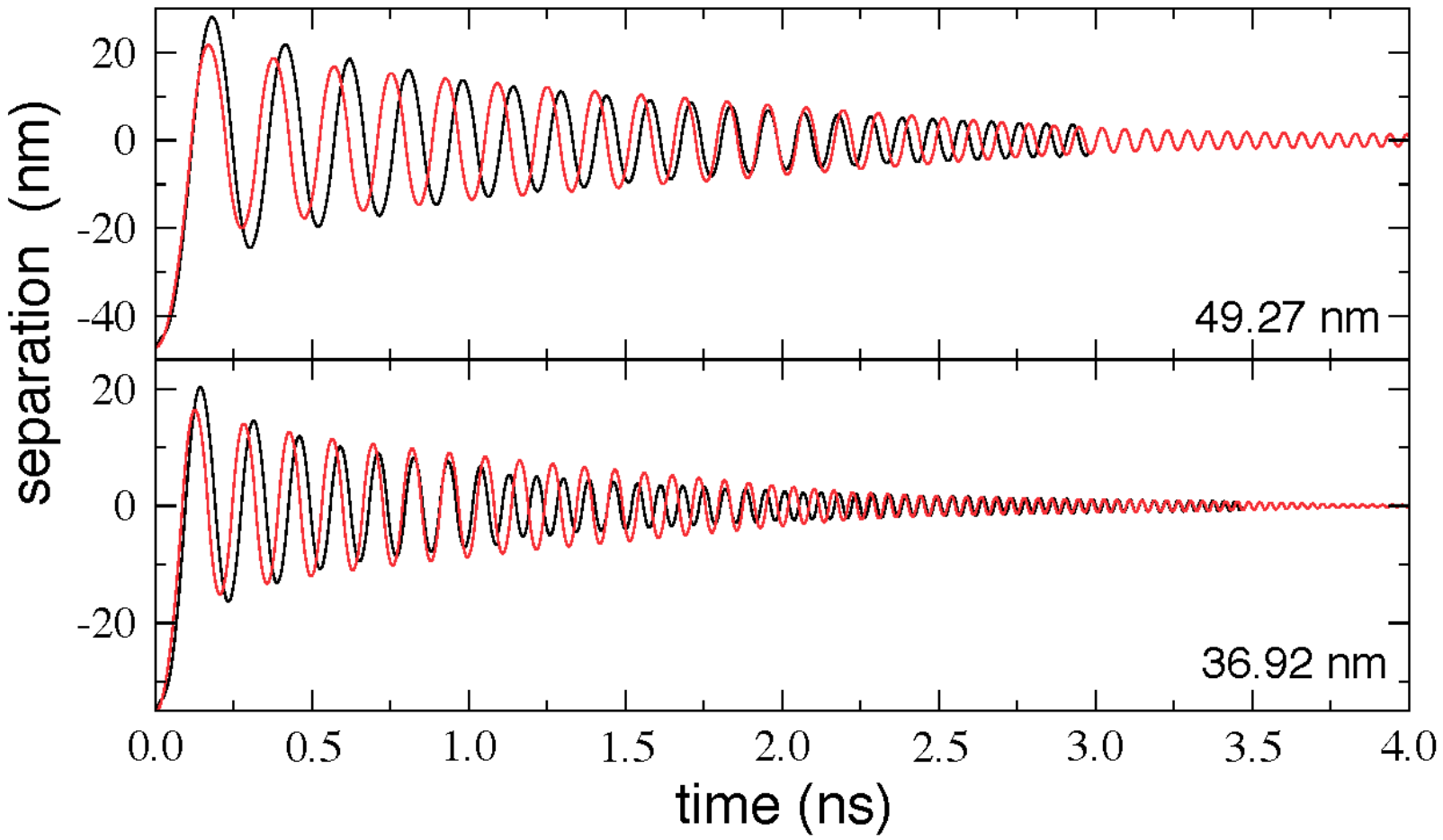


Figure 4.23: Damped oscillations of simulations (black lines) and predictions (red lines) of the mechanical model with effective forces dependent of the initial conditions. The systems have chiral conformations (7,0) / (9,9).

strength force, which is the same for nanotubes with axial length of 24.56 nm and up, we can predict the dynamic strength for these systems. Defining the interfacial area as $2\pi RL_c$, where $R$ is the average radius between the radius of the inner and outer nanotubes radii as shown in Figure 4.24, then we can calculate the dynamic strength, results of these calculations are shown in Figure 4.25 as a red line for systems with axial lengths from 350 to 7000 nm. Experimental estimations for these strengths are shown in black circles for the system of Cumings and Zetl (2000) with 330 nm of axial length (the actual length of the system was not reported, the only length reported was the extrusion length, which is assumed to be close to the axial length of the system) but the diameter was not reported. The results of Yu *et al.* (2000) are also shown at 2200 nm and 7000 nm for system with outer diameters of 30 and 36 nm, respectively. The predicted dynamic strength is proportional to the inverse of the axial length, and the agreement with the largest experimental system is particularly good (absolute difference of ~0.04 MPa). The predicted curve is only for incommensurate nanotubes with an outer diameter of 1.22 nm. Probably for systems with larger outer diameters, there will be four main effects: the increase in the van der Waals interactions due to the larger number of carbon atoms forming the unit cell will increase the shear strength; the larger area will decrease the strength; for wider systems the deformations will be larger and will decrease the dynamic strength. Finally, the fourth effect will be the chiral conformation.

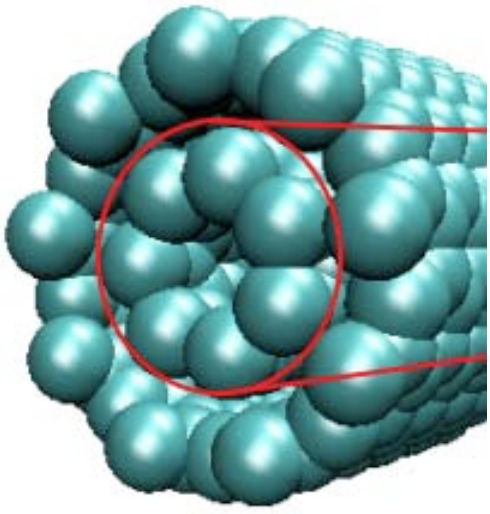

Figure 4.24 Snapshot of the double-wall carbon nanotube and the red cylinder represents the interfacial area between the nanotubes.

How this affects the system is ill-defined (Kolmogorov and Crespi, 2000; Wenning and Muser, 2001).

Using this mechanical model, the time needed to reduce the oscillations to amplitude of less than 4 nm was calculated for systems with axial length up to 1000 nm and the results are reported as black circles in Figure 4.26. The value of 4 nm was chosen because for the system with 1000 nm the normal axial modes of vibration produce vibrations of this magnitude. The red line represents the best fit to a power function, and is given by:

$$time(ns) = \left(0.024176\ ns\ nm^{-1}\right)\left(length(nm)\right)^{1.2} \tag{4.15}$$

Predictions of the profiles for the frequencies as function of the time were produced for four nanotubes between 245 and 982 nm, and the results are shown in Figure 4.27. The profiles were stopped when the amplitude of the oscillations were less than 4 nm as in Figure 4.26. Even though all systems reached frequencies of oscillation above 1 GHz at the end of the process, only the 24.56 nm system exhibits GHz frequencies. As in the previous simulations of shorter systems, the frequencies decrease with the axial length.

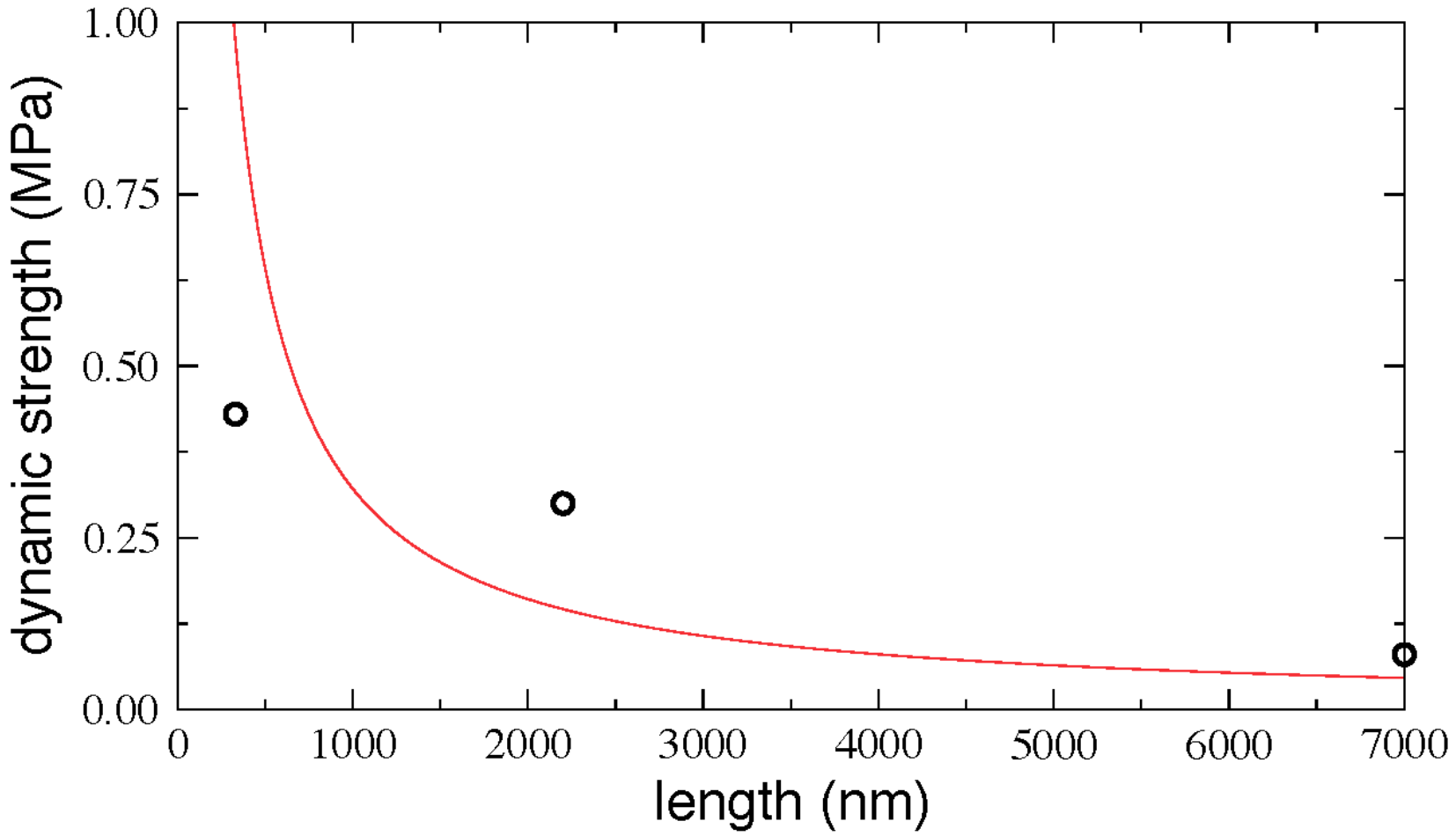


Figure 4.25: Dynamic strength as function of the length for systems with chiral conformations (7,0) / (9,9). Black circles represent the estimated experimental values at 330 nm (Cummings and Zetl, 2000), 2200 and 7000 nm (Yu ***et al.***, 2000).

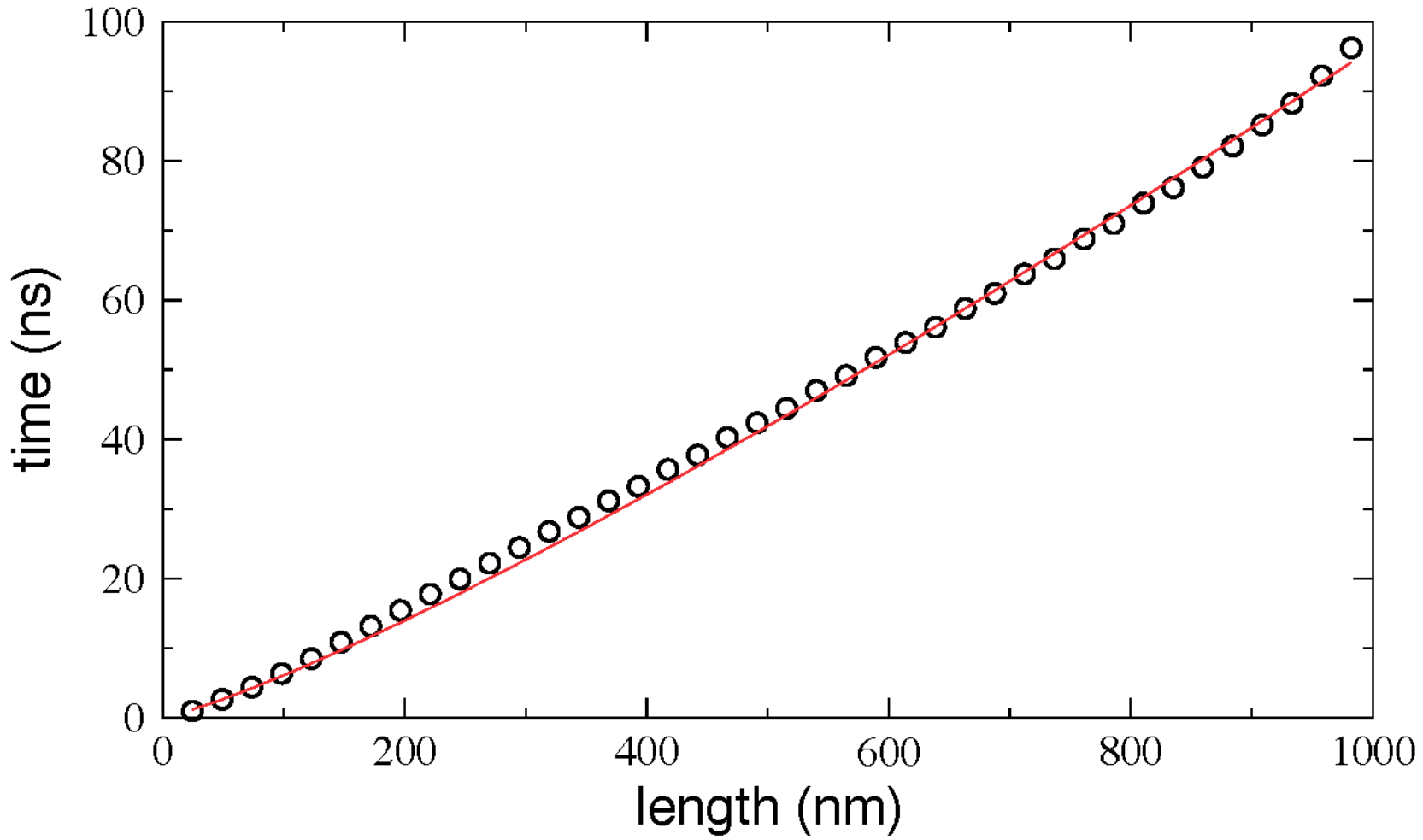


Figure 4.26: Time required to decrease the amplitude of the oscillations to 4 nm as function of the length. The red line represents the fitted function to a power of the length.

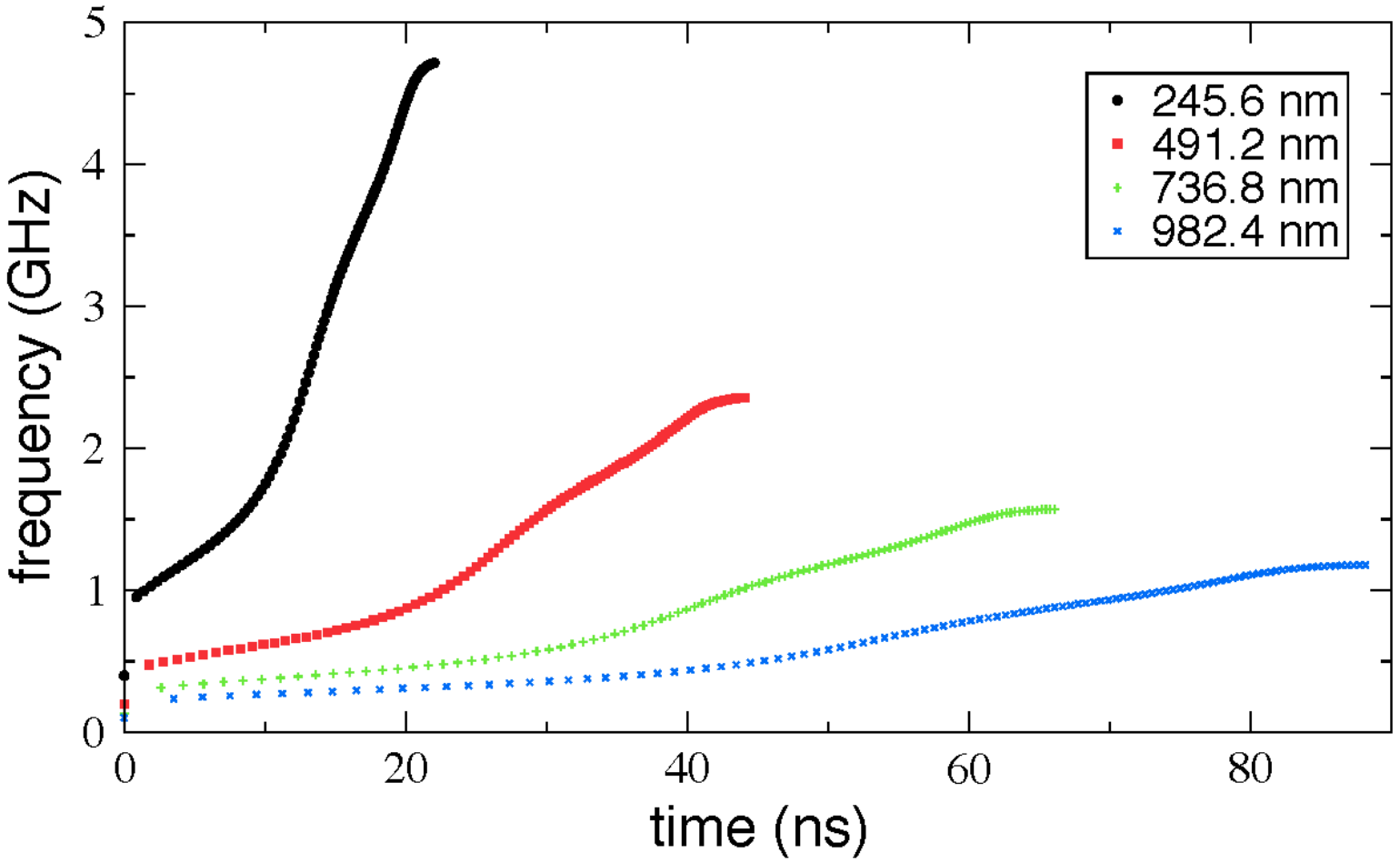


Figure 4.27: Predicted frequency profiles as function of time for systems with chiral conformations (7,0) / (9,9) and axial lengths from 245.6 to 982.4 nm.

### 4.4.4 The incommensurate system (7,0)/(9,9) with unequal axial lengths

The effect of different axial lengths was studied using an inner nanotube with axial length of 12.21 nm and seven different systems where the axial length of the outer nanotube changed from –30 % to +40% as depicted in the snapshots of Figure 4.28. Results with the damped oscillation profiles are shown in Figure 4.29 for the shorter outer nanotubes and in Figure 4.30 for the larger outer nanotubes. The case (o1) depicted in Figure 4.29 showed that by reducing the length of the outer nanotube by 10 %, we obtain initially faster equilibrations, but the nanotube never finishes the damped oscillations because the center of mass of the inner nanotube is moving between both ends of the outer nanotube. This phenomena is clearer for cases (o2) and (o3) where the outer nanotube is 20 and 30 % shorter respectively. Using larger outer nanotubes we can also obtain very fast equilibrations as in the case (o4) where after ~0.5 ns the damped oscillations have almost completely ceased, but the oscillations never passed an amplitude of 2 nm. If the axial length of the outer nanotube is increased by 20 % then it takes ~ 1 ns for the well-defined damped oscillations to finish, while for the systems with 30 % and 40 % larger outer nanotubes, it takes ~ 0.75 ns to finish. Beyond these times, we observe erratic behavior, which probably reflects large thermal fluctuations.

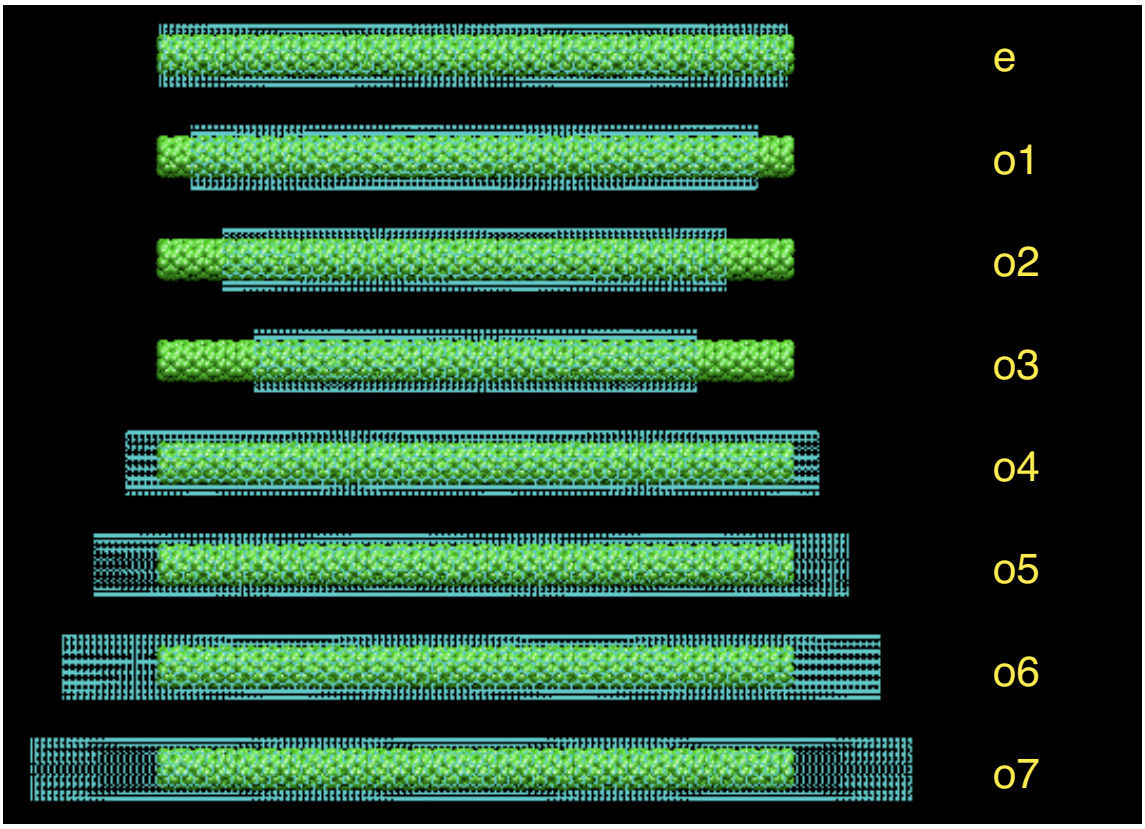


Figure 4.28: Snapshots of the equilibrated systems with chiral conformations (7,0) / (9,9) and e) even axial lengths (12.21 nm), o1) outer nanotube 10 % shorter, o2) 20 %, o3) 30 %, o4) 10 % larger, o5) 20 %, o6) 30 %, and o7) 40 %.

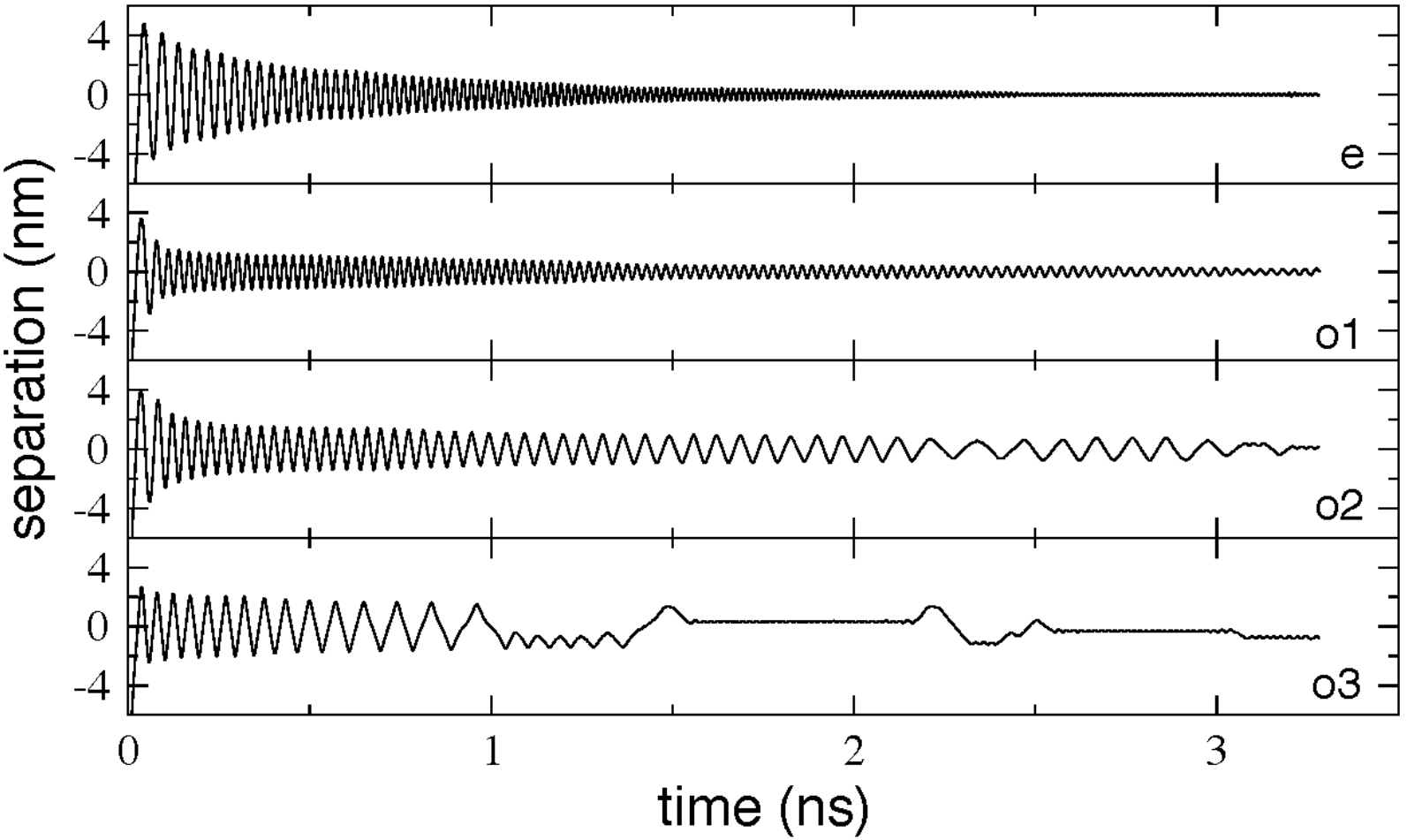


Figure 4.29: Separation of the centers of mass as a function of time for the system with chiral conformations (7,0) / (9,9) and e) even axial lengths, o1) outer nanotube 10% shorter, o2) 20%, and o3) 30%.

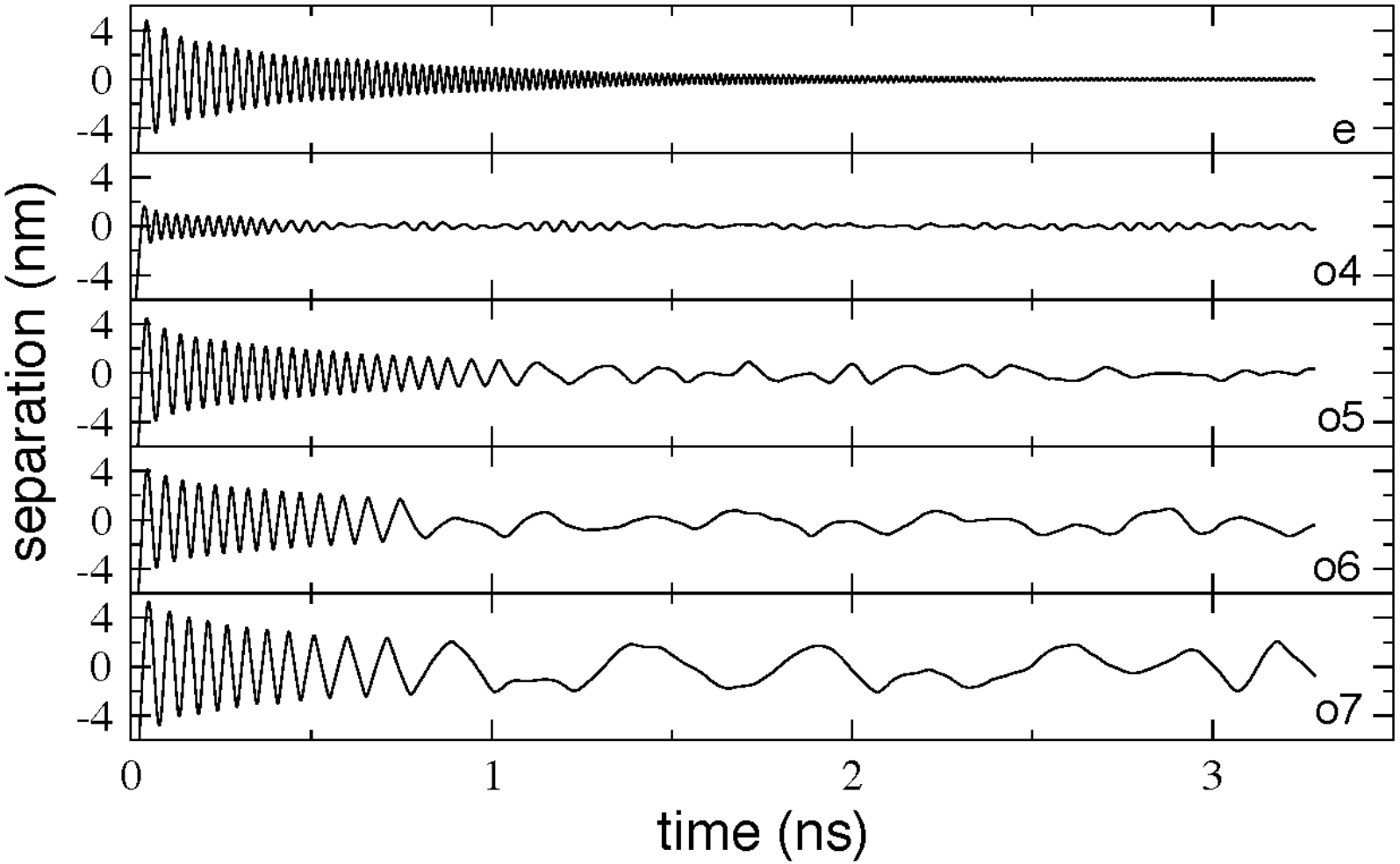


Figure 4.30: Separation of the centers of mass as a function of time for the system with chiral conformations (7,0) / (9,9) and e) even axial lengths, o4) outer nanotube 10% larger, o5) 20 %, o6) 30 %, and o7) 40 %

The frequencies of oscillation were calculated for all cases and appear in the top of Figure 4.31 for the systems with shorter outer nanotubes and in the bottom of the figure for the systems with larger outer nanotubes. The case where both lengths are the same is used as a reference case and it is plotted in both Figures for comparison. Compared to the reference case, shorter outer nanotubes have bigger frequencies at the beginning of the motion, but then they reach a maximum and start to decrease. The rate of decrease is faster for the shortest outer nanotube. For the case (o4) with a outer nanotube that is 10% larger in axial length than the inner nanotube, the frequencies are higher than the reference case, but for case (o5) through (o7) they are generally lower and the well-defined damped oscillations last for less than 1 ns.

The absolute effective forces were calculated for all these cases and appear in Figure 4.32 for $F_I$, and $F_{II}$ is plotted in Figure 4.33. In general we can see a movement of the forces profiles to the right reflecting the differences between the axial lengths of the inner and outer nanotubes. There is also a decrease in the magnitude of the absolute axial forces no matter if the outer nanotube is shorter or larger, the maximum absolute attractive force is reached when both nanotubes has the same axial length. The case (o4) with 10 % larger outer system is very interesting, because the maximum absolute effective force $F_I$ decreases by ~25 %, but for the next system (20 % larger) this force increases again by ~17% and from there continues to decrease regularly.

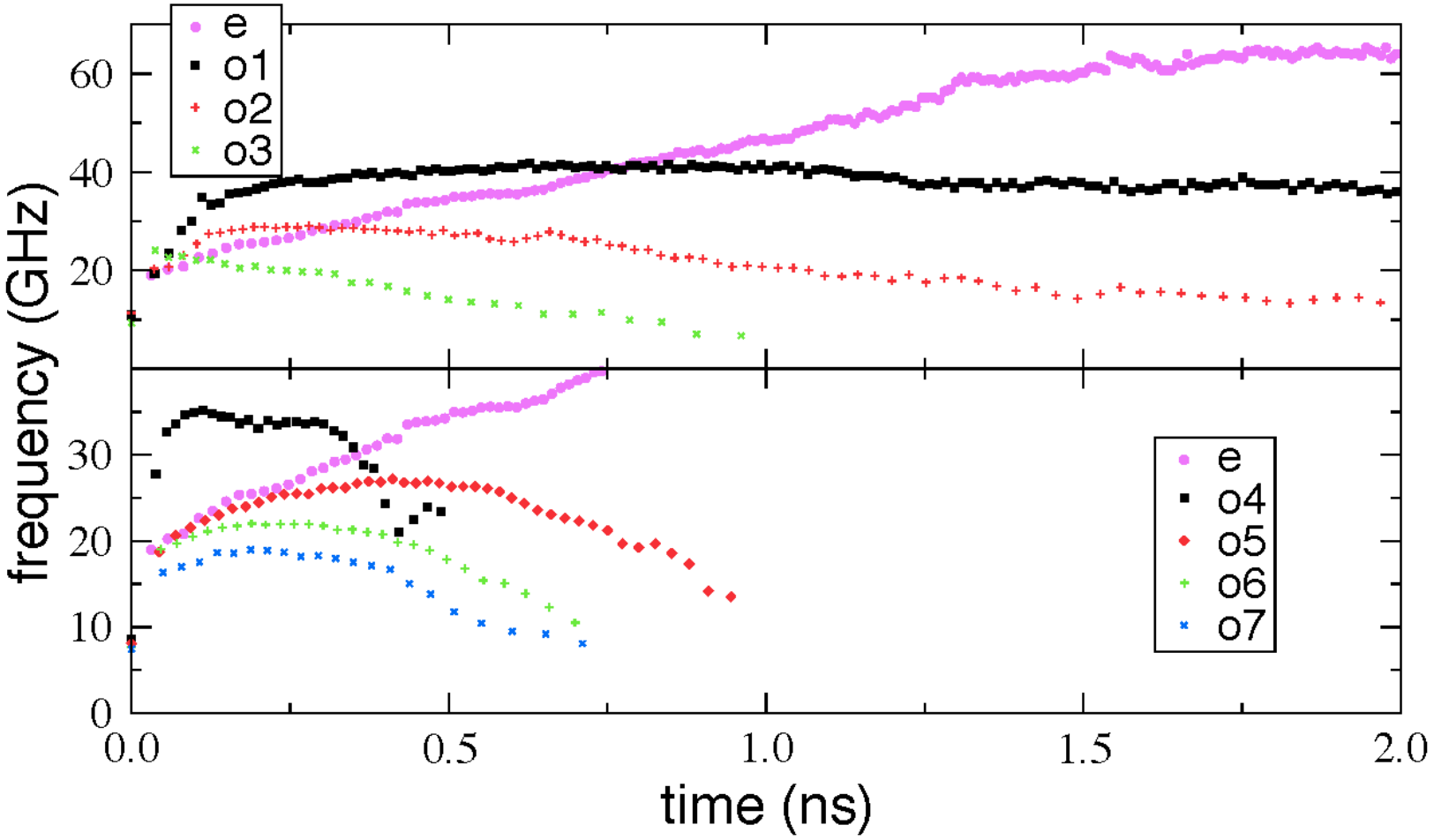


Figure 4.31: Frequency of the damped oscillations as a function of time for systems with chiral conformations (7,0)/(9,9) and e) even axial lengths, o1) outer nanotube 10 % shorter, o2) 20 %, o3) 30 %, o4) outer nanotube 10 % larger, o5) 20 %, o6) 30 %, and o7) 40 %.

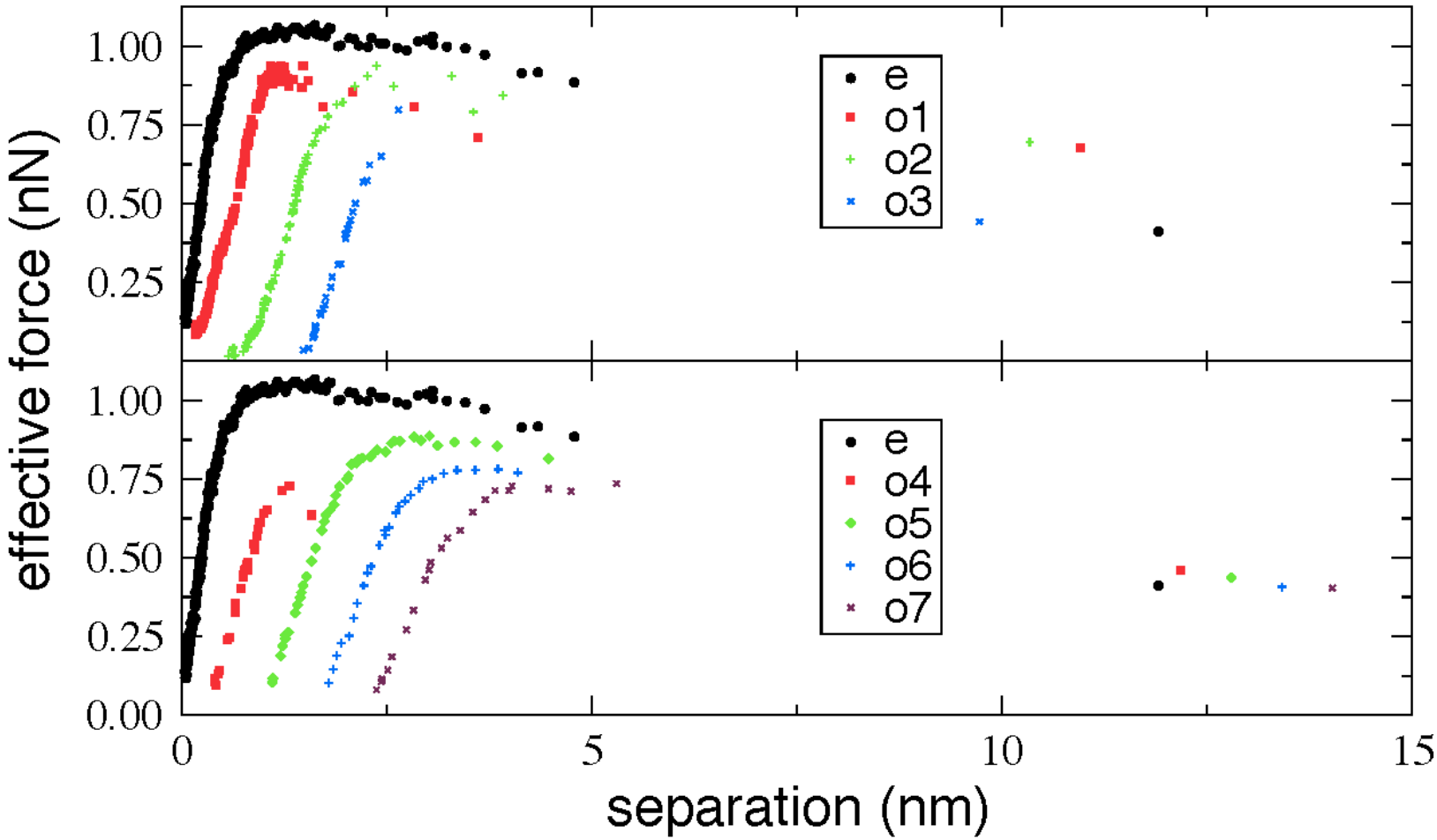


Figure 4.32: Effective forces (I, III) as a function of the intial separation for systems with chiral conformations (7,0)/(9,9) and e) even axial lengths, o1) outer nanotube 10 % shorter, o2) 20 %, o3) 30 %, o4) outer nanotube 10 % larger, o5) 20 %, o6) 30 %, and o7) 40 %.

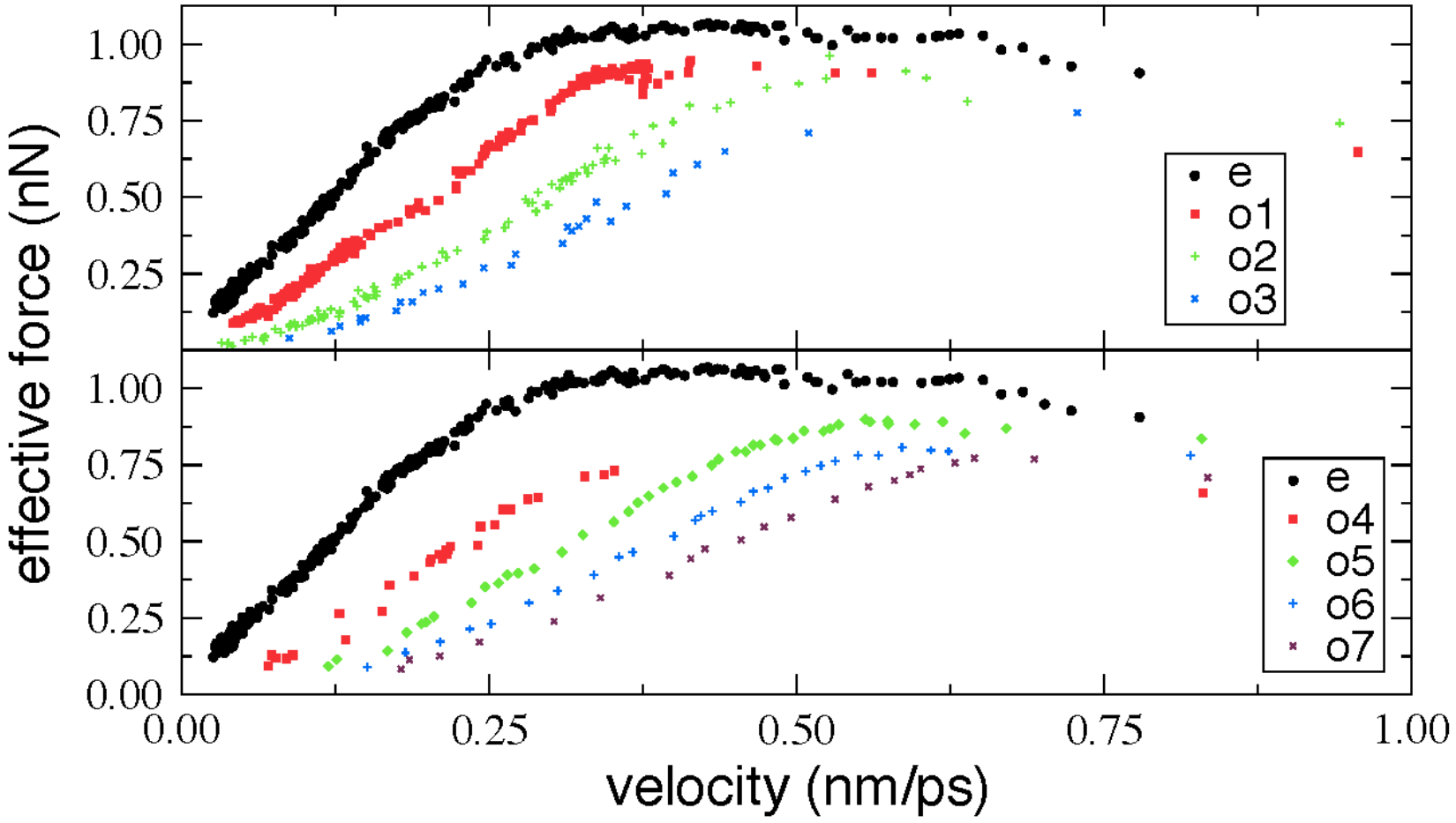


Figure 4.33: Effective forces (II, IV) as a function of the initial velocity for systems with chiral conformations (7,0)/(9,9) and e) even axial lengths, o1) outer nanotube 10 % shorter, o2) 20 %, o3) 30 %, o4) outer nanotube 10 % larger, o5) 20 %, o6) 30 %, and o7) 40 %.

### 4.4.5 The effect of temperature

The effect of temperature was studied in the system with axial length of 12.21 nm. The studied temperatures were 275, 298.15, 325, 350, 375, 400, and 450 K. The damped oscillations of the separation between the center of mass are shown in Figure 4.34 for five of these temperatures. In general we can see a faster equilibration of the systems with increasing temperature probably because the carbon atoms move faster, making the equilibration process faster also. This can be seen again in Figure 4.35 where the time required to decrease the amplitude of the oscillations to less than 0.4 nm is plotted against the temperature of the simulation. This criteria (0.4 nm) is smaller than that used previously (4 nm) because of the short length (12.21 nm) of the nanotube studied here. In general the time decreases with the temperature, but the behavior is not well defined. Changing the temperature by 175 K starting at 275 K, decreases the time by ~1 ns.

In terms of the frequencies of oscillation, there is not much difference between the profiles shown in Figure 4.36, except that at 450 K the frequencies are higher at the beginning with differences as high as 15 GHz after 0.75 ns of simulation. As expected, there are no changes in terms of the absolute effective forces as shown in Figure 4.37, because the forces do not depend on the simulated temperatures.

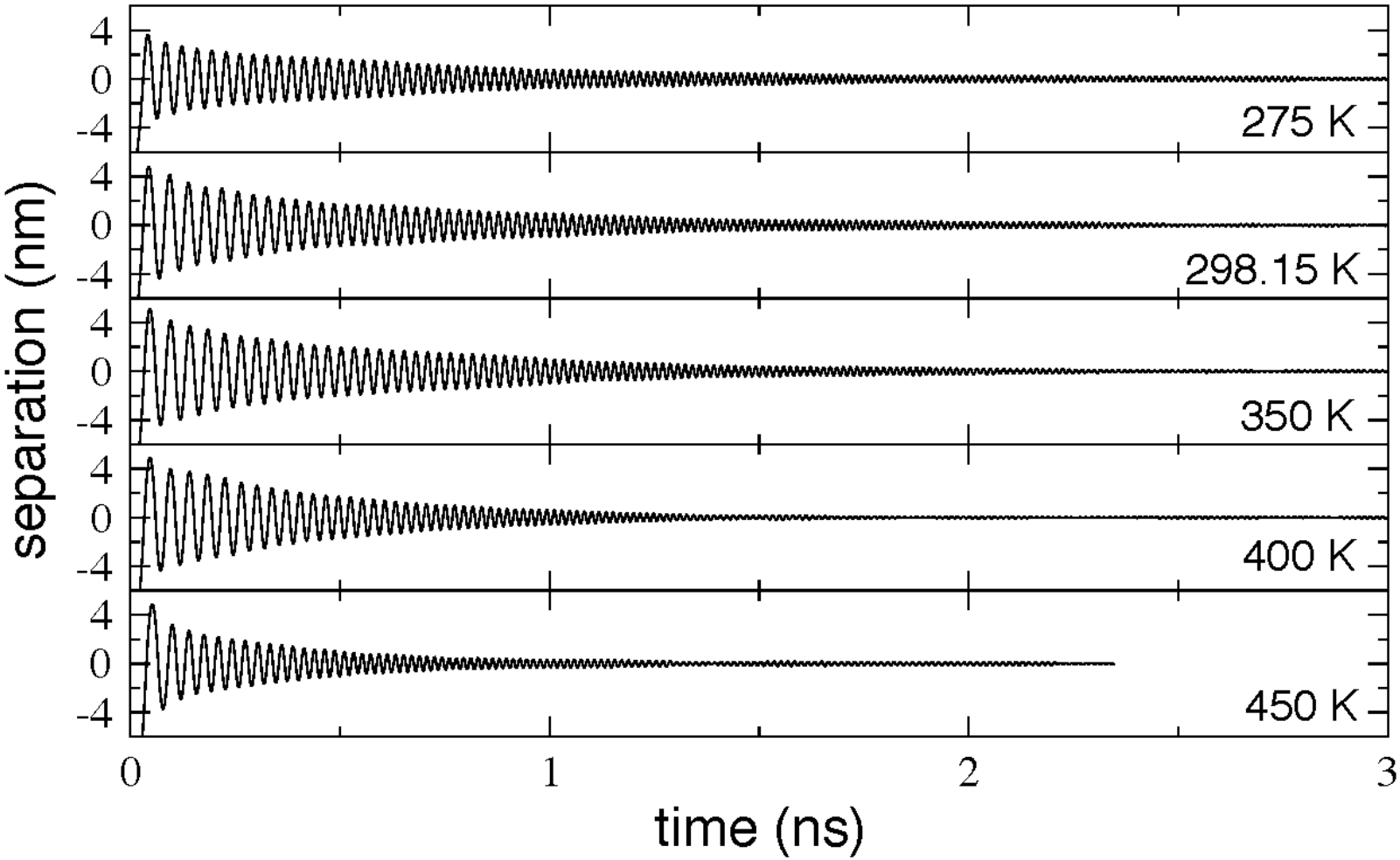


Figure 4.34: Separation of the center of mass as function of the time for systems with chiral conformations (7,0) / (9,9), axial length of 12.21 nm, and temperatures from 275 to 450 K.

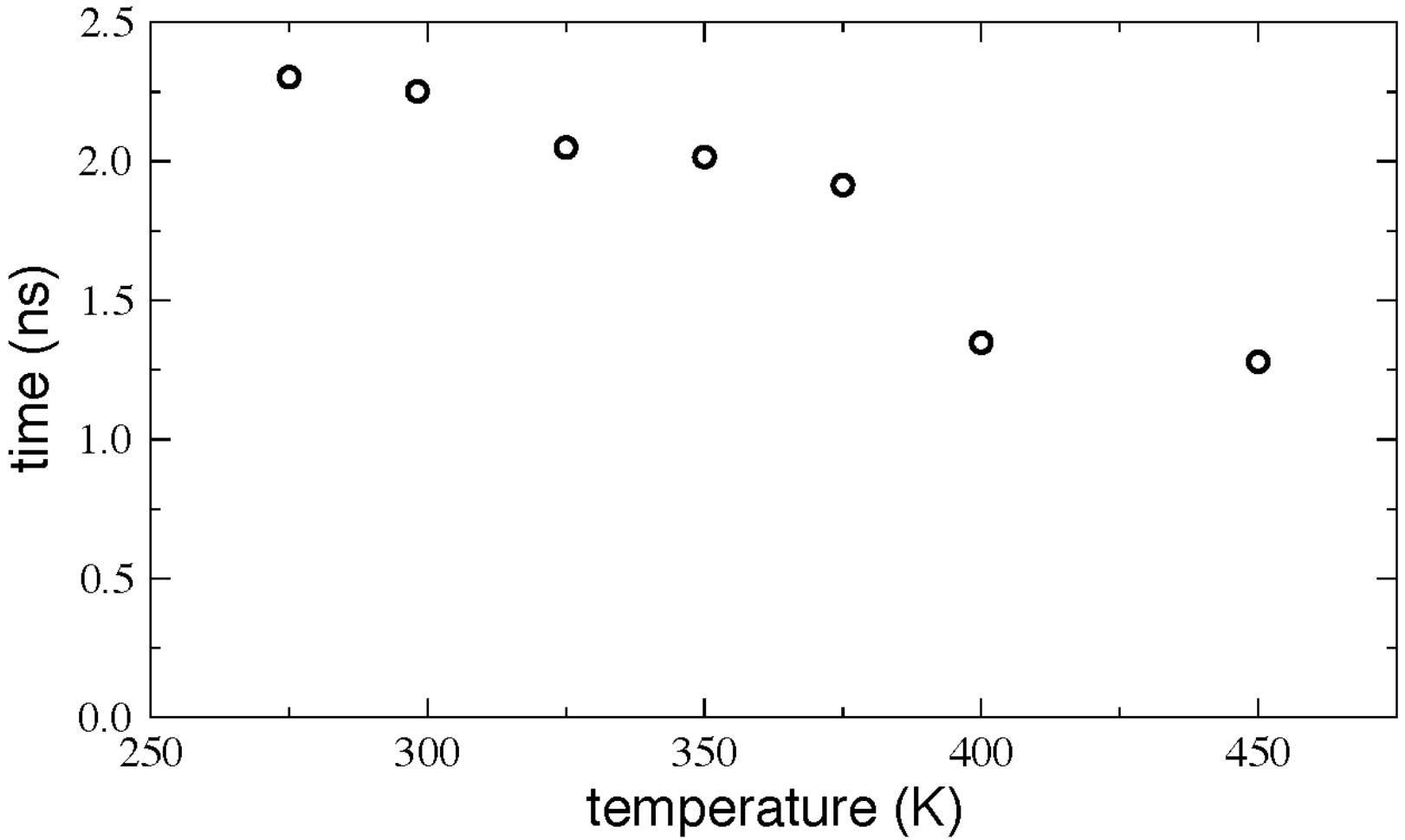


Figure 4.35: Time required to decrease the amplitude of the oscillation to 0.4 nm as function of the temperaute. The systems have chiral conformations of (7,0) / (9,9) and axial length of 12.21 nm.

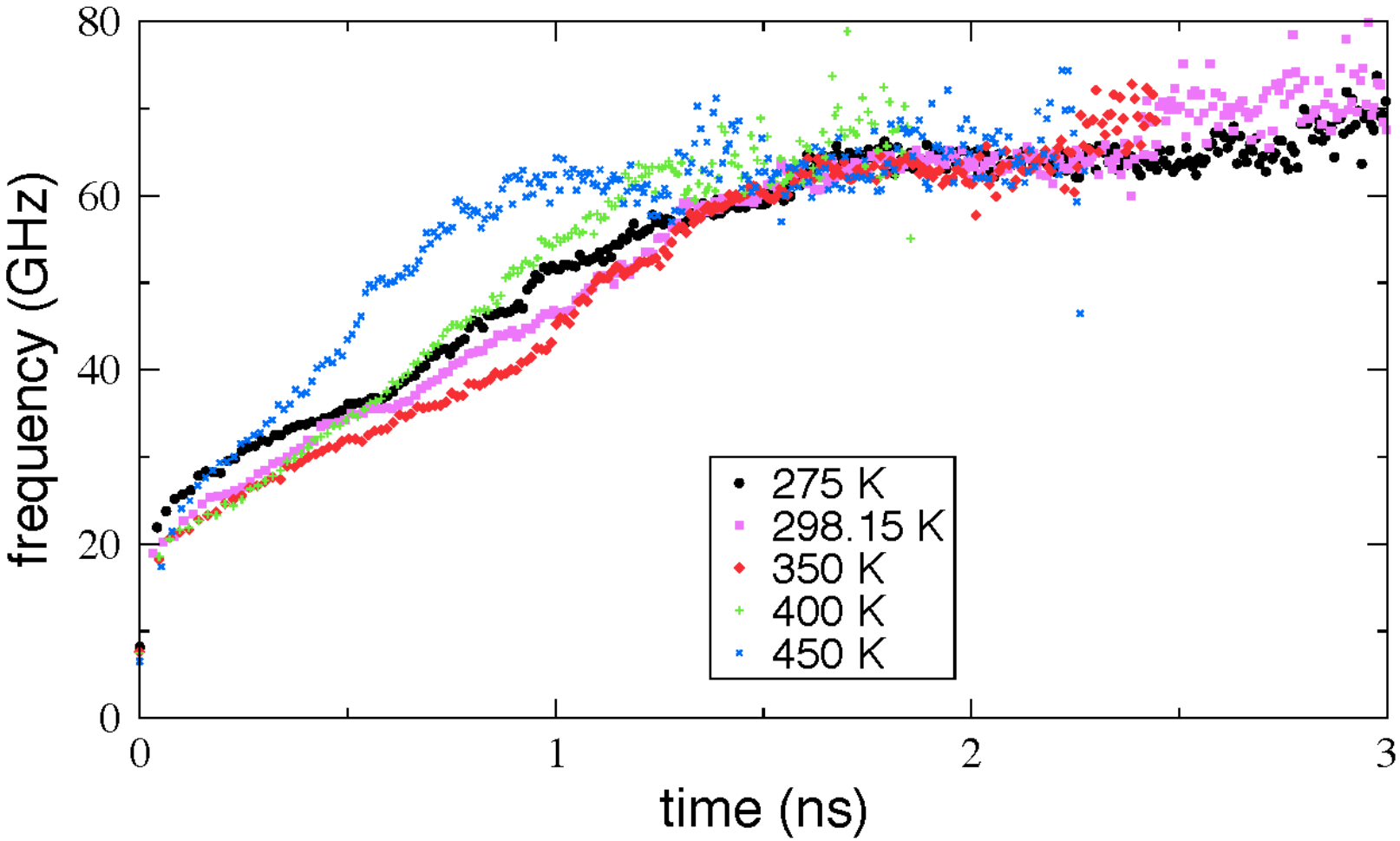


Figure 4.36: Frequency of the damped oscillations as function of the time for temperatures from 275 to 450 K. The systems have chiral conformations (7,0) / (9,9) and axial length of 12.21 nm.

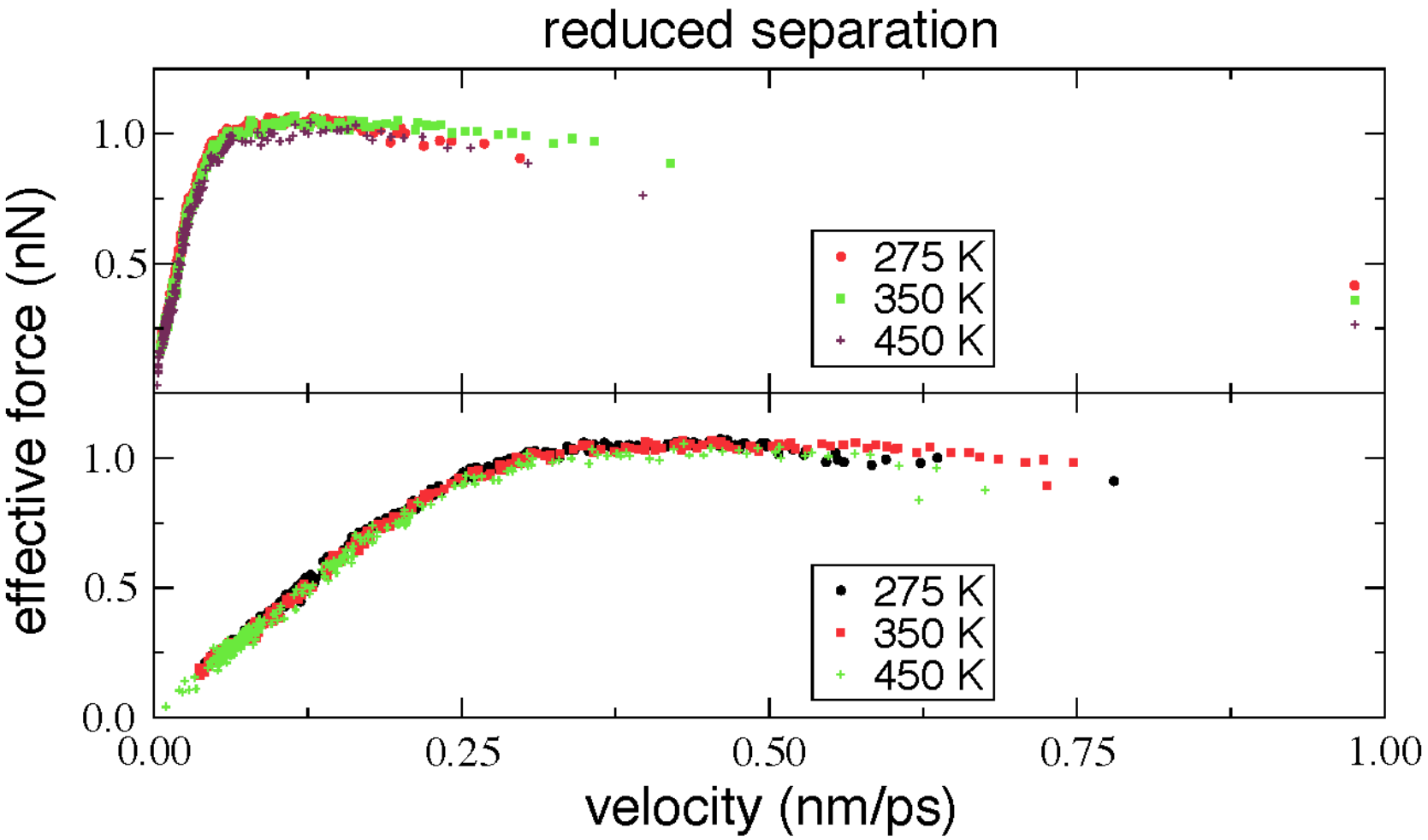


Figure 4.37: Effective forces as function of the initial reduced separation (top), and the initial velocity (bottom) for temperatures from 275 to 450 K, chiral conformations (7,0) / (9,9), and axial length of 12.21 nm.

### 4.4.6 The incommensurate system (7,0)/(10,10)

This incommensurate system has a bigger intershell distance, which is 0.06 nm larger than the one measured experimentally for graphite. This system was simulated as a hypothetical case to study the behavior of higher intershell distance. Systems with four axial lengths: 12.21, 24.56, 36.92, and 49.27 nm were simulated. The system with axial length of 12.21 nm could not be controlled and it separated completely. For the remaining systems, the simulated damped oscillations between the centers of mass are shown in Figure 4.38. The amplitude of the oscillations decreased more slowly than the corresponding cases for the system with intershell distance the same as graphite and none of them ceased their oscillation in the period of time simulated. As shown in Figure 4.39, the frequencies of oscillation are lower compared to the corresponding reference cases and they continue to increase for the period of time simulated. As in the reference case, the frequencies decrease with the axial length of the system. The most interesting characteristic of these systems is their absolute effective forces as shown in Figure 4.40. The red lines represent the optimized curves for the reference incommensurate case with intershell separation of 0.34 nm. The whole profile was not obtained because these systems never ceased their oscillations, most of the points show a linear behavior with very low dispersion and so the model with constant absolute effective forces should describe the damped behavior of these systems very well.

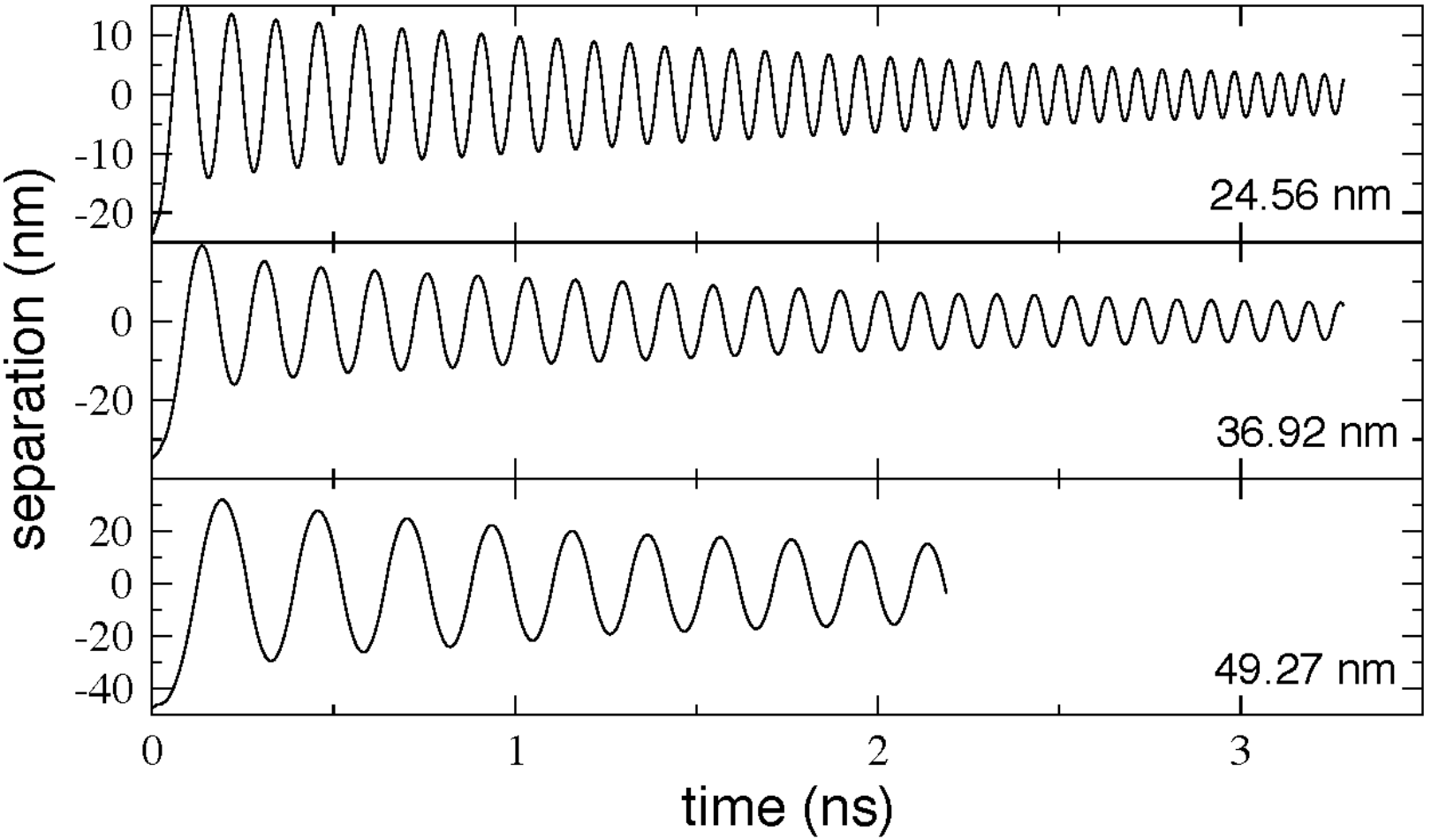


Figure 4.38: Separation of the centers of mass as function of the time for systems with chiral conformations (7,0) / (10,10), and axial lengths from 24.56 to 49.27 nm.

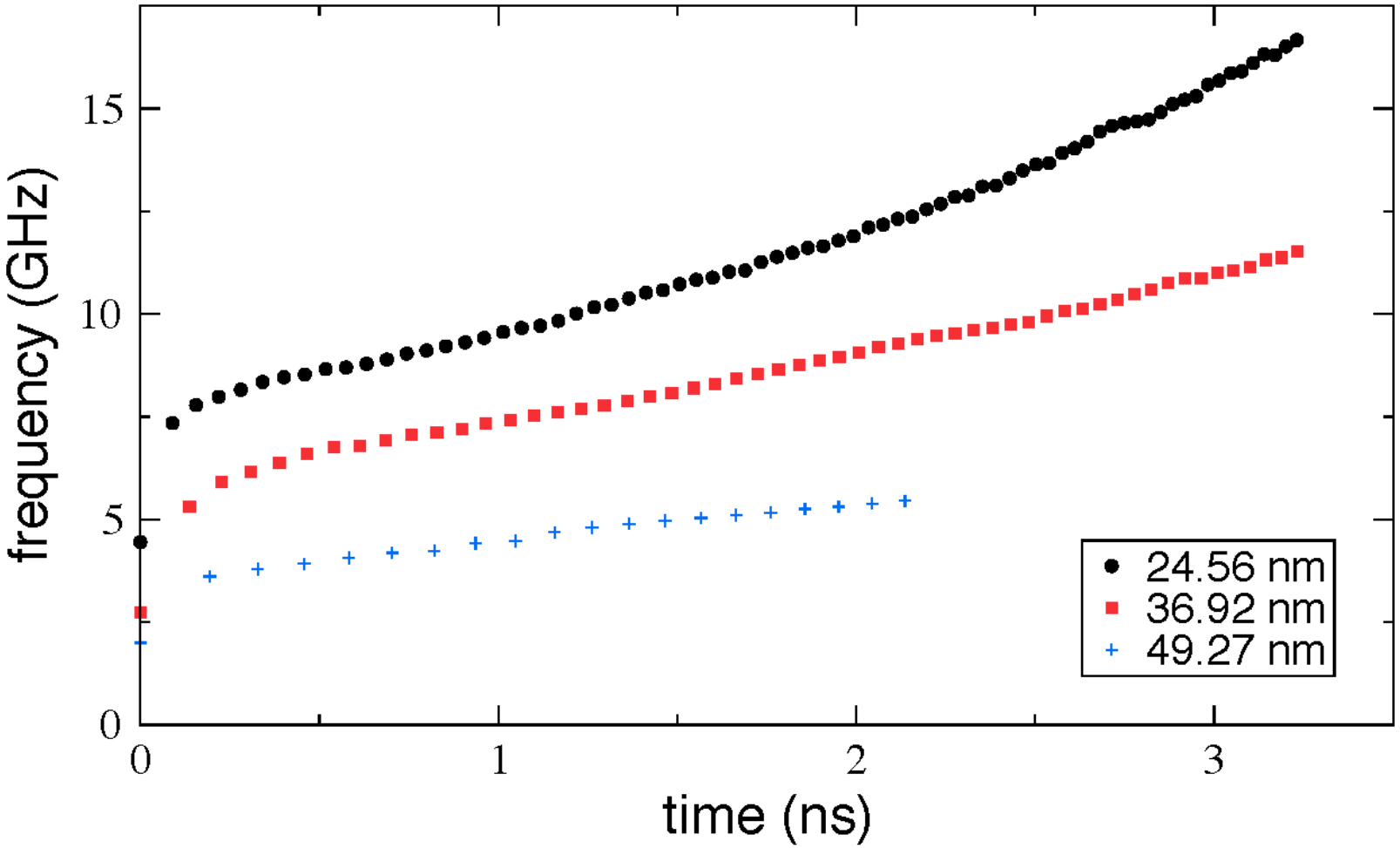


Figure 4.39: Frequency of the damped oscillations as function of the time for systems with chiral conformations (7,0) / (10,10), and axial lengths from 24.56 to 49.27 nm.

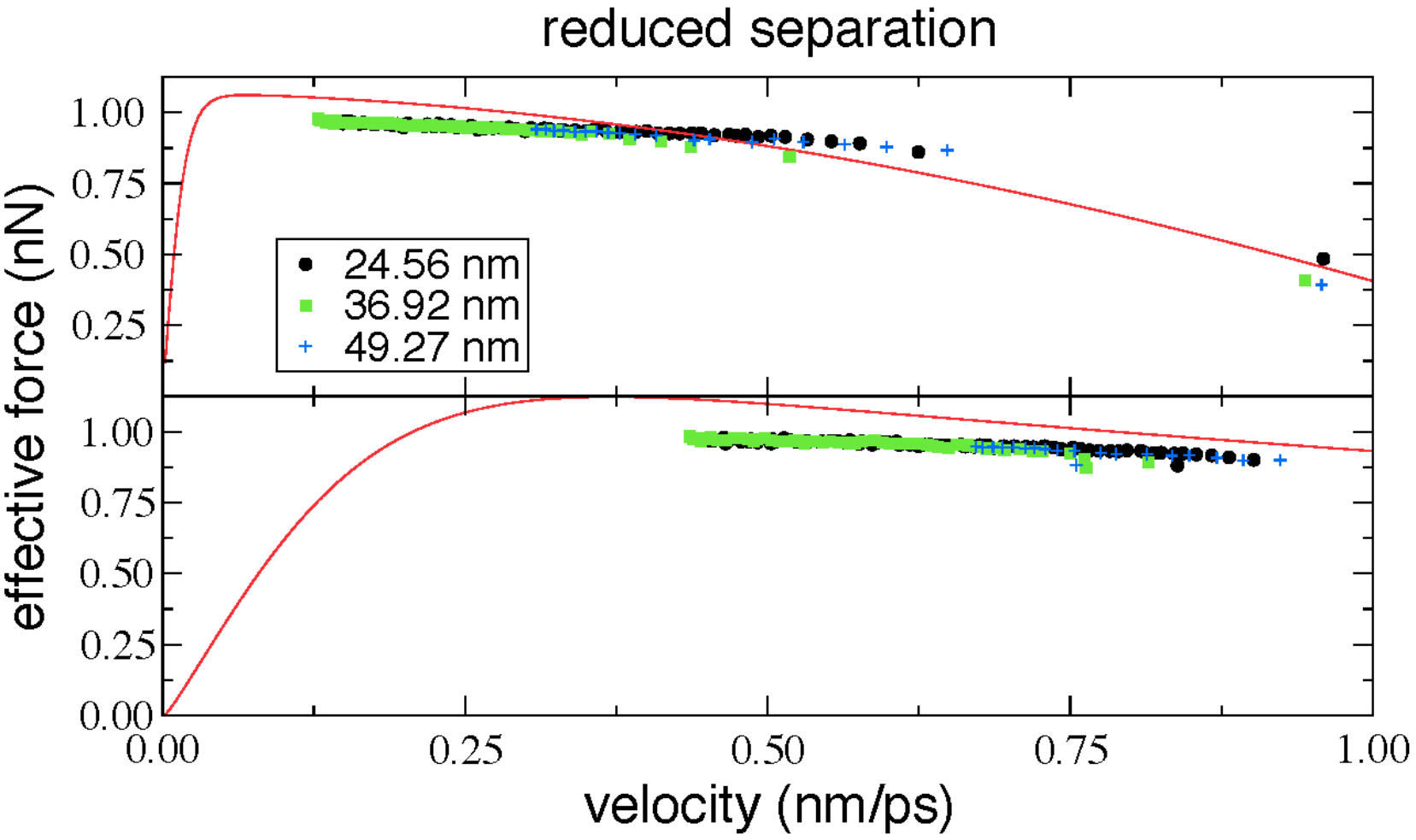


Figure 4.40: Effective forces as a function of the initial reduced separation (top) for regions I and III with chiral conformations (7,0) / (10,10), and the initial velocity (bottom) for regions II and IV. Red lines represent the optimized curves for the corresponding incommensurate systems with chiral conformations (7,0) / (9,9).

### 4.4.7 The commensurate system (5,5) / (10,10)

A commensurate system was studied using four axial lengths: 12.21, 24.56, 36.92, and 49.27 nm at 298.15 K. This system also has an intershell separation of 0.34 nm as in graphite. Results of the simulated damped oscillation are shown in Figure 4.41. The two larger systems were simulated for short times due to the long computer time required for these systems. A difference with the incommensurate case is that these systems showed very low amplitudes at the beginning of the motion and they equilibrated faster than the corresponding incommensurate cases. For the system with axial length of 12.21 nm, takes ~1.5 ns to equilibrate while for the corresponding incommensurate system takes ~2.5 ns. The frequencies of oscillation obtained are plotted in Figure 4.42. These systems show a similar behavior to the corresponding incommensurate systems. The normal frequencies when the nanotube ceased the damped oscillations are lower than the incommensurate case- i.e. for the commensurate case the frequency is ~60 GHz, while for the incommensurate it is ~75 GHz for the system with axial length of 12.21 nm. The absolute effective forces are plotted in Figure 4.43. In this figure the red line is the optimized curve for the incommensurate case and is plotted for comparison. Commensurate systems show higher maximums (~1.31 nN) and again the smallest system shows behavior different from the remaining simulated systems.

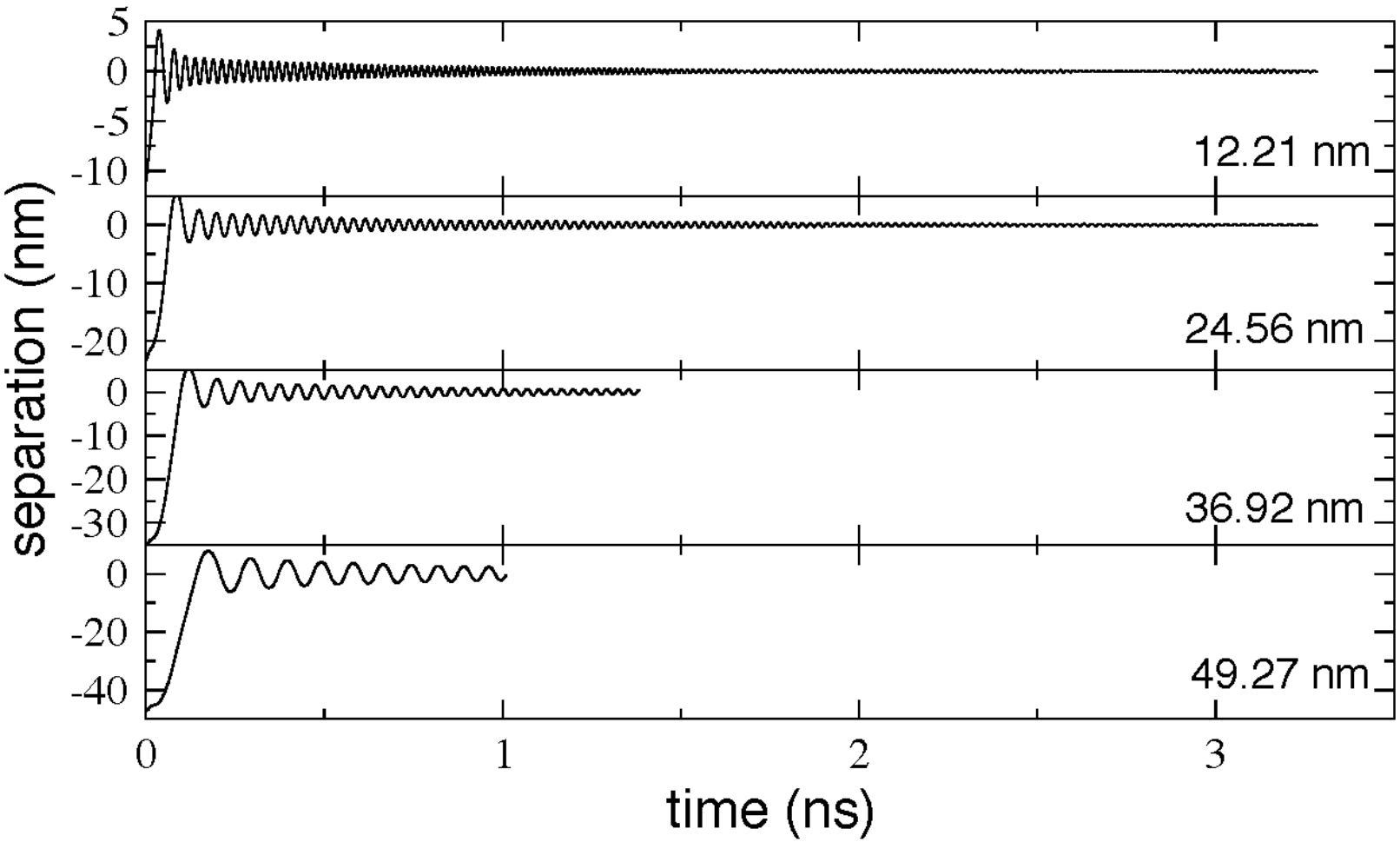


Firgure 4.41: Separation of the centers of mass as function of the time for systems with chiral conformations (5,5) / (10,10), and axial lengths from 12.21 to 49.27 nm.

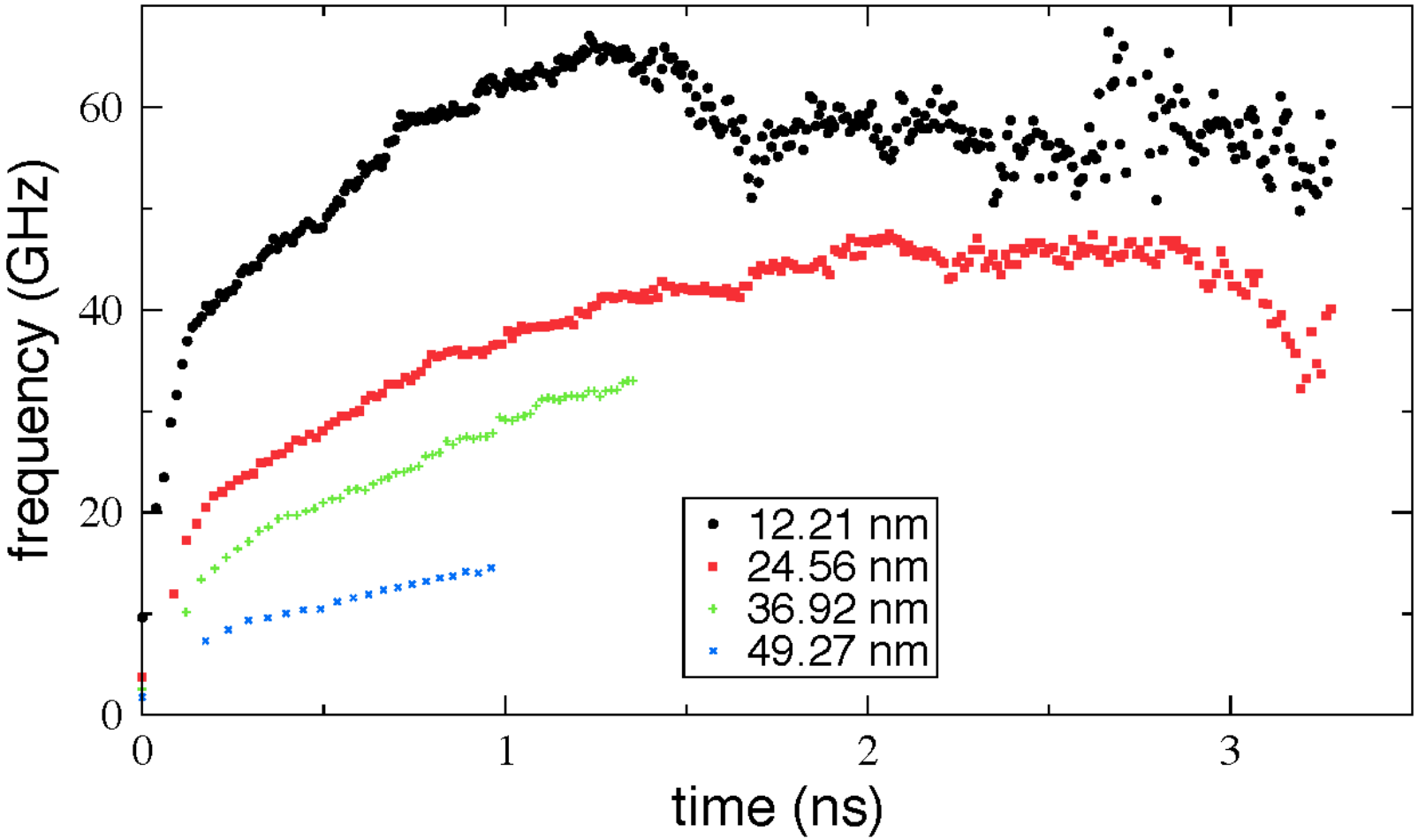


Figure 4.42: Frequency of the damped oscillations as a function of the time for systems with chiral conformations (5,5) / (10,10), and axial lengths from 12.21 to 49.27 nm.

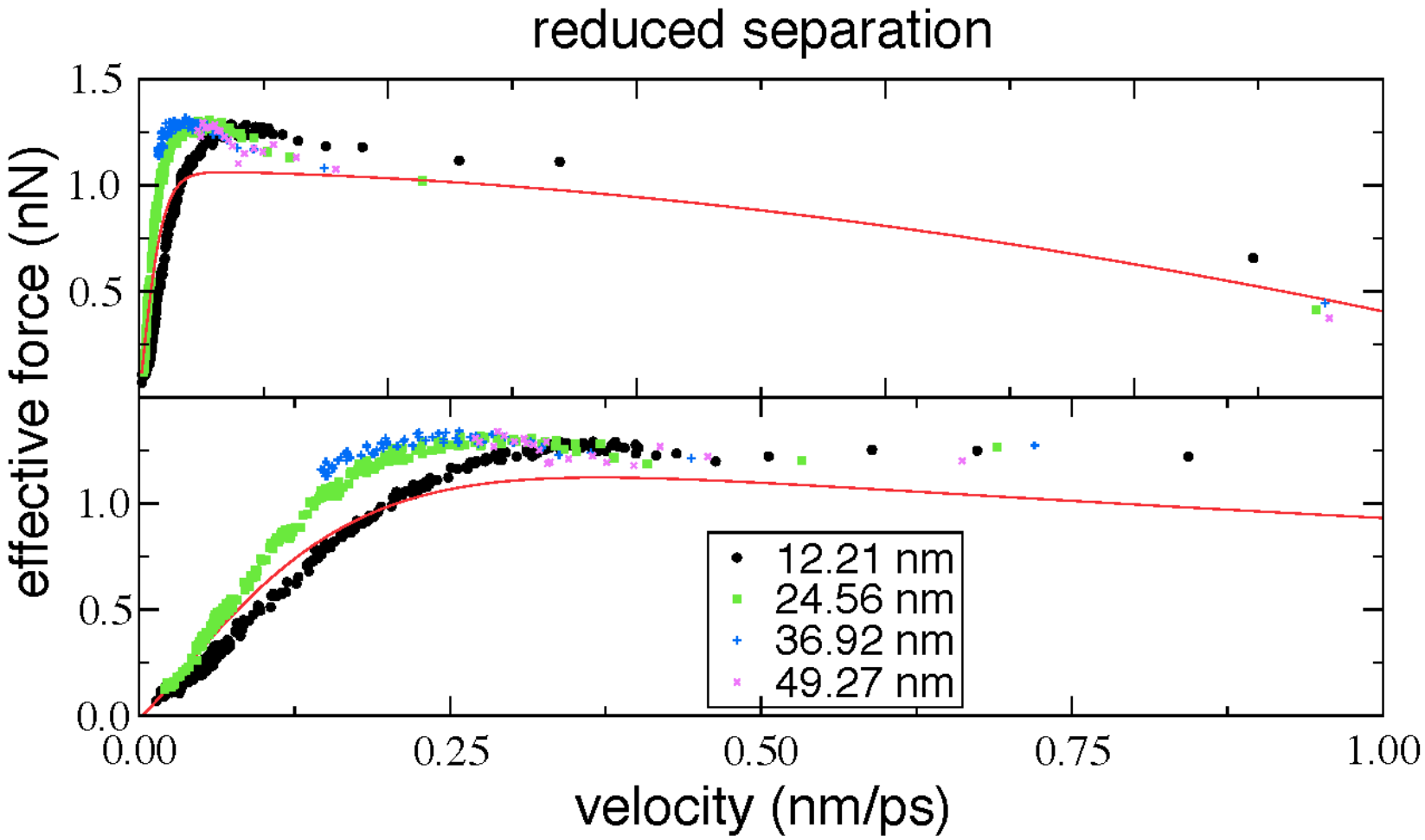


Figure 4.43: Effective forces as function of the initial reduced separation (top), and initial velocity (bottom) for systems with chiral conformations (5,5) / (10,10), and axial lengths from 12.21 to 49.27 nm. The red lines represent the optimized curves for the corresponding incommensurate systems with chiral conformations (7,0) / (9,9).

# Conclusions

Double-wall carbon nanotubes are nanomechanical systems that have potential applications as nanodevices to control nanofluids and as nanobearings and nanomotors. This study focused on the dynamics of the forces that are important in these systems. The damped oscillatory behavior of the motion between the centers of mass of double-wall carbon nanotubes was studied. Systems with three different chiral conformations were studied: (7,0)/(9,9), (7,0)/(10,10), and (5,5)/(10,10). The first two systems correspond to cases where the nanotubes formed an incommensurate system, while the last system is a commensurate system.

The incommensurate system (7,0)/(9,9) was studied for axial lengths between 12.21 and 98.24 nm. A time of ~2.5 ns was needed to cease the oscillation in the smaller system. The frequencies of oscillation obtained from these simulations have GHz magnitudes. The initial frequency of oscillation is inversely proportional to the axial length of the system in agreement with theoretical predictions. Two mechanical models were developed to understand and reproduce these damped oscillations. The first model only takes into account constant van der Waals interactions and a constant force related to the definition of friction force. This model is only valid for approximately half of the simulated time, when these forces are constant. The second mechanical model takes into account the

deformation forces that are important at long separations. The effective forces used by this model depend on the maximum and minimum separations and the velocities when the nanotube cross the zero separations. This model is valid for the whole oscillatory process and it reproduced well the simulated damped behavior. The profile of these effective forces showed a maximum at ~5% of separation. Using this maximum force as the dynamic force strength, the dynamic strength was calculated and found that to be inversely proportional to the length of the system. An absolute difference of 0.04 MPa with an estimated experimental result for this property was found. Predictions were produced for the time required to decrease the amplitude of the oscillations to less than 4 nm and for the profiles of the frequencies of oscillation.

The incommensurate system (7,0)/(9,9) was also studied with unequal axial lengths between the inner and outer nanotubes. The axial length of the inner nanotube was kept constant, while the length of the outer nanotube was varied from –30 % to +40 % the inner axial length. These systems equilibrated faster, but after equilibration the behavior is somewhat erratic and requires further investigation. A maximum absolute effective force is reached only for the nanotubes with the same axial length, but the system where the outer nanotube is 10% larger equilibrate much more rapidly (~0.5 ns).

The effect of temperature was also studied in the system with axial length of 12.21 nm. Temperatures in the range from 275 to 450 K were studied. The change of temperature does not have any effect on the profile of the absolute effective forces. Increasing the temperature has an effect on the time required to the system reach an equilibration stage, where this time decrease with the temperature, but a well-defined profile was not obtained. In terms of the frequencies of oscillation, only for the highest temperature studied showed higher frequencies at the beginning of the process.

For the incommensurate system with chiral conformation (7,0)/(10,10), four systems were studied with axial lengths from 12.21 to 49.27 nm, at 298.15 K. For the smallest system, the initial separation step to prepare the system for the damped oscillations could not be controlled. Compared to the corresponding systems with chiral conformation (7,0)/(9,9), these systems showed damped oscillations with higher amplitudes and did not reach an equilibrated configuration during the period of time simulated. For these incommensurate systems the frequency of oscillation also decreased with the axial length of the system, and the absolute effective forces showed a partial profile for which a mechanical model with constant effective forces could reproduce its behavior.

The commensurate system (5,5)/(10,10) was studied with four systems having axial lengths from 12.21 to 49.27 nm at 298.15 K. These systems showed the

shortest equilibration periods. The system with axial length of 12.21 nm needed ~1 ns less to equilibrate compared to the corresponding incommensurate system. The usually observed decrease in the frequency with the axial length of the system is also present for these systems. In terms of the absolute axial force these systems showed higher maximums compared to the incommensurate systems and again the shortest system showed a different behavior than the larger systems.

# Bibliography


Baughman R. H., Zakhidov A. A., and de Heer W. A., Carbon nanotubes – the route toward applications, *Science*, **297**, 787 (2002).

Brenner D. W., Empirical potential for hydrocarbons for use in simulating the chemical vapor deposition of diamond films, *Phys. Rev. B*, **42**, 9458 (1990).

Buldum A., and Lu J. P., Atomic scale sliding and rolling of carbon nanotubes, *Phys. Rev. Lett.*, **83**, 5050 (1999).

Buldum A. and Lu J. P., Contact resistance between carbon nanotubes, *Phys. Rev. B*, **63**, 161403 (2001).

Collins F. G., Arnold M. S., and Avouris Ph., Engineering carbon nanotubes and nanotube circuits using electrical breakdown, *Science*, **292**, 706 (2001).

Cumings J., and Zetl A., Low-friction nanoscale linear bearing realized from multiwall carbon nanotubes, *Science*, **289**, 602 (2000).

Damnjanovic M., Milosevic I., Vukovic T., and Sredanovic R., Fully symmetry, optical activity, and potentials of single-wall and multiwall nanotubes, *Phys. Rev. B.*, **60**, 2728 (1999).

Damnjanovic M., Vukovic T., and Milosevic I., Super-slippery carbon nanotubes, *Eur. Phys. J. B*, **25**, 131 (2002).

Dong S. R., Tu J. P., and Zhang X. B., An investigation of the sliding wear behavior of Cu-matrix composite reinforced by carbon nanotubes, *Mat. Sci. Eng. A*, **313**, 83 (2001).

Donnet C., Martin J. M., Le Mogne Th., and Belin M., Super-low friction of MoS2 coatings in various environments, *Tribol. Lett.*, **29**, 123 (1996).

Dresselhaus M. S., Dresselhaus G., and Avouris P. H., *Carbon Nanotubes: Synthesis, Structure, Properties, and Applications*, (Springer-Verlag, Berlin, 2001).

Drexler K. E., Building molecular machine systems, *Trends. Biotechnol.*, **17**, 5 (1999).

Drexler K. E., *Molecular machinery, manufacturing, and computation*, (Wiley-Interscience, New York, 1992).

Ebbesen T, W., *Carbon Nanotubes: Preparation and properties*, (CRC Press, Boca Raton, 1997).

Fischer J. E., Dai H., Thess A., Lee R., Hanjani N. M., Dehaas D. L., and Smalley R. E., *Phys. Rev. B*, **55**, R4921 (1997).

Forro L., Beyond Gedanken experiments, *Science*, **289**, 560 (2000).

Frankland S. J. V., Caglar A., Brenner D. W., and Griebel M., Molecular simulation of the influence of chemical cross-links on the shear strength of carbon nanotube – polymer interfaces, *J. Phys. Chem. B*, **106**, 3046 (2002).

Gao G., Cagin T., and Goddard W. A., Energetics, structure, mechanical and vibrational properties of single-walled carbon nanotubes, *Nanotechnology*, **9**, 184 (1998).

Gao G., Cagin T., and Goddard W. A., Positions of K atoms in doped single-walled carbon nanotube crystals, *Phys. Rev. Lett.*, **80**, 5556 (1998).

Guo Y., Karasawa N., and Goddard W. A., Prediction of fullerene packing in $C_{60}$ and $C_{70}$ crystals, *Nature*, **351**, 464 (1991)

Hathorn, B. C., Sumpter B. G., Noid D. W., and Barnes M. D., Molecular dynamics simulations of polymer nanoparticles collision: Internal reorganization and translation-vibration coupling, *Macromolecules*, **35**, 1102 (2002).

Humphreys D. D., Friesner R. A., and Berne B. J., A multiple-time-step molecular dynamics algorithm for macromolecules, *J. Phys. Chem.*, **98**, 6885 (1994).

Iijima S., Helical microtubules of graphitic carbon, *Nature*, **354**, 56 (1991).

Kahn D., and Lu J. P., Vibrational modes of carbon nanotubes and nanoropes, *Phys. Rev. B.*, **60**, 6535 (1999).

Kociak M., Suenega K., Hirarhara K., Saito Y., Nakahira T., and Iijima S., Linking chiral indices and transport properties of double-wall carbon nanotubes, *Phys. Rev. Lett.*, **89**, 155501 (2002).

Kolmogorov A. N., and Crespi V. H., Smoothest Bearings: Interlayer sliding in multiwalled carbon nanotubes, *Phys. Rev. Lett.*, **85**, 4727 (2000).

Kuzumaki T., Hayashi T., Miyazawa K., Ichinose H., Ito K., and Ishida Y., Discussion of the mechanical behavior of carbon nanotube / C60 composite based on observation of interfacial structure, *Mat. Trans. JIM*, **39**, 578 (1998).

Li Y., Kim W., Zhang, Y., Rolandi M., Wang D., and Dai H., Growth of single-walled carbon nanotubes from discrete catalytic nanoparticles of various sizes, *J. Phys. Chem. B*, **105**, 11424 (2001).

Liao K., and Li S., Interfacial characteristics of a carbon nanotube-polystyrene composite system, *Appl. Phys. Lett.*, **79**, 4225 (2001).

Mao Z., Garg A., and Sinnott S. B., Molecular dynamics simulations of the filling and decorating of carbon nanotubes, *Nanotechnology*, **10**, 273 (1999).

McCurdy C. W., Stechel E., Cummings P., Hendrickson B., and Keyes D., Theory and modeling in nanoscience, Report of workshop, Department of Energy, 2002.

Merkle R.C., A proof about molecular bearings, *Nanotechnology*, **4**, 86 (1993).

Muser M. H., and Robbins M. O., Conditions for static friction between flat crystalline surfaces, *Phys. Rev. B*, **61**, 2335 (2001).

Ni B., and Sinnott S. B., Tribological properties of carbon nanotubes bundles predicted from atomistic simulations, *Surf. Sci.*, **487**, 87 (2001).

Nose S., A unified formulation of the constant temperature molecular dynamics methods, *J. Chem. Phys.*, **81**, 511 (1984).

Odom T. W., Huang J-l., Kim P., and Lieber C. M., Atomic structure and electronic properties of single-walled carbon nanotubes, *Nature*, **391**, 62 (1998).

Pan C., Sampson M. P., Chai Y., Hauge R. H., and Margrave J. L., Heats of sublimation from a polycrystalline mixture of $C_{60}$ and $C_{70}$, *J. Phys. Chem.*, **95**, 2944 (1991).

Procacci P., and Berne B. J., Computer simulations of solid $C_{60}$ using multiple time-step algorithms, *J. Chem. Phys.*, **101**, 2421 (1994).

Siegal M. P., Overmyer D. L., and Provencio P. P., Precise control of multiwall carbon nanotube diameters using thermal chemical vapor deposition, *Appl. Phys. Lett.*, **80**, 2171 (2002).

Sohlberg K., Tuzun R. E., Sumpter B. G., and Noid D. W., Application of rigid-body dynamics and semiclassical mechanics to molecular bearings, *Nanotechnology*, **8**, 103 (1997).

Suh J. S., and Lee J. S., Highly ordered two-dimensional carbon nanotube arrays, *Appl. Phys. Lett.*, **75**, 2047 (1999).

Tans S. J., Verschueren A. R. M., and Dekker C., Room-temperature transistor based on a single carbon nanotube, *Nature*, **393**, 49 (1998).

Tuckerman M. E., Berne B. J., and Martyna G. J. Molecular dynamics algorithm for multiple time scales: Systems with long range forces, *J. Chem. Phys.*, **94**, 6811 (1991).

Tuckerman M., Berne B. J., and Martyna G. J., Reversible multiple time scale molecular dynamics, *J. Chem. Phys.*, **97**, 1990 (1992).

Tuzun R. E., Noid D. W., and Sumpter B. G., Dynamics of a laser driven molecular motor, *Nanotechnology*, **6**, 52 (1995).

Tuzun R. E., Noid D. W., and Sumpter B. G., The dynamics of molecular bearings, *Nanotechnology*, **6**, 64 (1995).

Tuzun R. E., Noid D. W., Sumpter B. G., and Merkle R. C., Dynamics of fluid flow inside carbon nanotubes, *Nanotechnology*, **7**, 241 (1996).

Wenning L., and Muser M. H., Friction laws for elastic nanoscale contacts, *Europhys. Lett.*, **54**, 693 (2001).

White C. T., Robertson D. H., and Mintmire J. W., Helical and rotational symmetries of nanoscale graphitic tubules, *Phys. Rev. B*, **47**, 5485 (1993).

Wildoer J. W., Venema L. C., Rinzler A. G., Smalley R. E., and Dekker C., Electronic structure of atomically resolved carbon nanotubes, *Nature*, **391**, 59 (1998).

Xu X., Thwe M. M., Shearwood C., and Liao K., Mechanical properties and interfacial characteristics of carbon-nanotube-reinforced epoxy thin films, *Appl. Phys. Lett.*, **81**, 2833 (2002).

Yu M-F., Yokobson B. I., and Ruoff R. S., Controlled sliding and pullout of nested shells in individual multiwalled carbon nanotubes, *J. Phys. Chem. B*, **104**, 8764 (2000).

Yu M-F., Lourie O., Dyer M. J., Moloni K., Kelly T. F., and Ruoff R. S., Strength and breaking mechanism of multiwalled carbon nanotubes under tensile load, *Science*, **287**, 637 (2000).

Zheng Q., and Jiang Q., Multiwalled carbon nanotubes as Gigahertz oscillators, *Phys. Rev. Lett.*, **88**, 045503 (2002).

Zheng Q., Liu J. Z., and Jiang Q., Excess van der Waals interaction energy of a multiwalled carbon nanotube with an extruded core and the induced core oscillation, *Phys. Rev. B*, **65**, 245409 (2002).

# Vita

Jose Luis Rivera Rojas was born in México, Distrito Federal on May 2, 1970. He went to high school to Escuela Nacional Preparatoria “Pedro de Alba” in México, D. F. and graduated in 1988. He went to Universidad Autonoma Metropolitana – Iztapalapa in México, D. F. and received a B. Sc. in Chemical Engineering in 1994, and a M. Sc. in Physical Chemistry in 1999.